4-2016

Mechanistic characterization of acetic acid resistance enzymes of Acetobacer aceti

Jesse R. Murphy
Purdue University

Graduate School Form
30 Updated 12/26/2015

PURDUE UNIVERSITY
GRADUATE SCHOOL
Thesis/Dissertation Acceptance

This is to certify that the thesis/dissertation prepared

By Jesse R. Murphy

Entitled
MECHANISTIC CHARACTERIZATION OF ACETIC ACID RESISTANCE ENZYMES OF ACETOBACTER ACETI

For the degree of Doctor of Philosophy

Is approved by the final examining committee:

T. Joseph Kappock
Chair

Frederick Gimble

Scott Briggs

Christine Hrycyna

To the best of my knowledge and as understood by the student in the Thesis/Dissertation Agreement, Publication Delay, and Certification Disclaimer (Graduate School Form 32), this thesis/dissertation adheres to the provisions of Purdue University's "Policy of Integrity in Research" and the use of copyright material.

Approved by Major Professor(s): T. Joseph Kappock

Approved by: Andrew Mesecar 4/18/2016

Head of the Departmental Graduate Program Date

MECHANISTIC CHARACTERIZATION OF THE ACETIC ACID RESISTANCE ENZYMES OF ACETOBACTER ACETI

A Dissertation

Submitted to the Faculty

of

Purdue University

by

Jesse R. Murphy

In Partial Fulfillment of the

Requirements for the Degree

of

Doctor of Philosophy

May 2016

Purdue University

West Lafayette, Indiana

For My Family

ACKNOWLEDGEMENTS

I would like to thank my research advisor Professor T. Joseph Kappock and the members of my research advisory committee: Professors Dr. Frederick Gimble, Dr. Scott Briggs, Dr. Christine Hrycyna, and Dr. Amy Davidson.

I would also like to thank everyone who directly contributed to this study: Stefano Donini purified and crystallized TpCSH6 and T. Joseph Kappock solved the structure. This work was essential for my first paper at Purdue. Thank you to everyone who contributed to Chapter 2: Hong Jiang synthesized the AcCoA analogue AcMX. Elwood Mullins originally solved the crystal structure of AarCH6 bound to AcMX. The degradation of AcMX in that crystal structure was the inspiration for my main body of work in the Kappock lab. Kelly Sullivan helped with the crystallography and T. Joseph Kappock solved the structures of AarC bound to synthetic CoA analogues. Thank you to everyone who contributed to Chapter 3: Hong Jiang measured the rate of HDX catalyzed by AaCS•OAA by NMR, Sandra Kerfoot measured the rate of HDX by ESI-MS, Charles Constantine made single Trp mutants, and Julie Francois measured inhibition constants of AcCoA analogues. Thank you to my family and friends who made this possible. I could not have done this without the love and support of my wife, Brianna. You were there every time I needed you. Thank you to my mom, Jody, for showing

me what hard work looks like. Thank you to my sister, Kid, whose success keeps me competitive. Thank you to my friends, Kelly Sullivan, Elwood Mullins, Kayleigh Nyffeler, and Brendan Powers.

TABLE OF CONTENTS

LIST OF FIGURES

Figure Page

Figure Page

LIST OF TABLES

ABSTRACT

Murphy, Jesse R. Ph.D, Purdue University, May 2016. Mechanistic Characterization of Acetic Acid Aesistance Enzymes of Acetobacter Aceti. Major Professor: T.J. Kappock.

Acetobacter aceti (*A. aceti*) is a Gram-negative, acidophilic bacterium that is used for the industrial production of acetic acid from ethanol. Oxidation of ethanol by membrane-bound oxidoreductases provides energy for *A. aceti* and the production of high concentrations of acetic acid is an effective defense mechanism. Acetic acid diffuses through cell membranes at low pH and effectively kills many bacteria, including *E. coli*, at low millimolar concentrations. The ability of *A. aceti* to thrive in molar concentrations of acetic acid is partially due to the twin subjects of this thesis, the acetic acid resistance factors AarA (citrate synthase, AaCS) and AarC (succinyl-CoA:acetate CoA-transferase).

AarC and CS exploit the distinct properties of the thioester moiety in acetyl-CoA (AcCoA) to catalyze different reversible reactions. AarC takes advantage of the relatively high leaving group potential of the CoA thiolate (anionic or RS^- form) to transfer the acetyl moiety of AcCoA to an active site glutamate. In contrast, CS uses the relatively acidic carbon adjacent to the thioester moiety to catalyze a Claisen/aldol condensation reaction that forms a new carbon-carbon bond. Class I CoA-transferases such as AarC produce acylglutamyl anhydride intermediates that undergo attack by the CoA thiolate on one of

its two carbonyl carbon atoms, forming distinct internal or external tetrahedralintermediates less than 3 Å apart. In this study, crystal structures were used to examine the role of the internal oxyanion hole residue Asn347 and the highly conserved elements of the external oxyanion hole.

First, a structure of the active mutant AarC-N347A bound to CoA revealed both solvent substitution for the deleted carboxamide and displacement of the adjacent Glu294. This indicates that Asn347 both polarizes and orients the essential glutamate Glu294.

Second, AarC was crystallized with the nonhydrolyzable AcCoA analogue dethiaacetyl-CoA (AcMX) in an attempt to trap a closed enzyme complex containing a stable analogue of the external oxyanion intermediate. One active site contained an acetylglutamyl anhydride adduct and a truncated AcMX, an unexpected result hinting at what would have been an unprecedented cleavage of the ketone moiety into an acetyl group and the CoA analogue MX. Solution studies confirmed that AcMX decomposition is accompanied by production of near-stoichiometric acetate, in a process that seems to depend on microbial contamination but not AarC.

Authentic MX was synthesized to evaluate the hypothesis that it is derived from AcMX. A crystal structure of AarC bound to MX showed complete closure of one active site per dimer but no acetylglutamyl anhydride, even for crystals grown in the presence of exogenous acetate. These findings imply that AcMX degradation results in the production of an activated acetyl donor; a working hypothesis involving ketone oxidation is offered. Moreover, the ability of MX to induce full active site closure suggests that it

subverts a system used to impede inappropriate active site closure on unacylated CoA.

The remainder of this thesis concerns the enzyme CS, an essential part of central metabolism in aerobes and many other organisms. The CS reaction comprises two successive reactions: a Claisen/aldol condensation of AcCoA and oxaloacetate (OAA) that forms citryl-CoA (CitCoA), and CitCoA hydrolysis. Protein conformational changes that close the active site assemble a catalytically competent condensation active site. The 2.2 Å resolution crystal structure of CS from the thermoacidophile *Thermoplasma acidophilum* (TpCS) fused to a C-terminal hexahistidine tag (TpCSH6) reported here is an open structure that, when compared with several liganded TpCS structures, helps to define a complete path for active site closure.

Hydrogen-deuterium exchange (HDX) reactions can be used to study the critical proton transfer required for condensation. In D_2O, both TpCS•OAA and AaCS•OAA catalyze rapid HDX in AcMX. Fluorescence "dequenching" that occurs upon addition of AcMX to OAA complexes of CS forms that possess a suitable (reporter) Trp is the result of the destruction of the polarized OAA carbonyl during condensation. TpCS•OAA converts AcMX to the binary condensation product complex TpCS•CitMX, which means that more than one event could account for the introduction of a deuterium atom that results in HDX. In contrast, AaCS•OAA appears to stabilize the ternary pseudo-Michaelis complex AaCS•OAA•AcMX, with no evidence of condensation. Mass spectrometric and isotope effect studies are used to define the kinetic mechanism of AaCS•OAA catalyzed HDX.

CHAPTER 1. BACKGROUND AND INTRODUCTION

1.1 Perspective

New bio-based strategies to implement large-scale replacement of petroleum-derived chemical matter have the potential to transform global economic systems. An approach called synthetic biology adds manmade evolutionary selection to create new processes and materials from existing enzymes. A key step in this process is to investigate structure/function relationships of diverse enzymes with the hope of altering substrate specificity and making new products.

In the cell, acyltransfer and carbon-carbon bond forming condensation reactions are commonly used to enlarge small molecules. Linking otherwise unreactive carboxylates to coenzyme A (CoA) through a thioester increases reactivity in one of two ways. First, the CoA moiety can facilitate acyltransfer reactions by acting as an effective leaving group due to the relatively low pK_a of the incipient thiolate. This type of acyl activation is required in the biosynthesis of phospholipids, neurotransmitters, and diverse acyl-CoAs. Second, the thioester linkage in acetyl-CoA (AcCoA) increases the acidity of the adjacent α-carbon. This type of activation is important because the first chemical step in condensation reactions is the difficult deprotonation of a carbon acid, which formally produces a highly reactive carbanion intermediate. The acyl-CoA thioester is a single

functional group that allows two main types of otherwise difficult chemical reactions to occur under physiological conditions. Biosynthesis of AcCoA by most bacteria requires an initial energy investment. Acetate must be activated, often by acetate kinase (AK) (Figure 1.1a) and ATP-dependent phosphorylation. Formation of AcCoA from acetyl-phosphate and CoA is then catalyzed by phosphotransacetylase (PTA). Alternatively, AcCoA can be synthesized from acetate, ATP, and CoA by one enzyme, AcCoA synthetase (ACS) (Figure 1.1b). ATP usage in this way is a worthwhile investment because of the diverse functionality of AcCoA and both acyl- transfer and condensation reactions allow for the recovery and recycling of CoA.

Citrate synthase (CS) catalyzes the condensation of AcCoA and OAA and hydrolysis of a citryl-CoA intermediate. There has been strong selective pressure to ensure extreme specificity as any AcCoA hydrolase activity would be metabolically detrimental to the cell. It is currently unknown how CS is able to very effectively differentiate and specifically hydrolyze citryl-CoA but not the substrate AcCoA.

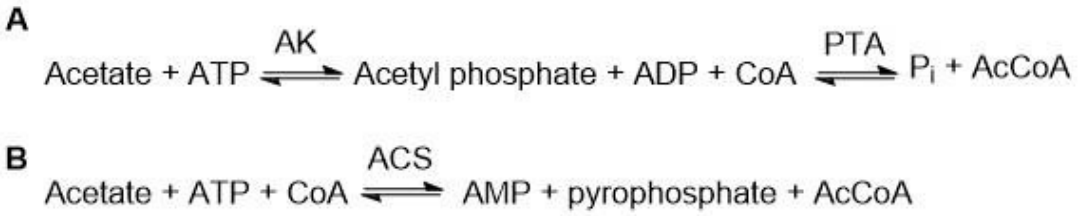

Figure 1.1 Synthesis of AcCoA. The formation of AcCoA by AK/PTA and ACS requires ATP.

***Acetobacter aceti* uses a variant citric acid cycle to remove excess cytoplasmic acetate.** Acetic acid is a cell permeable acid produced by acetic acid bacteria (AAB) that acidifies the cytoplasm and disrupts the proton gradient thereby killing competing microbes

(Francois et al., 2006). *Acetobacter aceti* (*A. aceti*) is a particularly acid tolerant AAB that is widely used in the commercial production of vinegar from ethanol (Asai, 1968). *A. aceti* has evolved extreme internal acetate tolerance that is largely attributed to increased inherent protein acid stability, expressing an acetate: proton antiporter, and expression of acetic acid resistance genes *aarABC* (Matsushita et. al., 2005; Nakano et. al., 2006; Fukaya et. al., 1990; Mullins et. al., 2008). AarA is a citrate synthase (AaCS), SixA (produced by a genetic region originally designated *aarB*) is a transcriptional regulator thought to activate flux through the citric acid cycle, and AarC is an acyl-CoA transferase (Francois et. al., 2006; Fukaya et al., 1990; Mullins et al., 2008). These enzymes work together to process the constant influx of acetate experienced by *A. aceti*. AarC catalyzes the formation of AcCoA from succinyl-CoA and free acetate or acetic acid. Acetate thereby has a direct path into the CAC in the form of AcCoA by condensation with OAA catalyzed by CS. In this variant CAC, CoA is recovered and excess acetate is lost to diffusion upon "overoxidation" to CO_2 (Mullins et al., 2008).

AarC catalyzes the formation of AcCoA from succinyl-CoA and acetate. CoA-transferases catalyze the reversible transfer of CoA from acyl-CoA thioesters to free carboxylates in order to increase acyl-CoA diversity. AarC is a succinyl-CoA: acetate CoA-transferase that allows for the direct incorporation of acetate into the CAC of *A. aceti* (Mullins and Kappock 2012). Class I CoA-transferase such as AarC catalyze CoA transfer reactions through multiple covalent adducts at the active site glutamate (Figure 1.2) (Hersh and Jencks 1967a-c; Solomon and Jencks 1969; Pickart and Jencks 1979; White and Jencks 1976).

In the forward direction, initial nucleophilic attack on the succinyl-CoA substrate by Glu294 results in the formation of the external oxyanion intermediate stabilized in a novel oxyanion hole composed of Gly388 NH and the CoA N2'' (Mullins and Kappock, 2012). The resulting CoA thiolate acts as a leaving group forming a succinylglutamyl anhydride. CoA does not exchange and is free to attack the internal succinylglutamyl anhydride carbonyl forming the internal oxyanion that is proposed to be stabilized by Asn347 (White and Jencks, 1976; Jacob et al., 1997). Upon the formation of the glutamyl- CoA thioester, succinate and free acetate are free to exchange and the reverse reaction occurs ultimately resulting in the formation of AcCoA.

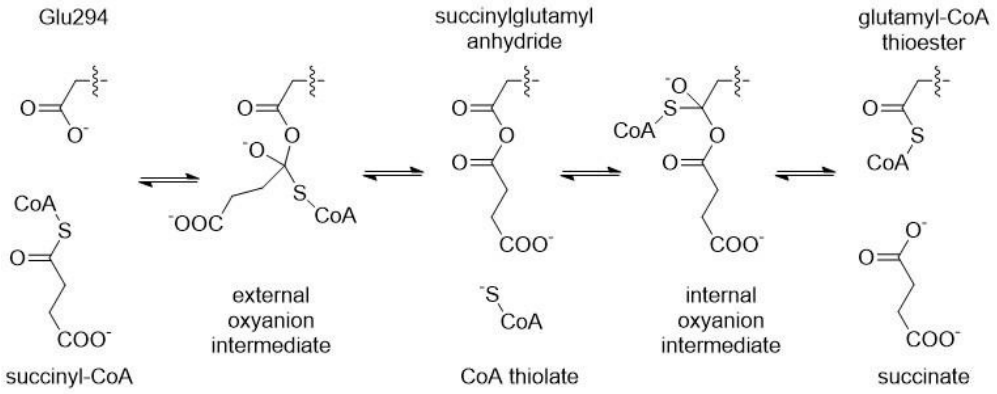

Figure 1.2. The forward half-reaction catalyzed by AarC. AarC catalyzes the freely reversible transfer of CoA between succinate and acetate. In the forward direction succinate is generated upon formation of the glutamyl-CoA thioester. Acetate exchanges with succinate and the reverse reaction occurs, ultimately forming AcCoA.

Jencks argued that for enzyme catalyzed reactions to occur it is not sufficient for enzymes to only stabilize the transition state (Jencks, 1975). In order to more easily reach the transition state, both the enzyme-substrate (ES) and enzyme-product (EP) complexes

must be destabilized by adding steric strain, desolvation of the active site, and/or decreasing entropy by holding the substrate in the proper orientation for catalysis. Enzymes must “pay” for this destabilization of the ground state by harnessing the free energy of the non-covalent binding interactions (Jencks, 1987).

Acyl-CoA transferases are an ideal model system for studying how distal, non-covalent enzyme-substrate interactions provide the driving force for catalysis. Kinetic and thermodynamic analysis of acyl-CoA transferases suggest that non-covalent interactions with the ADP moiety of acyl-CoA substrates is responsible for the observed rate enhancements in acyl-transfer (White and Jencks, 1976; Moore and Jencks, 1982). Furthermore, an intact acyl-CoA substrate is required to effectively transmute the binding energy from distal enzyme-substrate interactions into rate accelerations (Fierke and Jencks, 1982).

Due to the high concentration of intracellular acetate, AarC is under strong selective pressure forcing this CoA-transferase to have unusually high substrate specificity rapid kinetics (Mullins and Kappock, 2012). Crystal structures of AarC frozen in various stages of the reaction were later solved and were consistent with the Jencks model of catalysis (Mullins and Kappock 2012). Active site closure upon binding to a valid acyl-substrate accelerates catalysis by simultaneously constituting the external oxyanion hole, contorting the thioester into a Bürgi-Dunitz configuration, and enforcing a conformation that stabilizes acylglutamyl anhydride relative to the Michaelis complex (Bürgi et al., 1973). Previous attempts to crystallize the closed enzyme-substrate complex has required mutation of active site residues (Mullins and Kappock, 2012). To date, the closed

conformation of wild type AarC bound to substrates or analogues has not been observed. Crystal structures indicate AarC E294A bound to CoA adopts the closed conformation. However, mutation of Glu294 to alanine not only shortens the Glu side chain providing increased active site volume but also removes hydrogen bonding potential with the CoA thiol in the active site. It is therefore possible that hydrogen bonding between the CoA thiol and the Glu carboxylate prevents active site closure. The inability to structurally examine the closed form of the wild type enzyme has been a major hurdle preventing study of the unique AarC active site, specifically, the formation of adjacent oxyanion holes (Figure 1.2).

AaCS catalyzes proton exchange without condensation. As the first enzyme in the CAC, CS catalyzes one of the most important carbon-carbon bond forming reaction in all aerobes. CS catalyzes the condensation between the carbonyl of OAA and the terminal methyl group of AcCoA (Figure 1.3). The intermediate product citryl-CoA is then irreversibly hydrolyzed to citrate and CoA, in what is typically the rate- limiting step for the enzyme (Kurz et al., 2000; Kurz et al., 2009).

The similar appearance of the active site in CS forms from all domains of life has led to the assumption that they all use the same chemical mechanism, despite a very high degree of sequence divergence. CS from pig heart (PCS) or the euryarchaeon *Thermoplasma acidophilum* (TpCS) are dimeric (type I) whereas CS from *E. coli* (EcCS) or *A. aceti* (AaCS) are hexameric (type II) (Singh et al., 1970; Kurz et al., 2000; Francois et al., 2006). AaCS was crystallized in the closed form bound to OAA and carboxymethyldethia-CoA (CMX). This confirmed that the hexameric forms consist of three protomers, each

resembling the type I dimer, and the two types have near superimposable active sites suggesting that the number of protein subunits does not affect the mechanism (Remington et al., 1982; Wiegard et al., 1984; Usher et al., 1994).

The CS condensation reaction can be studied without interference from the hydrolysis reaction using the AcCoA analogue AcMX, in which the thioester is replaced with a ketone (Kurz et al., 2009). Condensation can be monitored directly using fluorescence spectroscopy in both CS types that contain a reporter tryptophan (Kurz et al., 2000; Francois et al., 2006). Substantial quenching of intrinsic tryptophan fluorescence upon OAA binding is caused by proximity of the polarized OAA carbonyl to a semi-conserved Trp residue (Kurz et al., 2005). During condensation, the OAA carbonyl is attacked by the AcCoA enolate causing conversion of the sp^2 orbital to sp^3 upon formation of citryl-CoA (Figure 1.3), effectively “dequenching” Trp fluorescence (Figure 1.3) (Kurz et al., 2009).

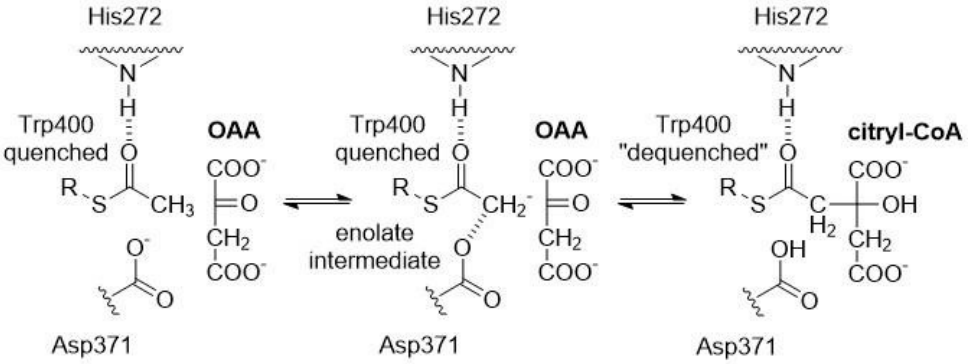

Figure 1.3. Condensation half-reaction catalyzed by AaCS. AcCoA (R is the remainder of CoA) and OAA are shown bound in the AaCS active site. Asp371 is the base that deprotonates the terminal methyl group of AcCoA forming the enolate intermediate. His272 plays an orientational role and interacts with the thioester of AcCoA and the enolate intermediate. The carbanion attacks the polarized carbonyl of OAA forming citryl-CoA. CS then hydrolyzes citryl-CoA to form citrate and CoA. It is important to note that the AcCoA analogue AcMX where the thioester sulfur is replaced with a ketone methylene would prevent hydrolysis and thus isolate the condensation half-reaction.

The first chemical step in the condensation reaction is deprotonation of the terminal methyl group of AcCoA, resulting in transient formation of an enolate intermediate with strong carbanion character. Transient carbanion formation can be monitored by hydrogen deuterium exchange (HDX) of substrate protons for solvent deuterons (Rose, 1958). CS●OAA catalyzed HDX of the terminal methyl group of AcCoA is not observed during turnover in D_2O (Kurz et al., 2000). The non-hydrolyzable but HDX susceptible AcCoA ketone analogue AcMX isolates the condensation reaction from the subsequent hydrolysis but does not completely isolate the proton transfer reaction (Kurz et al., 2009). Fluorescence dequenching is observed upon TpCS●OAA binding to AcMX, consistent with crystallographic detection of the citryl-CoA analogue citryl-MX. Hydrolysis of citryl-MX is not chemically possible due to the pKa of what would be the incipient

carbanion and dissociation of citryl-MX was not observed. Instead, reverse condensation occurs resulting in reformation of OAA and partially exchanged AcMX. It is difficult to determine if AcMX HDX occurs before or after condensation between AcMX and OAA. This is an important distinction because HDX prior to condensation would indicate the reversible formation of a carbanion whereas HDX after condensation would indicate that proton transfer and condensation are concerted. PCS may address this issue because the equilibrium favors PCS●OAA●AcCoA over PCS●CitCoA but PCS lacks an OAA sensitive Trp residue (Kurz et al., 2009). The work highlighted here shows that AaCS catalyzes AcMX HDX without formation of citryl-MX and therefore is the CS form best suited to study the critical proton transfer reaction.

1.2 Purpose

The following is a structure/function examination of two enzyme types, an acyl-CoA transferase (AarC) and citrate synthase (CS). AarC and AaCS are related in that they are essential for the extreme acid tolerance of of *A. aceti*. Furthermore, these enzymes must form and stabilize oxygen and carbon centered nucleophiles that are used in central metabolism to enlarge small molecules.

Chapter 2 provides the first published and deposited unliganded structure of TpCS and allows for detailed examination of conformational changes upon ligand binding. This work also provides the generation and purification of a hexahistidine tagged TpCS (TpCSH6) and the kinetic analysis to show this tag has little effect on enzyme activity. This CS form greatly simplifies the commonly used purification protocol involving the use of

dye ligand columns (Sutherland et. al., 1991). [The contents of Chapter 2 were published in Murphy et. al., 2015].

Chapter 3 examines AarC active site closure and probes the assembly of adjacent oxyanion holes. Mutagenesis of the internal oxyanion hole previously showed diminished activity (Mullins and Kappock, 2012). The data presented here suggests that Asn347 acts to not only stabilize the internal oxyanion but also plays a role in orienting Glu294 in the active site. As the external oxyanion hole is comprised of the Gly388 backbone nitrogen and the distal amide nitrogen of the substrate itself, the external oxyanion was probed using the unreactive substrate analogue AcMX. The evidence provided in chapter 3 suggests that microbial contamination initially oxidized AcMX and allowed the product to act as an effective AarC acylating agent. The identity of the nucleotide containing product, after acyl-transfer, is unclear but provided the framework for future experiments. The proposed product, MX, is a CoA analogue where the terminal thiol is replaced with a methyl group. Crystal structures of wild type AarC bound to MX adopted the closed conformation where AarC bound to CoA remains open. This suggests that hydrogen bonding between the active site glutamate and the CoA thiol is responsible for discrimination between acyl-CoA substrates and the weak inhibitor CoA. [The contents of Chapter 3 have been submitted for review].

Chapter 4 demonstrates that AaCS can catalyze hydrogen-deuterium exchange without condensation in the AcCoA ketone analogue AcMX. This analogue has been used to isolate the condensation reaction in another CS form, TpCS. (Kurz et al., 2009). It was also demonstrated that TpCS catalyzes HDX of the terminal methyl group of AcMX but

rate constants for the condensation and reverse-condensation reaction, derived from fluorescence “dequenching” kinetics, are much faster. Thus it is not possible to determine if HDX occurs prior to condensation or only as the enzyme performs the reverse-condensation reaction. AaCS also catalyzes HDX of the terminal methyl group of AcMX but apparently cannot perform the subsequent condensation reaction to a detectable extent. To date, AaCS●OAA + AcMX is the only known system to perform HDX without condensation and therefore hydrolysis. This provides a comparatively simplified system for the study of proton exchange in CS and shows AaCS is the ideal form to study this reaction.

1.3 References

1. Jencks, W. P. (1963). The Chemistry of Biological Energy Transfer. *Survey of progress in chemistry*, *1*, 249.

2. Francois, J. A., Starks, C. M., Sivanuntakorn, S., Jiang, H., Ransome, A. E., Nam, J. W., Constantine, C.Z., and Kappock, T. J. (2006). Structure of a NADH-insensitive hexameric citrate synthase that resists acid inactivation. *Biochemistry*, (45), 13487-13499.

3. Asai, T. (1968) Acetic acid bacteria. Classification and biochemical activities, University of Tokyo Press, Tokyo, Japan.

4. Matsushita, K., T. Inoue, O. Adachi, and H. Toyama. 2005. Acetobacter aceti possesses a proton motive force-dependent efflux system for acetic acid. J. Bacteriol. 187:4346–4352.

5. Nakano, S., M. Fukaya, and S. Horinouchi. 2006. Putative ABC transporter responsible for acetic acid resistance in Acetobacter aceti. Appl. Environ. Microbiol. 72:497–505).

6. Fukaya, M., H. Takemura, H. Okumura, Y. Kawamura, S. Horinouchi, and T. Beppu. 1990. Cloning of genes responsible for acetic acid resistance in Acetobacter aceti. J. Bacteriol. 172:2096–2104.

7. Mullins, E. A., Francois, J. A., & Kappock, T. J. (2008). A specialized citric acid cycle requiring succinyl-coenzyme A (CoA): acetate CoA-transferase (AarC) confers acetic acid resistance on the acidophile Acetobacter aceti.Journal of bacteriology, 190(14), 4933-4940.

8. Mullins, E. A., & Kappock, T. J. (2012). Crystal structures of Acetobacter aceti succinyl-coenzyme A (CoA): acetate CoA-transferase reveal specificity determinants and illustrate the mechanism used by class I CoA-transferases. *Biochemistry*, *51*(42), 8422-8434.

9. Hersh, L. B., & Jencks, W. P. (1967). Coenzyme A Transferase KINETICS AND EXCHANGE REACTIONS. *Journal of Biological Chemistry*, *242*(15), 3468-3480.

10. Hersh, L. B., & Jencks, W. P. (1967). Coenzyme A Transferase ISOLATION AND PROPERTIES OF AN ENZYME-COENZYME A INTERMEDIATE.*Journal of Biological Chemistry*, *242*(15), 3481-3486.

11. Hersh, L. B., & Jencks, W. P. (1967). Isolation of an enzyme-coenzyme A intermediate from succinyl coenzyme A-acetoacetate coenzyme A transferase. *Journal of Biological Chemistry*, *242*(2), 339-340.

12. Solomon, F., & Jencks, W. P. (1969). Identification of an enzyme-γ-glutamyl coenzyme A intermediate from coenzyme A transferase. *Journal of Biological Chemistry*,*244*(4), 1079-1081.

13. Pickart, C. M., & Jencks, W. P. (1979). Formation of stable anhydrides from CoA transferase and hydroxamic acids. *Journal of Biological Chemistry*, *254*(18), 9120-9129.

14. White, H., & Jencks, W. P. (1976). Mechanism and specificity of succinyl-CoA: 3-ketoacid coenzyme A transferase. *Journal of Biological Chemistry*, *251*(6),1688-1699.

15. Jacob, U., Mack, M., Clausen, T., Huber, R., Buckel, W., and, Messerschmidt, A. (1997) Glutaconate CoA-transferase from Acidaminococcus fermentans: The crystal structure reveals homology with other CoA-transferases. Structure 5, 415−426.

16. Jencks, W.P. (1975). Binding energy, specificity and enzymic catalysis: The Circe effect. *Adv. Enzymol*. 43:219.

17. Burgi, H. B., Dunitz, J. D., & Shefter, E. (1973). Geometrical reaction coordinates. II. Nucleophilic addition to a carbonyl group. *Journal of the American Chemical Society*, *95*(15), 5065-5067.

18. Kurz, L. C., Drysdale, G., Riley, M., Tomar, M. A., Chen, J., Russell, R. J., & Danson, M.J. (2000). Kinetics and mechanism of the citrate synthase from the thermophilic archaeon Thermoplasma acidophilum. *Biochemistry*,*39*(9), 2283-2296.

19. Kurz, L. C., Constantine, C. Z., Jiang, H., & Kappock, T. J. (2009). The partial substrate dethiaacetyl-coenzyme A mimics all critical carbon acid reactions in the condensation half-reaction catalyzed by Thermoplasma acidophilum citrate synthase. *Biochemistry*, *48*(33), 7878-7891.

20. Singh, M., Brooks, G. C., & Srere, P. A. (1970). Subunit structure and chemical characteristics of pig heart citrate synthase. *Journal of Biological Chemistry*, *245*(18), 4636-4640.

21. Remington, S., Wiegand, G., & Huber, R. (1982). Crystallographic refinement and atomic models of two different forms of citrate synthase at 2· 7 and 1· 7 Å resolution. *Journal of molecular biology*, *158*(1), 111-152.

22. Wiegand, G., Remington, S., Deisenhofer, J., & Huber, R. (1984). Crystal structure analysis and molecular model of a complex of citrate synthase with oxaloacetate and S-acetonyl-coenzyme A. *Journal of molecular biology*, *174*(1), 205-219.

23. Usher, K. C., Remington, S. J., Martin, D. P., & Drueckhammer, D. G. (1994). A very short hydrogen bond provides only moderate stabilization of an enzyme-inhibitor complex of citrate synthase. *Biochemistry*, *33*(25), 7753-7759.

24. Kurz, L. C., Fite, B., Jean, J., Park, J., Erpelding, T., & Callis, P. (2005). Photophysics of tryptophan fluorescence: link with the catalytic strategy of the citrate synthase from Thermoplasma acidophilum. *Biochemistry*, *44*(5), 1394-1413.

25. Rose, I. A., & Rieder, S. V. (1958). STUDIES ON THE MECHANISM OF THE ALDOLASE REACTION ISOTOPE EXCHANGE REACTIONS OF MUSCLE AND YEAST ALDOLASE. *Journal of Biological Chemistry*, *231*(1), 315-329.

CHAPTER 2. AN ACTIVE SITE-TAIL INTERACTION IN THE STRUCTURE OF HEXAHISTIDINE-TAGGED THERMOPLASMA ACIDOPHILUM CITRATE SYNTHASE

2.1 Introduction

Citrate synthase (CS) performs two sequential reactions: a reversible condensation reaction converts acetyl coenzyme A (AcCoA) and oxaloacetate (OAA) into citryl-CoA (CitCoA), and an irreversible thioester hydrolysis then forms citrate and CoA. This pivotal metabolic reaction is performed by members of at least three enzyme superfamilies (Eggerer, 1965; Gottschalk & Barker, 1966; Kobylarz et al., 2014). The CS dimer is a classic case of induced-fit substrate binding (Srere, 1966; Bloxham et al., 1980). OAA binding induces domain closure and the formation of an AcCoA binding site between the large and small domains of each subunit (Remington et al., 1982; Wiegand & Remington, 1986; Daidone et al., 2004). Since many conserved active-site residues participate in both the condensation and hydrolysis reactions, the central CS–CitCoA complex is expected to toggle among multiple configurations (Bayer et al., 1981). Strong selective pressure ensures a high degree of substrate specificity: CS does not cleave AcCoA but efficiently hydrolyzes CitCoA (Srere, 1972). A mechanism proposed for the condensation reaction, based in part on the crystal structures of liganded complexes

Declaration of collaborative work: In this study the TpCS crystals were prepared by Stefano Donini and the structure was solved by T. Joseph Kappock. All other experiments and analysis were done by Jesse R. Murphy. This chapter has been published and used with permission: Murphy, J., R., Donini, S., Kappock, T.J., An active site-tail interaction in the structure of hexahistidine-tagged Thermoplasma acidophilum citrate synthase. Acta Crystallographica Section F: Structural Biology Communications 71.10 (2015): 1292-1299.

(Karpusas et al., 1990; Remington, 1992), remains broadly consistent with subsequent experimental findings. Computation-based models for the proton transfers involved in carbon–carbon bond formation (Donini et al., 2000; Mulholland et al., 2000; Yang & Drueckhammer, 2003; van der Kamp et al., 2008, 2010) have not reached consensus (Aleksandrov et al., 2014).

CS from the thermophilic, acidophilic euryarchaeon Thermoplasma acidophilum (TpCS; Danson et al., 1985) has several advantages for mechanistic studies, among them an endogenous fluorophore that reports directly on enzyme chemistry (Kurz et al., 2000, 2005). TpCS Trp348 fluorescence is strongly quenched by OAA binding nearby (Kurz et al., 2005). The subsequent addition of either carboxymethyl-CoA (CMCoA) or carboxymethyl-dethiaCoA (CMX), potent CS inhibitors that resemble the deprotonated AcCoA species produced during the condensation reaction, forms a 'closed' ternary complex (Bayer et al., 1981; Karpusas et al., 1990; Kurz et al., 1992) but has little effect on TpCS fluorescence (Kurz et al., 2005). Quenching is, however, alleviated by the subsequent addition of dethiaacetyl-CoA (AcMX), an AcCoA analog that contains a methylene instead of sulfur (Martin et al., 1994; Kurz et al., 1997, 2005). The fluorescence increase is owing to destruction of the Trp348 quencher, the polarized OAA carbonyl, by its conversion to an sp3 carbon in the nonhydrolyzable CitCoA analogue dethiacitryl-CoA (CitMX; Kurz et al., 2009). Reversible, stoichiometric formation of a nonhydrolyzable binary TpCS–CitMX complex was detected by equilibrium fluorescence analysis, pre-steady-state kinetics and a crystal structure (PDB entry 2r9e; C. Lehmann, L. C. Kurz & T. E. Ellenberger, unpublished

work). Since the TpCS protein conformation is almost the same in the ternary TpCS–OAA–CMCoA complex (PDB entry 2r26; C. Lehmann, L. C. Kurz & T. E. Ellenberger, unpublished work), the active site arrangement is likely to represent the configuration used for the condensation reaction, not hydrolysis. This study addresses two barriers to the further study of conformational changes in TpCS. Firstly, an unliganded structure of TpCS has been reported (Russell et al., 1994) but the coordinates have not been deposited. This hampers the analysis of protein motions accompanying the formation of the TpCS–OAA (PDB entry 2ifc; C. Lehmann, L. C. Kurz & T. E. Ellenberger, unpublished work) and TpCS–OAA–CMCoA complexes. Secondly, TpCS purification involves a dye-linked affinity column (Sutherland et al., 1991) that may displace (acyl-) CoA ligands (Weitzman & Ridley, 1983) and irreversibly binds at least one mutant protein (Constantine, 2009). Here, we report the purification, characterization and crystal structure of TpCS fused to a C-terminal hexahistidine affinity tag (TpCSH6). While the affinity tag has only minor effects on enzyme function in solution, it promotes the formation of a crystal with a His tag bound to an adjacent active site. Liganded and 'empty' partner subunits adopt essentially the same 'open' conformation.

2.2 Materials and Methods

DNA manipulations

Oligodeoxynucleotides (ODNs) were from IDT (Coralville, IA). DNA-modifying enzymes were from New England Biolabs (Beverly, MA). A Vent DNA polymerase PCR product, obtained with ODN primers 1306 and 1307 (Table 1) and plasmid pRec7-ArCS as template,

added flanking NdeI and XhoI sites to the gltA open reading frame and deleted the native stop codon. Ligation into the corresponding sites of plasmid pET24a furnished TpCSH6 expression plasmid pJK438, which adds a 15-residue peptide VDKLA AALEH HHHHH (residues 385-399) to the native C-terminus of TpCS. A QuikChange mutagenesis kit (Agilent, La Jolla, CA), pJK438, ODN 2066 50-GCTGCAaGGCGGTGCAGCTGAGG), and ODN 2067 50-ACCGCCtTGCAGCGGACCCTTG) were used to construct the TpCSH6-H222Q expression plasmid pJK511. Bidirectional Sanger sequencing of the coding region was used to confirm that both plasmids contained the expected DNA sequences.

Macromolecule production

Escherichia coli C41 (DE3) cells transformed with either pJK438 or pJK511 (cloning procedures are given in the Supporting Information) were propagated in LB medium supplemented with 50 mg l1 kanamycin. Production cultures (1 L) were grown at 310 K to an optical density at 600 nm of 0.6, at which point isopropyl -d-1-thiogalactopyranoside (IPTG; Gold Biotechnology, St Louis, Missouri, USA) was added (0.4 mM final concentration) to induce protein production. After a further 16 h, the cells were harvested by centrifugation (8000g for 15 min at 277 K), resuspended in 8 ml buffer H (20 mM Tris–HCl pH 8.0, 100 mM KCl) per gram of wet cell weight and disrupted by sonication. Streptomycin was added to a final concentration of 1% (w/v) from a 10%stock and solids were removed by centrifugation (30 000g for 10 min at 277 K). Column-chromatography steps were performed at 295 K under gravity flow. A Ni^{2+}-loaded iminodiacetic acid Sepharose column (Sigma–Aldrich, St Louis, Missouri, USA; 2.5 3.5 cm, 14 ml column

volume) was washed with buffer H (140 ml) and the cleared cell lysate was applied. The column was washed with buffer H containing 20 mM imidazole (42 ml) and was developed with buffer H containing 250 mM imidazole (100 ml). Protein-containing fractions were pooled and concentrated to >5 mg ml1 by ultrafiltration using an Amicon Ultra-15 centrifugal filter unit (EMD Millipore, Billerica, Massachusetts, USA). Solid ammonium sulfate was added to 85% saturation at 277 K over 30 min. After stirring for a further 30 min at 277 K, aliquots were taken and stored as a slurry at 277 K. For crystal production, an aliquot was dissolved in a minimal volume of TE (20 mM Tris–HCl pH 8.0, 1 mM EDTA) and applied onto a Sephadex 200 gel-filtration column (2.5 x 8 cm; Pharmacia, Uppsala, Sweden) that was developed in TE. Protein containing fractions were collected, pooled and concentrated to 5 mg ml1. Exchanged samples were kept at 277 K and used within 12 h. Proteins were quantitated by the method of Bradford using bovine serum albumin as a standard (Bradford, 1976). Gel-filtration analysis was used to determine molecular sizes as described by Mullins et al. (2013). Macromolecule- production information is summarized in Table 1. Enzyme activities were determined using a continuous assay that detects CoA release by monitoring the cleavage of 5,50-dithiobis(2-nitrobenzoic acid) (DTNB) at 412 nm ($\Delta\epsilon$ = 14.1 mM^{-1} cm^{-1}; Srere et al., 1963; Srere, 1969; Riddles et al., 1979). One unit (U) is defined as the amount of enzyme required to produce 1 mmol of product per minute.

Table 2.1

Macromolecule-production information.

Source organism	*T. acidophilum*
DNA source	Plasmid pJK438
Forward primer†	ACAGGAGTACATATGCCAGAAACTGAAGAA
Reverse primer†	TTGAGAAAACTCGAGTCACTTTCTTTCAGC
Expression vector	pET-24a
Expression host	*E. coli* C41(DE3)
Complete amino-acid sequence of the construct produced‡	PETEEISKGLEDVNIKWTRLTTIDGNKGILRYGG- YSVEDIIASGAQDEEIQYLFLYGNLPTEQELR- KYKETVQKGYKIPDFVINAIRQLPRESDAVAM- QMAAVAAMAASETKFKWNKDTDRDVAAEMIGR- MSAITVNVYRHIMNMPAELPKPSDSYAESFLN- AAFGRKATKEEIDAMNTALILYTDHEVPASTT- AGLVAVSTLSDMYSGITAALAALKGPLHGGAA- EAAIAQFDEIKDPAMVEKWFNDNIINGKKRLM- GFGHRVYKTYDPRAKIFKGIAEKLSSKKPEVH- KVYEIATKLEDFGIKAFGSKGIYPNTDYFSGI- VYMSIGFPLRNNIYTALFALSRVTGWQAHFIE- YVEEQQRLIRPRAVYVGPAERKYVPIAERKVD- KLAAALEHHHHHH
UniProt identifier	P21553

† The restriction sites in ODNs 1306 (forward, NdeI) and 1309 (reverse, XhoI) are underlined. Stop codon 385 is replaced by the vector-encoded tag sequence. ‡ The recombinant protein lacks an N-terminal Met. The 15-residue His6 tag appended to the C-terminus of the native sequence is underlined.

Enzyme kinetics and inhibition analysis

Enzyme activities at 298 K were recorded on a Cary 100 spectrophotometer (Varian) equipped with a Peltier temperature controller. Nonlinear least-squares fitting was performed using using gnuplot (version 4.4). Enzyme initial velocities were determined in a final volume of 0.7 mL that contained 50 mM 4(2-hydroxyethyl)-1-piperazinepropanesulfonic acid (EPPS), pH 8.0, 0.1 mM EDTA, 0.3 mM DTNB, either 15 M or 0.4 mM OAA, variable amounts of the other substrate, and either TpCSH6 (0.6 g) or TpCSH6-H222Q (20 g). Kinetic constants were obtained by fitting initial velocity data to the Michaelis-Menten equation. AcMX, synthesized by Hong Jiang as described (Francois et al., 2006), was used to prepare the TpCS CitMX complex (PDB entry 2r9e) and assessed as a TpCSH6 inhibitor. Initial velocities were measured in a final volume of 0.7 mL that

contained 50 mM potassium phosphate, pH 8.0, 100 mM KCl, 0.4 mM OAA, 0.3 mM DTNB, varied AcCoA, and several fixed concentrations of AcMX. Reactions were initiated by the addition of TpCSH6 (0.6 mg). Lineweaver-Burk plots showed a competitive inhibition pattern. All initial velocity data were globally fit to a Michaelis-Menten equation in which $KM_{app} = KM(1 + [AcMX]=Ki)$.

Ligand affinity measurements

Fluorescence emission spectra (excitation 295 nm) were recorded using a Fluoromax-3 (Horiba) spectrofluorimeter at 298 K. Emission spectra were corrected for dilution and, using a control titration of N-acetyl-l-tryptophanamide, the inner filter effect due to OAA. Titration data monitoring changes in the fluorescence emission intensity at 315 nm (F) were plotted by normalizing F by the emission intensity measured in the absence of titrant (Fo). Protein-ligand affinities were determined by fits to Eqn. 1 (for Kd=[E] > 5, where [E] is the subunit concentration of the enzyme) or Eqn. 2, which accounts for changes in [L] (either [OAA] or [AcMX]) due to ligand depletion.

$$F = F_0 + \frac{\Delta F[L]}{K_d + [L]} \quad (1)$$

$$F = F_0 + \frac{\Delta F}{2[E]}([L] + K_d + [E] + \sqrt{[L] + K_d + [E]^2 + 4[L][E]} \quad (2)$$

Crystallization

Sparse-matrix crystallization screens performed using the Wizard I and II kits (Emerald Bio) yielded two hits after 27 d: condition I-1 [20% PEG 8000, 0.1 M 2-(cyclohexylamino)-ethanesulfonate (CHES) pH 9.5] and condition I-26 (Table 2), each supplemented with 1 mM OAA. Crystals with a similar appearance were obtained in the

same buffer after 10 d in drops (2–4 ml prior to mixing with an equal volume of reservoir solution) containing 8–10% PEG 4000 and 5 mg ml1 TpCSH6 with or without OAA. Single crystals were loaded into nylon loops (Teng, 1990), transferred to reservoir solution supplemented with 15%(w/v) sorbitol for 10 min, rapidly immersed in liquid nitrogen and maintained at or below 100 K until data collection was complete.

Table 2.2 Crystallization

Method	Hanging-drop vapor diffusion
Plate type	VDX 24-well tray, Hampton Research
Temperature (K)	294
Protein concentration (mg ml^{-1})	5
Buffer composition of protein solution	20 m*M* Tris–HCl pH 8.0, 1 m*M* EDTA, 1 m*M* oxaloacetate
Composition of reservoir solution	0.1 *M* CHES pH 9.5, 12%(*w*/*v*) PEG 4000, 1 m*M* oxaloacetate
Volume and ratio of drop	2 µl (1:1 ratio)
Volume of reservoir (ml)	0.5

Data collection and processing

All screened crystals diffracted X-rays weakly and with high mosaicity. The best diffraction patterns were obtained from a TpCSH6 crystal that adhered to the side of the mounting loop. The unusual sample geometry hampered the collection of a complete X-ray diffraction data set, which was recorded in three passes using different regions of the crystal. Diffraction data from one-pass, two-pass or three-pass sets were processed using the HKL-2000 suite (Otwinowski & Minor, 1997). Single-pass data sets had similar statistics (not shown), including individual Rsym values that were comparable to the Rmerge value for the full (three-pass) data set (Table 3).

Table 2.3
Data collection and processing.
Values in parentheses are for the outer shell.

Diffraction source	21-ID-G, APS
Wavelength (Å)	0.97856
Temperature (K)	100
Detector	MAR Mosaic 300 mm CCD
Crystal-to-detector distance (mm)	200, 247.8 and 250
Rotation range per image (°)	0.5, 1.0 and 1.0
Total rotation range (°)	93, 122 and 360
Exposure time per image (s)	3.0, 2.8 and 3.5
Space group	$P2_1$
a, b, c (Å)	56.505, 113.406, 120.066
α, β, γ (°)	90, 95.08, 90
Resolution range (Å)	50–2.18 (2.24–2.18)
Total No. of reflections	983117
No. of unique reflections	76084
Completeness (%)	97.2 (97.0)
Multiplicity	12.9 (13.5)
$\langle I/\sigma(I)\rangle$	11.8 (2.1)
R_{meas}	0.249 (1.400)
$R_{p.i.m.}$	0.085 (0.422)
$CC_{1/2}$	0.993 (0.762)
Overall B factor from Wilson plot (Å^2)	24.9

Structure solution and refinement

PHENIX and Coot were used for structure solution and refinement (Emsley et al., 2010; Adams et al., 2010). Molecular replacement was performed with Phaser (McCoy et al., 2007) using subunit A from PDB entry 2ifc, with all buffer components and side-chain atoms beyond C removed, as the search model. The sole solution contained four subunit in the asymmetric unit (residues 4–383; the TpCS numbering excludes Met0). One round of phenix.autobuild (with default settings) was performed to repair side chains. Iterative cycles of model improvement and refinement, using noncrystallographic symmetry (NCS) restraints and a hybrid TLS–isotropic ADP model, were performed until Rfree appeared to

converge. The C-terminal appendage (residues Val386– His399) was added using Coot. NCS restraints were dropped in the final refinement cycles. MolProbity was used to check the protein geometry (Chen et al., 2010). Pairwise alignments and root-mean-square deviation (r.m.s.d.) computations were performed using one cycle of the align algorithm implemented in PyMOL (v.1.7.4.2; DeLano, 2002). Domain motions were computed using the DynDom server (v.1.5; default settings; Hayward & Berendsen, 1998; Hayward & Lee, 2002). Protein images were based on PyMOL or LIGPLOT (Wallace et al., 1995) output.

2.3 Results and Discussion

Comparison of TpCSH6 and TpCS

TpCSH6 was overexpressed in E. coli, purified and found to be a dimer (Figure 2.1) with a specific activity of 52 U mg^{-1} at 328 K and 22 U mg^{-1} at 298 K (8 s^{-1}, assuming one active site per subunit). Substrate-saturation analyses (Figure 2.2) yielded Michaelis constant (K_M) values of 3.0 mM for AcCoA and 5.2 mM for OAA. AcMX was a competitive inhibitor versus AcCoA (Ki = 20 µM; Figure 2.3). These results, and the relatively high batch-to-batch variability in specific activity, are comparable to those for TpCS (Sutherland et al., 1991; Kurz et al., 2000).

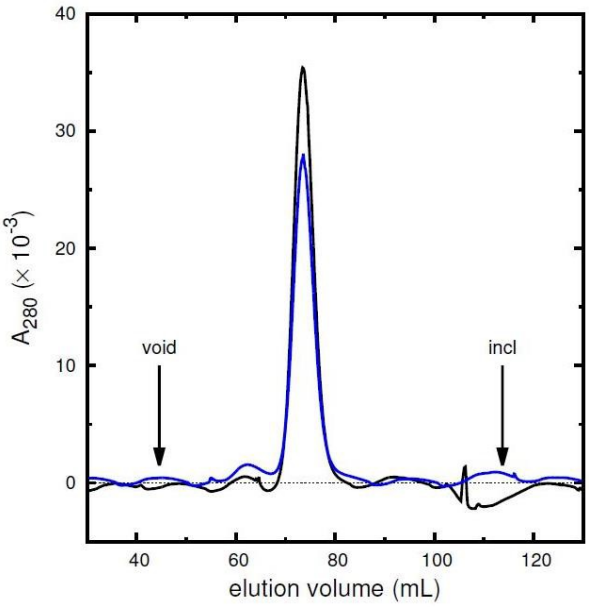

Figure 2.1. Gel filtration analysis of TpCSH6 (black trace) and TpCSH6-H222Q (blue trace) at 277 K in 50 mM Tris HCl, pH 8.0, and 100 mM KCl. Molecular size analysis was performed as described previously (Mullins et al., 2013). The arrows indicate the elution volumes for Blue Dextran (void) and acetone (incl) standards. Each elution profile reaches a maximum at 73.6 mL (81 kDa), as expected for a dimer of 43 kDa subunits.

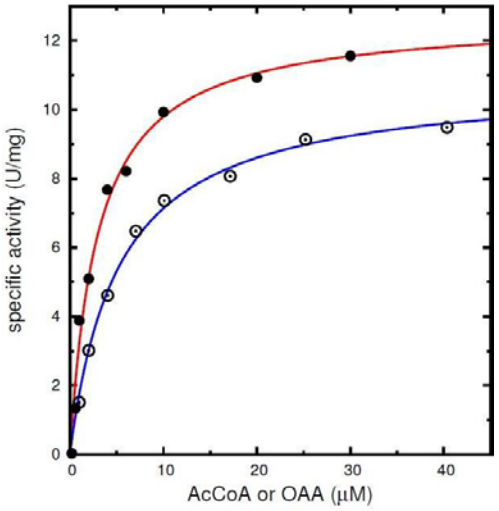

Figure 2.2. Determination of steady-state kinetic parameters for TpCSH6. Specific activities were measured using the DTNB assay at 298 K for AcCoA at 0.4 mM OAA (filled circles) or OAA at 15 M AcCoA (open circles). Solid lines depict fits to to the Michaelis-Menten equation: AcCoA, K_M = 3.0±0.4 µM and V_{max} = 12.7±0.5 U/mg; OAA, K_M = 5.2±0.4 µM and V_{max} = 10.8±0.2 U/mg.

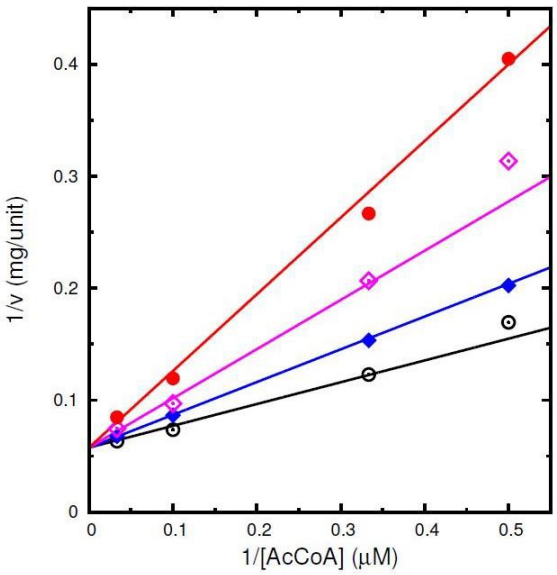

Figure 2.3. Determination of a competitive inhibition constant (Ki) for AcMX. Global fit parameters were: K_M = 3.3±0.2 µM, K_i = 19.9±2.1 µM, and V_{max} = 17.4±0.3 U/mg. [Phosphate weakly inhibits TpCS (Kurz et al., 2009).] The solid lines represent curves computed using global fit parameters at 0 (black open circles), 10 µM (blue filled diamonds), 25 µM (purple open diamonds), and 50 µM (red filled circles) AcMX.

Purified TpCSH6-H222Q, a mutant located in the AcCoA binding site, had a specific activity of 0.01 U mg1 at 298 K or 0.05% of that of the wild type. Since the mutant enzyme was isolated from a gltA+ E. coli strain, the observed activity could be associated with a contaminating host enzyme. However, the 'activity' did not increase as AcCoA was varied from 30 to 400 mM (at 0.4 mM OAA; data not shown), which suggests that host CS is not present. We conclude that TpCSH6-H222Q is nearly or completely devoid of enzymatic activity, and that the protein-isolation method can be used to study even very low-activity mutants produced in common protein-production strains.

Fluorescence titrations were used to measure OAA dissociation constants (Kd) of 0.76 and 19 µM for TpCSH6 and TpCSH6-H222Q, respectively (Figure 2.4). Saturating OAA quenched the fluorescence of both forms to about half of the initial level, which differs

from a report that TpCS-H222Q fluorescence is quenched to a relatively greater extent (Kurz et al., 2009). As observed for TpCS, the addition of AcMX to the TpCSH6–OAA complex results in a 124% increase in fluorescence (Kd = 1.5 µM) owing to the formation of CitMX (Figure 2.5). The Kd values determined for untagged TpCS(-H222Q) at 293 K were comparable: 1.3, 33 and 1.47 µM, respectively (Kurz et al., 2005, 2009).

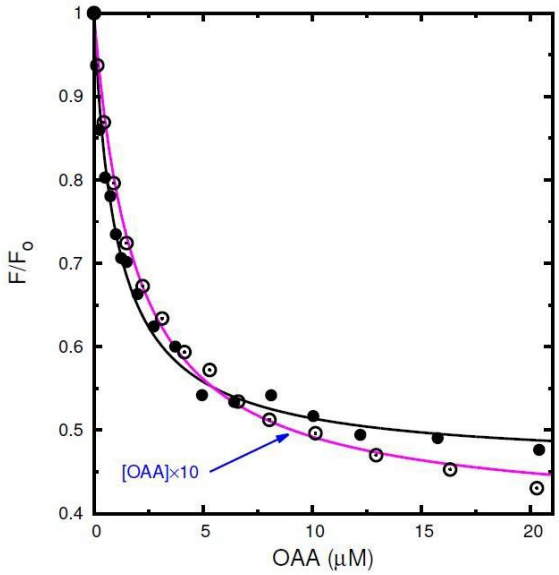

Figure 2.4. OAA affinities determined by fluorescence titration. OAA titrations were performed by adding aliquots to a constantly stirred 2 mL volume that contained 50 mM EPPS, pH 8.0, 0.1 mM EDTA, and either TpCSH6 or TpCSH6-H222Q. Spectra were recorded 3 min after each ligand addition. The OAA-dependent quenching of TpCSH6 (0.2 µM, filled circles) or TpCSH6-H222Q (1 µM, open circles) were analyzed by fits to Eqn. 2 and Eqn. 1, respectively. Solid lines depict fits for TpCSH6 (black curve) and TpCSH6 (purple curve), divided by Fo: Kd = 0.76±0.06 and 19±1 µM and maximal (e.g., [OAA] → ∞ 1) -ΔF=Fo = 0.541 and 0.603, respectively. Note that [OAA] in the TpCSH6-H222Q titration was 10-fold higher than indicated on the abscissa.

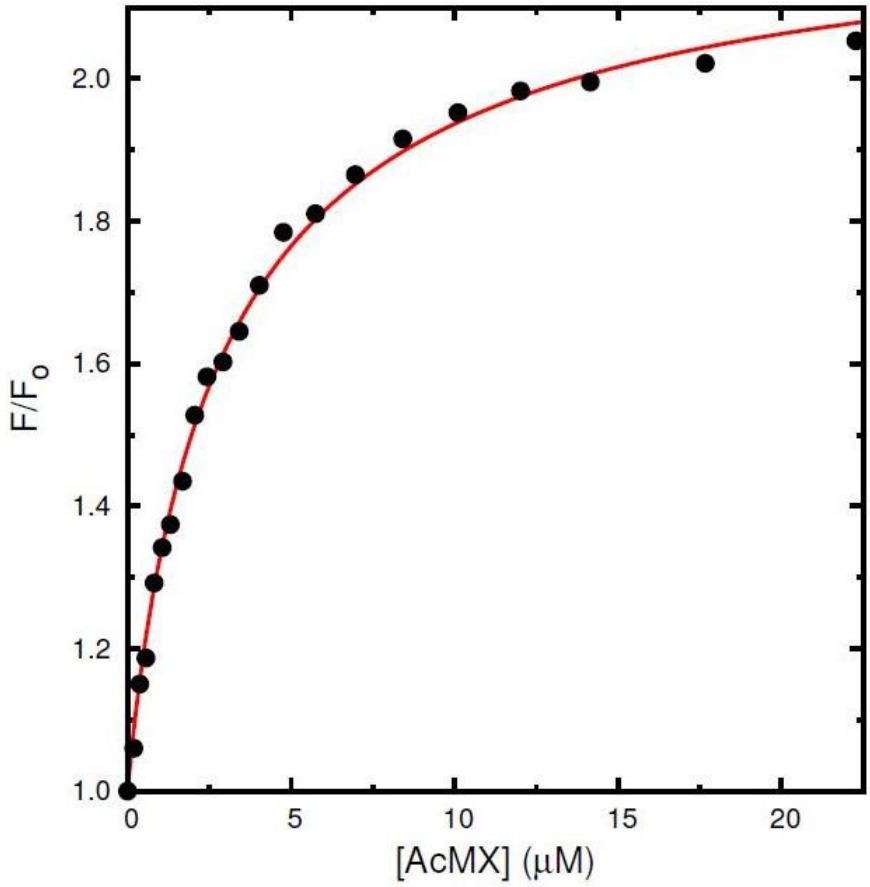

Figure 2.5. AcMX affinity for TpCSH6OAA determined by fluorescence titration. Experimental conditions were the same as described in Fig. 2.4, except that 0.2 mM OAA was also present. The AcMX-dependent increase in F is due to conversion of the fluorescence quencher OAA to CitMX. The solid line depicts a fit of the titration data to Eqn. 2, divided by Fo, with Kd = 1.5±0.1 μM and maximal F=Fo = 1.24± 0.01.

Crystal structure of TpCSH6

Initial attempts to crystallize TpCSH6 focused on HEPES/sodium acetate (pH 7.5–8.5) conditions, identified by robotic screening that yielded crystals of TpCS bound to one or more ligands (Christopher Lehmann, unpublished observations). No suitable TpCSH6 crystals were obtained in attempts to manually reproduce these conditions. A sparse-matrix screen identified high-pH conditions that yielded large crystals (Table 2). The

inclusion of OAA in the crystallization solution (Table 2) had no obvious effect on crystal morphology. A cryocooled crystal (0.1 0.1 1.0 mm) grown in the presence of OAA was selected for X-ray data collection. Several attempts to crystallize TpCSH6-H222Q under similar conditions yielded only microcrystals.

The three-pass data set was selected for further analysis because the completeness and electron-density maps (Figure 2.6) were superior to those computed using the one-pass or two-pass data sets (not shown). Molecular replacement and refinement proceeded smoothly, furnishing a final model with acceptable statistics (Table 4). Like TpCS (Russell et al., 1994), TpCSH6 crystallized in space group P21 with two dimers in the asymmetric unit, albeit with rather different unit-cell parameters (Table 3). TpCSH6 had almost the same monomer topology as unliganded TpCS (Figure 2.7). Pairwise alignments of TpCS (coordinates provided by Linda C. Kurz) and TpCSH6 subunits gave r.m.s.d. values of 0.40–0.59 A ° (C only) and 1.15– 1.25 A ° (all protein atoms). Pairwise alignments of the TpCSH6 subunits (residues 5–383) gave r.m.s.d. values of 0.26–0.42 A ° (C only) and 0.68–0.91 A ° (all protein atoms). TpCSH6 subunit C and the CD dimer were selected to represent the open conformation in all subsequent comparisons.

Table 2.4

Structure refinement.
Values in parentheses are for the outer shell.

Resolution range (Å)	29.15–2.18 (2.24–2.18)
Completeness (%)	89.8 (76.0)
σ Cutoff	0
No. of reflections, working set	70618 (4415)
No. of reflections, test set	1867 (126)
Final R_{cryst}	0.1642 (0.2385)
Final R_{free}	0.2118 (0.2965)
No. of non-H atoms	
Protein (all atoms)	12251
Protein (His_6-tag atoms)	277
Ligand	8
Water	868
Total	13127
R.m.s. deviations	
Bonds (Å)	0.012
Angles (°)	1.139
Average *B* factors (Å^2)	
Protein (all atoms)	33.8
Protein (His_6-tag atoms)	63.6
Ligand	45.5
Water	36.7
Ramachandran plot	
Favoured regions (%)	97.93
Additionally allowed (%)	2.01
Outliers (%)	0.06
MolProbity clashscore†	4.86
MolProbity overall score	1.08

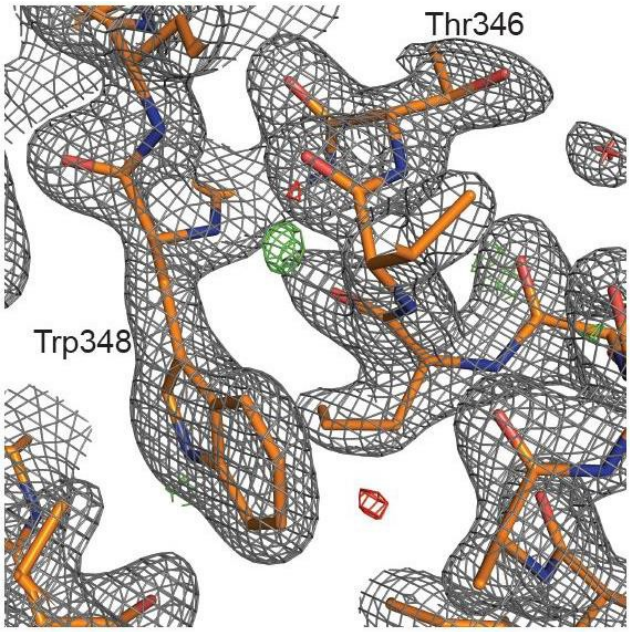

Figure 2.6. Representative map-model agreement. Electron density maps near Trp348 (subunit C) are shown: A-weighted 2mFo–DFc (grey mesh, 1:5) and mFo–DFc (green and red mesh, 3). The Trp348 rotamer, which is essentially the same as in liganded TpCS structures, is flipped (-171 rotation) relative to the rotamer observed in the structure of TpCS (Russell et al., 1994).

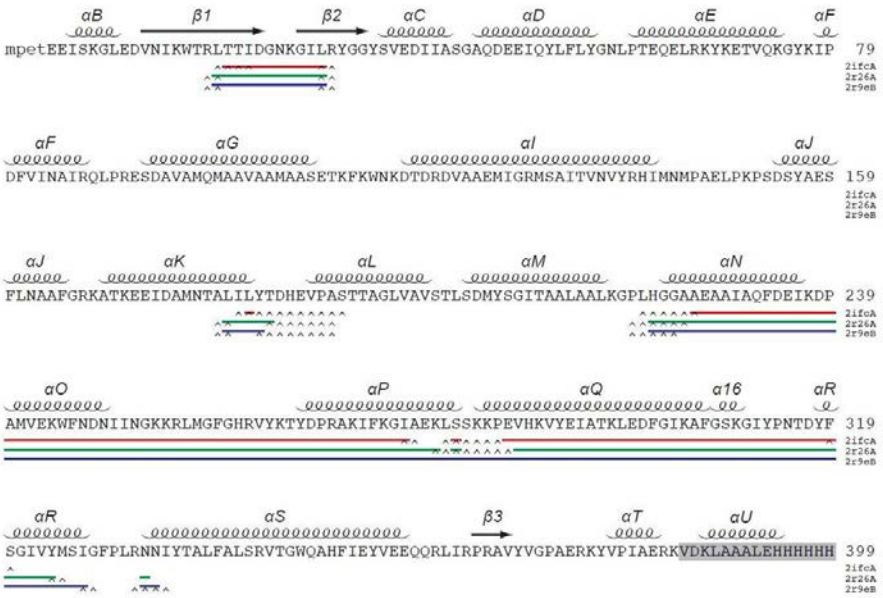

Figure 2.7. Primary sequence, secondary structure, and domain motions in TpCS(H6). The C-terminal appendage of TpCSH6 is indicated with a grey background. In keeping with prior practice, the initiator codon is assigned the number zero. The elements of secondary structure are given the same designations as in TpCS, apart from a short helix (16) and C-terminal appendage helix (U) that were not present in the apo TpCS structure. The colored symbols correspond to mobile domains (underlined) and hinge residues (carets) identified by DynDom comparisons of TpCSH6 with one ligand-bound TpCS subunit.

As expected for a relatively long exposure to synchrotron X-rays, alterations consistent with mild X-ray damage were observed, including Asp/Glu decarboxylation and loss of methanethiol in surface-accessible residues (Garman, 2010) such as Asp301B and Met241C. Two well ordered bicarbonate ligands were included in the final model. This was justified by the high pH of the mother liquor and the presence of OAA, which can spontaneously decarboxylate. These anions 'cap' the N-terminal (positive) end of the long Q helix in subunits B and C. The side chain of the single Ramachandran outlier, Lys237C, makes a well defined salt bridge with the side chain of Glu158D from a neighboring asymmetric unit. Positive difference electron density was observed early in refinement at two locations: a helix near the CD dimer interface and the nearby subunit D active site.

These features were linked to form the C-terminus of subunit A. Dimers AB and CD are bridged at the center of the asymmetric unit by two C-terminal appendages extending from subunits A and D (Figure 2.8). The C-terminal native sequence of subunit A wraps halfway around the large domain of the B subunit. The C-terminal tag sequence continues past helix T towards the CD interface, making a perpendicular turn to form the extra helix (U). A second sharp turn near residue His222D directs the tag sequence into the active site of subunit D, ending with a bidentate salt bridge formed between the C-terminal carboxylate of the tag residue His399A and the rg271D guanidinium. A similar interaction is formed between the C-terminus of subunit D and the active site of subunit A. NCS comparisons indicate the backbones diverge after Arg383, with helix U displaced along its axis about 2 A ° farther from the CD dimer than the AB dimer. No electron density consistent with the C-terminal appendage of subunits B or C was observed. Small affinity-tag appendages occasionally form crystal-packing contacts (Carson et al., 2007). The TpCSH6 His6 tag is one of a small number of ordered affinity tags that bind to an enzyme active site (Taylor et al., 2005; McDonald et al., 2007; Singh et al., 2011; Wojtkowiak et al., 2012).

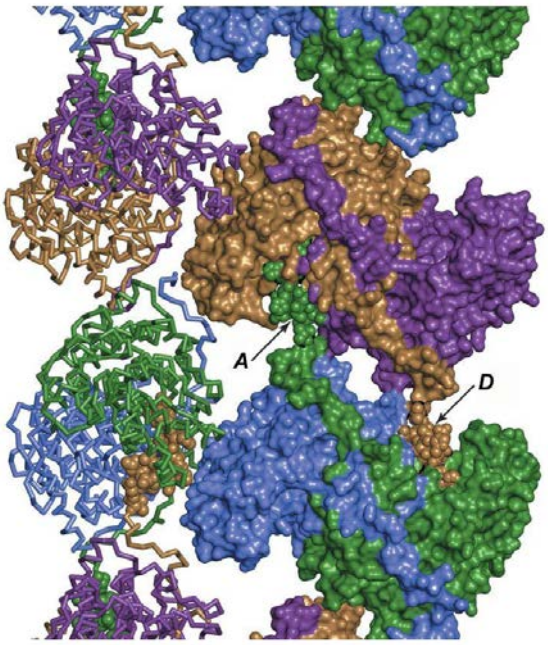

Figure 2.8. Crystal-packing diagram for TpCSH6. Subunits A–D in the monoclinic asymmetric unit are colored green, blue, purple and gold, respectively. Residues in the C-terminal appendage, shown as spheres in subunits A and D (indicated by arrows), occupy the active sites of subunits D and A, respectively. Left, ribbon rendering shows that the C-termini bind deep within the AB and CD dimers. In this orientation, the twofold screw axis (b axis) runs along the Cartesian x axis. The C-terminal appendage contacts active-site residues involved in binding both OAA and AcCoA (Figure 2.9). This was unexpected, as the hexahistidine sequence has no resemblance to either substrate. The C-terminal residue His399 makes a side-chain contact with His222, a residue that provides a hydrogen bond (involving N1) that polarizes the AcCoA enolate, and the terminal carboxylate contacts both His262 and Arg271, which bind carbonyl and -carboxylate O atoms in OAA. Since the His399–His222 contact involves two N1 atoms, one residue adopts a tautomer (N1–H), which is uncommon at high pH (Sudmeier et al., 2003; Li & Hong, 2011) but is employed by some active-site residues (Day et al., 2003). The local hydrogen-bonding context and the proposed role for the neutral tautomer in the condensation reaction (summarized in van der Kamp et al., 2007) suggest that His222 adopts the tautomer even in the absence of acetyl-CoA. Similarly, flipping the His398 imidazole would worsen the hydrogen-bonding context and introduce clashes, which suggests it may also adopt a tautomer stabilized by Ala191 NH (Fig. 2). His397 N"2 forms a hydrogen bond to one carboxylate O atom in the critical active-site base Asp317, which is not directly contacted by either substrate (Figure 2.10). Similar contacts are observed between Asp317 equivalents and strong inhibitors such as CMCoA and CMX (Usher et al., 1994; Francois et al., 2006)

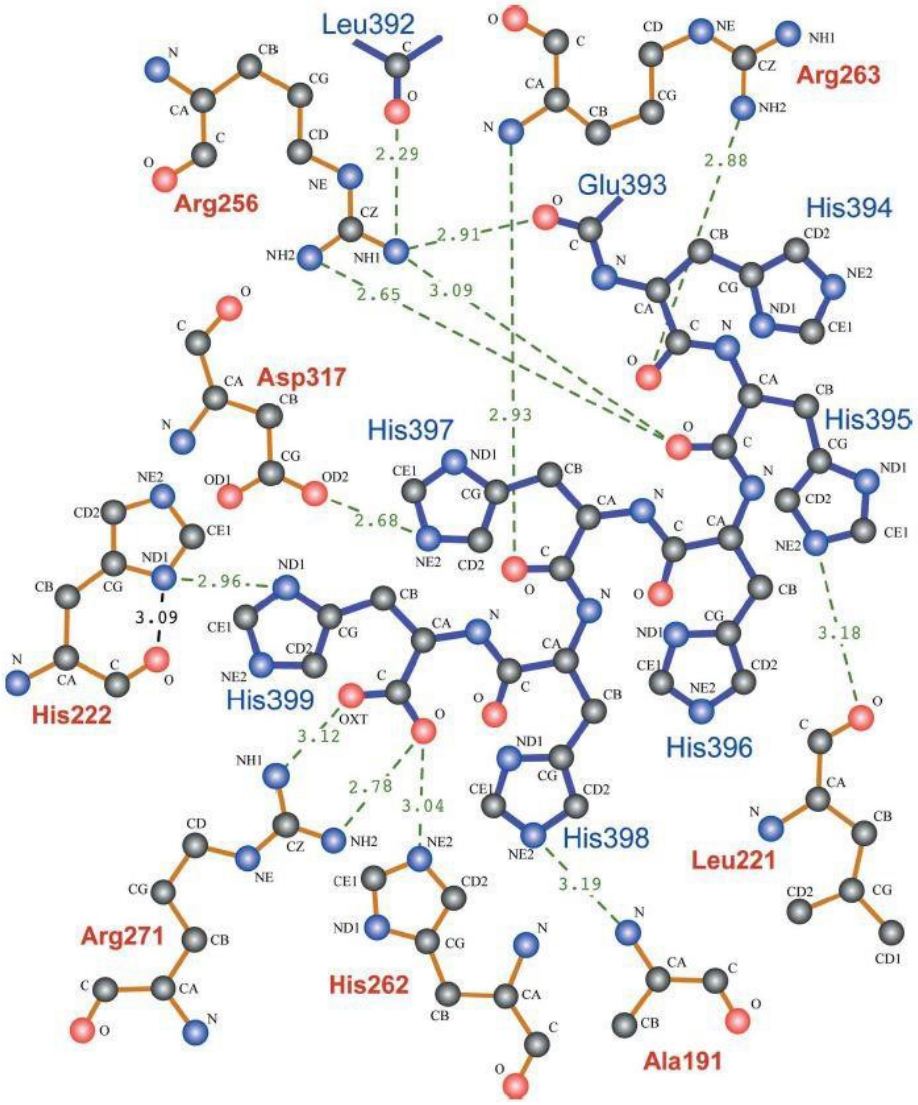

Figure 2.9. Active site of TpCSH6 subunit A bound to the C-terminus of subunit D (blue bonds). All illustrated residues also contact OAA (His262 and Arg271) or AcCoA (the remainder). His222 and Asp317 are responsible for deprotonating the AcCoA acetyl group, stabilizing the resulting enolate/carbanion and promoting the condensation reaction that produces CitCoA. An intra-residue hydrogen bond that stabilizes the neutral tautomer of His222 is shown in black. A similar analysis of the TpCS active site bound to the CitCoA analogue CitMX (Figure 2.10) shows that many of the same residues are involved in substrate contacts. All polar contacts presumed to result in hydrogen-bonding interactions are shown, with distances in Å

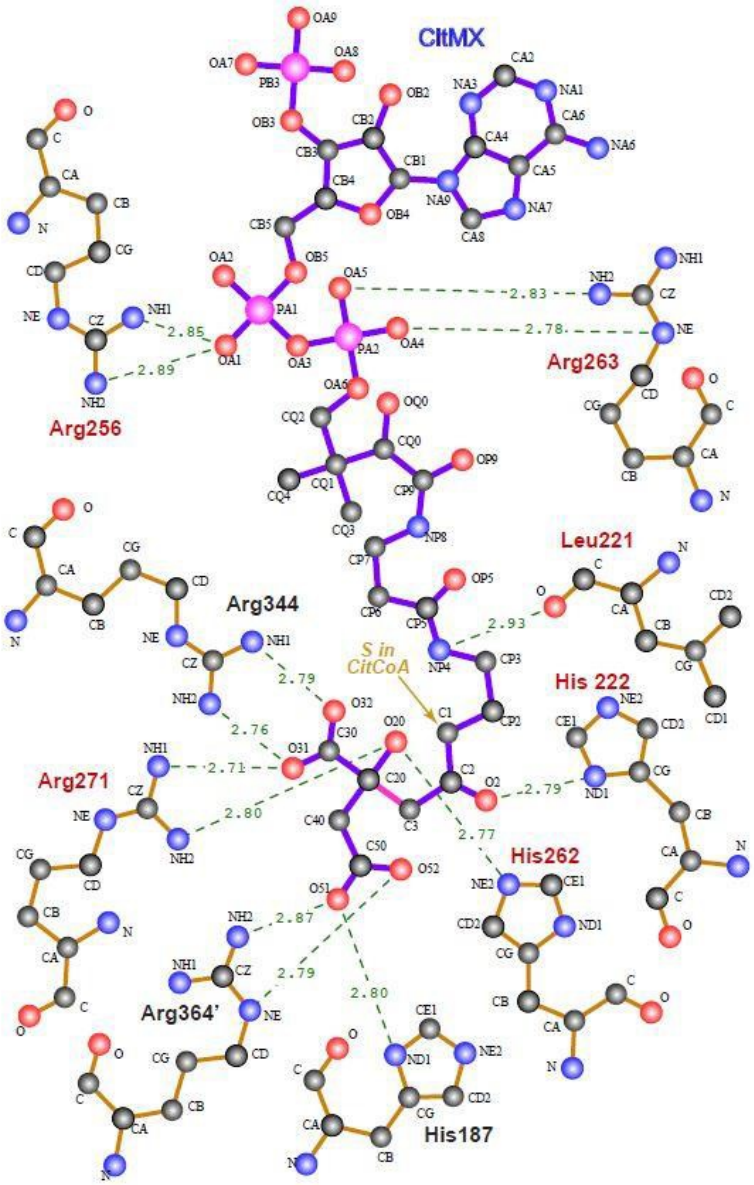

Figure 2.10. Active site of TpCS CitMX complex (PDB entry 2r9e) showing selected polar protein-ligand interactions. CitMX differs from CitCoA by an atomic substitution (S→CH2) indicated with an arrow. TpCS forms CitMX by condensing AcMX and OAA, forming the bond denoted in magenta. Residues with names shown in red are also involved in binding the C-terminus of TpCSH6 subunit A or D (Fig. 2.2). The prime denotes a residue from the partner subunit in the TpCS dimer; note that the C-terminus only engages residues from one subunit. Polar contacts with the CoA region by Leu257, Gly259, Phe260, Asn315, and Arg 361 are omitted.

Bisubstrate analogues can be potent and selective enzyme inhibitors (Collins & Stark, 1971; Radzicka & Wolfenden, 1995; Schramm, 2013). Clinically useful examples include finasteride, which is converted to a tight-binding bisubstrate analogue by its target enzyme (Bull et al., 1996). The stoichiometric ligand CitMX is a bisubstrate analogue inhibitor of CS that (like finasteride) is formed by its target enzyme (Kurz et al., 2009). Reversible formation of CitMX by TpCS might therefore contribute to inhibition by AcMX (Martin et al., 1994), although its potency could be sapped by harnessing 'binding energy' to drive the condensation reaction (Page & Jencks, 1971). CS is a highly specific enzyme that possesses a highly basic active site that binds two polyanionic substrates. All known potent CS inhibitors are unpromising starting points for drug design: they closely resemble the substrates and would encounter substantial barriers to cellular uptake. In contrast, imidazoles should be mostly uncharged at the basic pH, which may allow crystal growth by alleviating electrostatic repulsion between the active site and the His6 tail. This near-neutral peptide ligand could represent a useful alternative starting point for the identification of CS inhibitors.

To test the hypothesis that the CS active site has detectable affinity for a poly-His ligand, TpCSH6 was incubated with a dansyl-His3 synthetic peptide (Genscript, Piscataway, New Jersey, USA). Fluorescence changes consistent with Förster resonance energy transfer between the tripeptide and TpCSH6, presumably the nearby Trp115, were not observed (data not shown). Gel-filtration studies indicated that unliganded TpCS, TpCSH6 and TpCSH6-H222Q were each exclusively dimeric in solution (Fig. 2.1). Deletion of a hydrogen bond between the active-site residue His222 and the appendage residue

His399 appears to thwart TpCSH6-H222Q crystal growth. This sensitivity suggests a weak peptide–protein interaction that is stabilized by cooperative crystal-packing interactions.

TpCS conformational changes associated with ligand binding

Substrate exclusion by the C-terminal appendage could explain why the crystal morphology was unaffected by the addition of saturating OAA but only half of the active sites are occupied by peptide in the crystal (ordered solvent is observed in the other two active sites). The striking finding that all four subunits adopt open conformations suggests that the TpCS dimer cannot close just one active site. Previous CS crystal structures have a high degree of NCS and contain the same ligand(s) in both active sites. Since to our knowledge there is no evidence for cooperative binding of OAA by any CS, it is possible that the open conformation is trapped within the crystalline lattice.

The preferred rotamer at Trp348, or the residue occupying this position, has been reported to change upon ligand binding and concomitant enzyme closure (Kurz et al., 2005). The TpCS structure possesses m95 (Trp348A) and p90 (Trp348B) rotamers (Russell et al., 1994), each modeled with a C—C—C bond-angle outlier (> 5.5). In TpCSH6 and the three deposited TpCS structures, however, only m0 rotamers were observed in unambiguous electron density in all subunits (Figure 2.6). It is possible that binding of the C-terminal appendage to the TpCSH6 active site, which does not cause domain closure, triggers a Trp348 ring flip. A simpler model, however, is that the Trp348 indole does not ring flip, consistent with the fluorescence properties, which indicate a rigidly immobilizing protein environment (Kurz et al., 2005).

Using the new TpCSH6 structure as a reference, we examined the series of protein conformational changes associated with ligand binding, domain closure and the condensation reaction (Figure 2.7). As anticipated, the binding of OAA is associated with a conspicuous closure of the active site: a rotation of the small domain relative to the large domains that form the major dimer interface (Figure 2.11a). Each of the domains is relatively monolithic, with pairwise r.m.s.d. values of <1 Å, and similar sets of hinge residues are involved. This motion is similar to the larger (19.4) rotation observed in the canonical vertebrate CS open/closed pair (PDB entries 1cts/1csh; Remington et al., 1982; Usher et al., 1994; Hayward & Berendsen, 1998). Domain closure increases when a CoA analogue is also present (Figures 2.11b and 2.11c). As noted above, the TpCS–OAA–CMCoA and TpCS–CitMX complexes adopt similar protein structures, suggesting that they both represent the configuration associated with the condensation reaction.

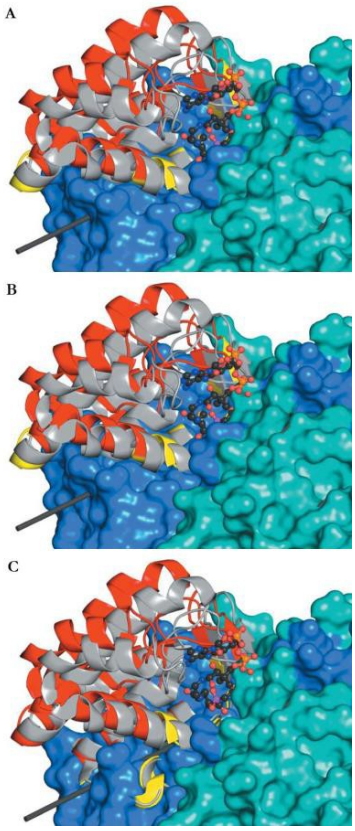

Figure 2.11. Domain motions in TpCS(H6). Each panel shows the open TpCSH6 structure superimposed on a closed TpCS structure in pairwise DynDom analyses. The static portion, mainly the large domains that form the majority of the dimer interface, is shown as a surface rendering. The mobile domain extends from the surface and is shown in cartoon rendering, with the TpCSH6 mobile region colored red and the closed structure colored grey. Hinging residues in each TpCSH6 domain are colored yellow. Residues involved in each pairwise comparison are shown in Figure 2.7. The rotation axis is shown as a black bar; closure results in clockwise rotations about this axis. (a) Comparison with the TpCS–OAA complex (PDB entry 2ifc subunit A) shows 52% closure and a 8.9 rotation (translation of 0.1 Å). Mobile domain: 99 residues, r.m.s.d. 0.41 Å . Static domain: 277 residues, r.m.s.d. 0.52 Å. (b) Comparison with the TpCS–OAA– CMCoA complex (PDB entry 2r26 subunit A) shows 86% closure and a 10.6 rotation (translation of 0.4 Å). Mobile domain: 115 residues, r.m.s.d. 0.68 Å. Static domain: 258 residues, r.m.s.d. 0.69 Å. CMCoA is a tight-binding analogue of the deprotonated AcCoA formed during the condensation reaction. (c) Comparison with the TpCS–CitMX complex (PDB entry 2r9e subunit B) shows 82% closure and a 10.3 rotation (translation 0.4 Å). Mobile domain: 123 residues, r.m.s.d. 0.83 Å. Static domain: 252 residues, r.m.s.d. 0.7 Å. CitMX is formed from AcMX and OAA, presumably within the crystal.

2.4 Conclusions

TpCSH6 is an active enzyme useful for solution studies of the CS mechanism. It unexpectedly produced a new crystal form that appears to prevent ligand cocrystallization. The serendipitous peptide ligand, with a total charge of near zero, binds both parts of the CS active site. Using this complex as an inspiration, it may be possible to identify an alternative drug scaffold to target this key step in primary metabolism.

2.5 Acknowledgments

We thank Joshua A. Mosberg for constructing pJK438, Jason Markovich for initial protein-expression trials, Elwood A. Mullins for help with X-ray data collection, Kelly L. Sullivan for performing gel-filtration analysis, Barbara L. Golden and Jeremy R. Lohman for processing X-ray data and Linda C. Kurz for materials, advice related to CS and discussions of CS conformational dynamics. This research used the resources of the Advanced Photon Source, a US Department of Energy (DOE) Office of Science User Facility operated for the DOE Office of Science by Argonne National Laboratory under Contract No. DE-AC02-06CH11357. Use of LS-CAT Sector 21 was supported by the Michigan Economic Development Corporation and the Michigan Technology Tri-Corridor (Grant 085P1000817).

2.6 References

1. Adams, P. D. et al. (2010). Acta Cryst. D66, 213–221.

2. Aleksandrov, A., Zvereva, E. & Field, M. (2014). J. Phys. Chem. B, 118, 4505–4513.

3. Bayer, E., Bauer, B. & Eggerer, H. (1981). Eur. J. Biochem. 120,155–160.

4. Bloxham, D. P., Ericsson, L. H., Titani, K.,Walsh, K. A. & Neurath, H. (1980). Biochemistry, 19, 3979–3985.

5. Bradford, M. M. (1976). Anal. Biochem. 72, 248–254.

6. Bull, H. G., Garcia-Calvo, M., Andersson, S., Baginsky, W. F., Chan, H. K., Ellsworth, D. E., Miller, R. R., Stearns, R. A., Bakshi, R. K., Rasmusson, G. H., Tolman, R. L., Myers, R. W., Kozarich, J. W. & Harris, G. S. (1996). J. Am. Chem. Soc. 118, 2359–2365.

7. Carson, M., Johnson, D. H., McDonald, H., Brouillette, C. & DeLucas, L. J. (2007). Acta Cryst. D63, 295–301.

8. Chen, V. B., Arendall, W. B., Headd, J. J., Keedy, D. A., Immormino, R. M., Kapral, G. J., Murray, L. W., Richardson, J. S. & Richardson, D. C. (2010). Acta Cryst. D66, 12–21.

9. Collins, K. D. & Stark, G. R. (1971). J. Biol. Chem. 246, 6599–6605.

10. Constantine, C. Z. (2009). PhD thesis. Washington University in St Louis, St Louis, Missouri, USA.

11. Daidone, I., Roccatano, D. & Hayward, S. (2004). J. Mol. Biol. 339, 515–525.

12. Danson, M. J., Black, S. C., Woodland, D. L. & Wood, P. A. (1985). FEBS Lett. 179, 120–124.

13. Day, R. M., Thalhauser, C. J., Sudmeier, J. L., Vincent, M. P., Torchilin, E. V., Sanford, D. G., Bachovchin, C. W. & Bachovchin, W. W. (2003). Protein Sci. 12, 794–

14. DeLano, W. L. (2002). PyMOL. http://www,pymol.org.

15. Donini, O., Darden, T. & Kollman, P. A. (2000). J. Am. Chem. Soc. 122, 12270–12280. 16. Eggerer, H. (1965). Biochem. Z. 343, 111–138.

17. Emsley, P., Lohkamp, B., Scott, W. G. & Cowtan, K. (2010). Acta Cryst. D66, 486–501.

18. Francois, J. A., Starks, C. M., Sivanuntakorn, S., Jiang, H., Ransome, A. E., Nam, J.-W., Constantine, C. Z. & Kappock, T. J. (2006). Biochemistry, 45, 13487–13499.

19. Garman, E. F. (2010). Acta Cryst. D66, 339–351.

20. Gottschalk, G. & Barker, H. A. (1966). Biochemistry, 5, 1125–1133.

21. Hayward, S. & Berendsen, H. J. C. (1998). Proteins, 30, 144–154.

22. Hayward, S. & Lee, R. A. (2002). J. Mol. Graph. Model. 21, 181–183.

23. Kamp, M. W. van der, Perruccio, F. & Mulholland, A. J. (2007). Proteins, 69, 521–535.

24. Kamp, M.W. van der, Perruccio, F. &Mulholland, A. J. (2008). Chem. Commun., pp. 1874.

25. Kamp, M. W. van der, Z˙ urek, J., Manby, F. R., Harvey, J. N. & Mulholland, A. J. (2010). J. Phys. Chem. B, 114, 11303–11314.

26. Karpusas, M., Branchaud, B. & Remington, S. J. (1990). Biochemistry, 29, 2213–2219.

27. Kobylarz, M. J., Grigg, J. C., Sheldon, J. R., Heinrichs, D. E. & Murphy, M. E. P. (2014). J. Biol. Chem. 289, 33797–33807.

28. Kurz, L. C., Constantine, C. Z., Jiang, H. & Kappock, T. J. (2009). Biochemistry, 48, 7878–7891.

29. Kurz, L. C., Drysdale, G., Riley, M., Tomar, M. A., Chen, J., Russell, R. J. M. & Danson, M. J. (2000). Biochemistry, 39, 2283–2296.

30. Kurz, L. C., Fite, B., Jean, J., Park, J., Erpelding, T. & Callis, P. (2005). Biochemistry, 44, 1394–1413.

31. Kurz, L. C., Roble, J. H., Nakra, T., Drysdale, G. R., Buzan, J. M., Schwartz, B. & Drueckhammer, D. G. (1997). Biochemistry, 36, 3981–3990.

32. Kurz, L. C., Shah, S., Crane, B. R., Donald, L. J., Duckworth, H. W. & Drysdale, G. R. (1992). Biochemistry, 31, 7899–7907.

33. Li, S. & Hong, M. (2011). J. Am. Chem. Soc. 133, 1534–1544. Martin, D. P., Bibart, R. T. & Drueckhammer, D. G. (1994). J. Am. Chem. Soc. 116, 4660–4668.

34. McCoy, A. J., Grosse-Kunstleve, R. W., Adams, P. D., Winn, M. D., Storoni, L. C. & Read, R. J. (2007). J. Appl. Cryst. 40, 658–674.

35. McDonald, H. M., Pruett, P. S., Deivanayagam, C., Protasevich, I. I., Carson, W. M., DeLucas, L. J., Brouillette,W. J. & Brouillette, C. G. (2007). Acta Cryst. D63, 891–905.

36. Mulholland, A. J., Lyne, P. D. & Karplus,M. (2000). J. Am. Chem. Soc. 122, 534–535.

37. Mullins, E. A., Sullivan, K. L. & Kappock, T. J. (2013). PLoS One, 8, e67901.

38. Otwinowski, Z. & Minor,W. (1997). Methods Enzymol. 276, 307–326.

39. Page, M. I. & Jencks, W. P. (1971). Proc. Natl Acad. Sci. USA, 68, 1678–1683.

40. Radzicka, A. & Wolfenden, R. (1995). Methods Enzymol. 249, 284–312.

41. Remington, S. J. (1992). Curr. Opin. Struct. Biol. 2, 730–735.

42. Remington, S., Wiegand, G. & Huber, R. (1982). J. Mol. Biol. 158, 111–152.

43. Riddles, P.W., Blakeley, R. L. & Zerner, B. (1979). Anal. Biochem. 94, 75–81.

44. Russell, R. J. M., Hough, D. W., Danson, M. J. & Taylor, G. L. (1994). Structure, 2, 1157–1167.

45. Schramm, V. L. (2013). ACS Chem. Biol. 8, 71–81.

46. Singh, H., Malinski, T. J., Reilly, T. J., Henzl, M. T. & Tanner, J. J. (2011). Arch. Biochem. Biophys. 509, 76–81.

47. Srere, P. A. (1966). J. Biol. Chem. 241, 2157–2165.

48. Srere, P. A. (1969). Methods Enzymol. 13, 3–11.

49. Srere, P. A. (1972). Curr. Top. Cell. Regul. 5, 229–283.

50. Srere, P. A., Brazil, H., Gonen, L. & Takahashi,M. (1963). Acta Chem. Scand. 17, S129–S134.

51. Sudmeier, J. L., Bradshaw, E. M., Haddad, K. E. C., Day, R. M., Thalhauser, C. J., Bullock, P. A. & Bachovchin,W.W. (2003). J. Am. Chem. Soc. 125, 8430–8431.

52. Sutherland, K. J., Danson, M. J., Hough, D. W. & Towner, P. (1991). FEBS Lett. 282, 132–134.

53. Taylor, E. J., Goyal, A., Guerreiro, C. I. P. D., Prates, J. A. M., Money, V. A., Ferry, N., Morland, C., Planas, A., Macdonald, J. A., Stick, R. V., Gilbert, H. J., Fontes, C. M. G. A. & Davies, G. J. (2005). J. Biol. Chem. 280, 32761–32767.

54. Teng, T.-Y. (1990). J. Appl. Cryst. 23, 387–391.

55. Usher, K. C., Remington, S. J., Martin, D. P. & Drueckhammer, D. G. (1994). Biochemistry, 33, 7753–7759.

56. Wallace, A. C., Laskowski, R. A. & Thornton, J. M. (1995). Protein Eng. Des. Sel. 8, 127–134.

57. Weitzman, P. D. J. & Ridley, J. (1983). Biochem. Biophys. Res. Commun. 112, 1021–1026.

58. Wiegand, G. & Remington, S. J. (1986). Annu. Rev. Biophys. Biophys. Chem. 15, 97–117.

59. Wojtkowiak, A., Witek, K., Hennig, J. & Jaskolski, M. (2012). Acta Cryst. D68, 713–723.

60. Yang, W. & Drueckhammer, D.G. (2003). J. Phs. Chem. B, 107, 5986-5994.

CHAPTER 3. FUNCTIONAL DISSECTION OF THE BIPARTITE ACTIVE SITE OF THE CLASS I COENZYME A (COA) TRANSFERASE SUCCINYL-COA: ACETATE COA-TRANSFERASE

3.1 Introduction

Substrate-dependent ordering of flexible active site loops can transmute substrate (ligand) binding affinity into faster enzymatic reactions (Jencks, 1975; Malabanan et al., 2010). When loop motions move critical functional groups, it is unclear if protein motions bias the enzyme-substrate complex conformational ensemble towards a reactive configuration or simply assemble the catalytic machinery. Enzymes with large substrates, like the coenzyme A (CoA) based molecules used throughout metabolism, have ample opportunity to exploit substrate affinity to promote catalysis.

A classic example of this phenomenon is provided by the CoA-transferases, which activate metabolism of diverse carboxylate substrates by introducing the versatile and reactive CoA thioester (Moore and Jencks, 1982a; Amyes and Richard, 1992; Yang and Drueckhammer, 2001), often at the expense of acetyl-CoA (AcCoA). *Acetobacter aceti* strain 1023 and other acetic acid bacteria use succinyl-CoA: acetate CoA-transferase (AarC) in a variant citric acid cycle that is required for a robust acetic acid resistance (*aar*) phenotype (Mullins et al., 2008). Strong selection for key roles in acetic acid resistance and central metabolism appear to have optimized the structural and functional properties

Declaration of collaborative work: Elwood Mullins grew the crystal containing AcMX and Jesse Murphy grew crystals in all other conditions. Elwood Mullins and T. Joseph Kappock collected and analyzed crystallographic data. Elwood Mullins collected and analyzed the borohydride trapping data. All other biochemical experiments and analysis were done by Jesse Murphy. This chapter has been submitted to the journal Frontiers in Chemistry. Publication is pending review.

of AarC, making it an excellent representative of the class I CoA-transferase superfamily. Class I acyl-CoA: carboxylate CoA-transferases produce reactive acylglutamyl anhydride intermediates that acylate CoA, forming either an acyl-CoA product and a free enzyme or a protein glutamyl-CoA thioester and a carboxylate product. Jencks proposed that active site closure, which immobilizes the acyl thioester, potentiates catalysis (White and Jencks, 1976). Efficient catalysis requires an intact CoA, consistent with long-range mechanical coupling of remote "binding" regions to the site of chemistry (Fierke and Jencks, 1986; Whitty et al., 1995).

The Jencks hypothesis was substantiated by a set of AarC crystal structures, including a trapped acetylglutamyl anhydride intermediate in which the CoA sulfur atom lies equidistant from two (external and internal) carbonyl carbon atoms (Mullins and Kappock, 2012). Competing thiolysis reactions (Figure 3.1) produce distinct tetrahedral oxyanion intermediates ~3 Å apart. The external oxyanion is stabilized by hydrogen bonds from CoA and Gly388 amides, whereas the internal oxyanion is stabilized by a hydrogen bond from the Asn347 carboxamide. While components of the external oxyanion hole are strictly conserved throughout the class I CoA-transferase superfamily, residues forming the internal oxyanion hole are supplied by different parts of the protein and are conserved within two large subsets of the superfamily.

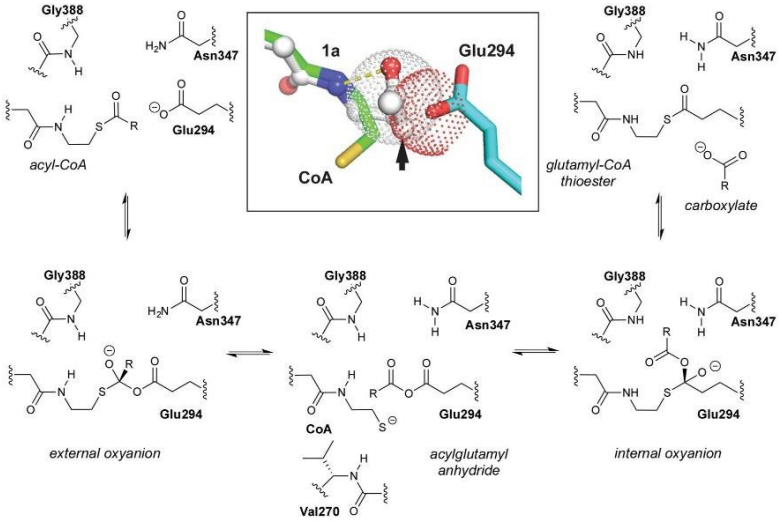

Figure 3.1. Class I CoA-transferase mediated acyl transfers involve two spatially distinct oxyanion holes. The reversible conversion of acyl-CoA substrate to the carboxylate product is shown, a half-reaction that converts free enzyme into a glutamyl-CoA thioester adduct. The other half-reaction reverses this reaction sequence. Inset, overlay of the "open" AarC•CoA complex (PDB entry 4eu7) with the "closed" AarC-E294A•**1a** complex (PDB entry 4euc) indicates that constriction of the active site around an acyl-CoA substrate causes extreme C/O overlap at an approach angle close to the ideal for nucleophilic attack on an unsaturated carbon (the Bürgi-Dunitz angle, 107°). The arrow indicates the position of the sulfur-for-methylene substitution in the AcCoA analogue **1a**, which contains a nonhydrolyzable ketone.

AarC crystal structures revealed that substrate binding provides the last piece of the external oxyanion hole, a hydrogen bond supplied by the CoA N4P hydrogen (Figure 3.1), and have begun to delineate steps in active site closure, a multi-step process that constriction of the acyl-CoA substrate (Mullins and Kappock, 2012). Properly positioning Val270, a residue at the tip of one of two loops that move the most during active site closure, appears to be particularly important: its side chain is proposed to desolvate and constrain the thioester while its amino group is proposed to supply a hydrogen bond donor that stabilizes the CoA thiolate leaving group produced by anhydride formation. The amide-thiolate interaction would both stabilize the nucleophile that attacks the

anhydride and help maintain the 270s loop in a closed state during reactions involving the anhydride adduct. A crystal structure of an inactive mutant, AarC-E294A, bound to the nonhydrolyzable AcCoA analogue dethiaacetyl-CoA (Figure 3.2; **1a**), suggests that active site closure crushes the acyl-CoA thioester into the Glu294 nucleophile, enforcing a near-ideal Bürgi-Dunitz angle (Bürgi et al., 1973) and confining the thioester oxygen atom in the external oxyanion hole (Mullins and Kappock, 2012). In contrast, ligand binding seems to have little effect on the internal oxyanion hole, although the subsequent active site closure process may alter its dielectric environment.

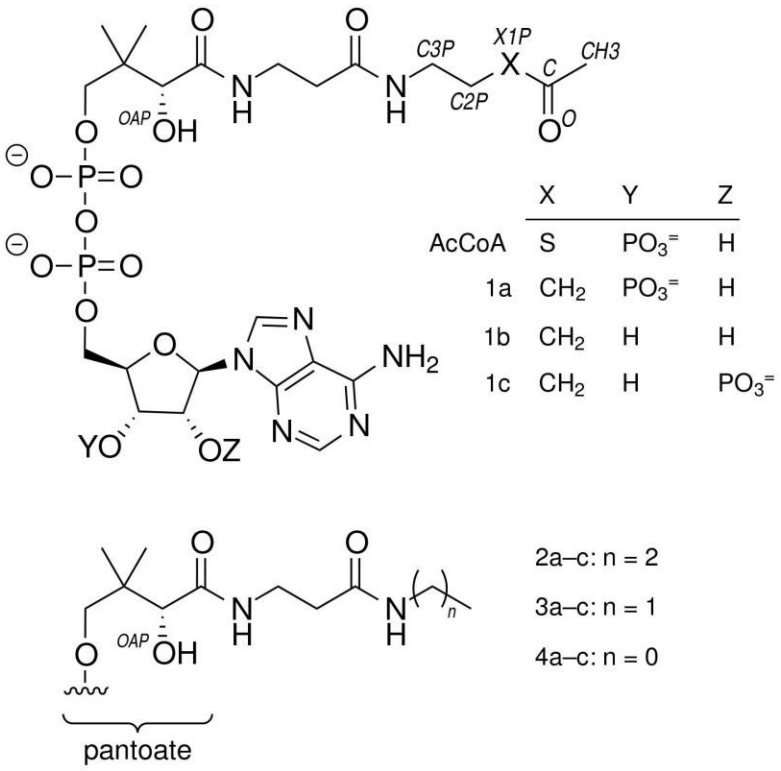

	X	Y	Z
AcCoA	S	$PO_3^=$	H
1a	CH_2	$PO_3^=$	H
1b	CH_2	H	H
1c	CH_2	H	$PO_3^=$

Figure 3.2. Compounds used in this work.

In this study, we used crystal structures of active AarC forms to study enzyme closure and probe the assembly of both oxyanion holes. Mutagenesis of the internal oxyanion hole resulted in diminished but not completely lost enzyme activity (Mullins and Kappock, 2012). Since the external oxyanion hole is composed of backbone and CoA atoms, analogues incapable of undergoing complete enzymatic conversion were used to examine the assembly of a closed enzyme-ligand complex. Compound **1a** was unexpectedly degraded by microbial contamination, yielding a crystal containing an acetylglutamyl anhydride adduct and a CoA analogue (modeled as **2a**). A complex of wild-type AarC and authentic **2a**, which deletes a hydrogen bond between the Glu294 carboxylate and the CoA thiol, showed complete closure of the active site. Since complete closure has not been observed in complexes of wild-type AarC and CoA, a specific polar contact formed between the Glu294 nucleophile and CoA may enable AarC to discriminate between acyl- CoA substrates and CoA. Selective prevention of complete active site closure on CoA might allow CoA-transferases to avoid forming dead-end complexes with ligands that cannot dissipate binding energy through enzyme catalysis.

3.2 Materials and Methods

Reagents and general analytical methods.

Chemicals were purchased from Sigma-Aldrich (St. Louis, MO) or Fisher (Houston, TX) unless otherwise noted. Dimethylformamide (DMF) was dried over 3A molecular sieves under a N_2 atmosphere. Oligodeoxynucleotides (ODNs) were obtained from Integrated DNA Technologies (Coralville, IA) and used without further purification. Yeast

acetyl-CoA synthetase (catalogue number A1765) and a rabbit pyruvate kinase/lactate dehydrogenase mixture (catalogue P0294) were from Sigma. DNA modifying enzymes were from New England Biolabs or Stratagene. Cells were disrupted at 4 °C by three rounds of sonication (1 min on, 1 min cooling) using a Fisher Sonic Dismembrator 550.

The synthesis of **1a** was described previously (Francois et al., 2006); no contaminating **1b** was detected (Figure 3.2). Absorbance measurements were recorded on a Cary Series UV-Vis spectrophotometer (Agilent; Santa Clara, CA) or Nanodrop 2000C (Thermo Scientific; Milwaukee, WI), matrix assisted laser desorption ionization – time of flight mass spectrometry (MALDI-TOF MS) was performed on a 4800 Plus MALDI TOF/TOF (Farmington, MA). Daughter ion *m*/*z* values were computed assuming that adenine N1 can be protonated (Kapinos et al., 2011) or that the phosphates associate with either protons or potassium ions.

DNA manipulations.

Plasmids pJK385, pJK513, and pJK524 encode AarC with a C-terminal hexahistidine tag (AarCH6), AarCH6-E294A, and AarCH6-N347A, respectively (Mullins and Kappock, 2012). For simplicity we will henceforth refer to AarCH6 proteins as AarC; the tagged and untagged proteins produce isostructural orthorhombic crystals (PDB entries 4eu7 and 4eud, respectively). Plasmids pESC124, pESC106, and pET15b/bPanK encode *E. coli* CoaE, CoaD, and PanK proteins, respectively, each with an N-terminal hexahistidine tag (Calder et al., 1999; Strauss and Begley, 2002). Sequencing of pET15b/bPanK revealed a silent mutation (T>C) in the His104 codon that removes an internal, endogenous *Nde*I site. *E.*

coli BL21(DE3) *ackA* was amplified using Pfu TURBO polymerase and oligodeoxynucleotides 2368 (5'-GCTGTCGCATATGTCGAGTAAGT) and 2369 (5'-ATTAGCTCGAGTCAGGCAGTC). The resulting PCR product was cloned into the *Nde*I and *Xho*I sites of pET28a to furnish plasmid pJK667, which is used to express AckA (acetate kinase) with an N-terminal hexahistidine fusion (H6AckA). Double-stranded DNA sequencing of all plasmids by the Purdue Genomics Core Low Throughput Laboratory yielded the anticipated sequence. All plasmids described in this section are available through Addgene (Herskovitch et al., 2012).

Production of CoA analogues 2a and 3a.

CoA biosynthesis enzymes were overexpressed in *E. coli* BL21(DE3) cells transformed with pESC124, pESC106, or pET15b/bPanK and propagated on LB medium supplemented with 100 mg/L ampicillin or 70 mg/L kanamycin. Production cultures were grown with shaking at 220 rpm at 37 °C to an optical density at 600 nm of 0.6, at which point isopropyl β-D-1-thiogalactopyranoside was added (0.4 mM final concentration). After an additional 4 h at 37 °C, cells were harvested by slow centrifugation (5000g, 15 min) and stored at -80 °C.

H6AckA was produced in *E. coli* BL21(DE3) cells transformed with pJK667 and propagated on LB medium supplemented with 100 mg/L ampicillin. Production cultures of ZYM-5052 autoinduction medium (1 L) (Studier, 2005) were grown with shaking at 220 rpm at 37 °C for 18 h. Cells were harvested by slow centrifugation and stored at -80 °C. The following protocol was used to isolate H6AckA, H6PanK, H6CoaD, or H6CoaE; all steps

were performed at 4 °C. Cells were resuspended in 5 mL/g TM buffer (50 mM Tris-HCl pH 8.0) at 4 °C and disrupted by sonication (3 rounds of 1 min on and 1 min off, 20% intensity). Debris was removed by fast centrifugation (30,000g, 30 min). The supernatant was adjusted to 1% (w/v) streptomycin sulfate [10% (w/v) stock] and solids were removed by fast centrifugation. The supernatant was applied under gravity flow to a Ni^{2+}-iminodiacetic acid Sepharose column (2.5 cm x 8 cm, ~5 mL) in TM buffer. After washing with TM buffer containing 300 mM KCl and 40 mM imidazole (50 mL), bound proteins were displaced using TM buffer containing 300 mM KCl and 500 mM imidazole (20 mL). SDS-PAGE was used to identify fractions containing the relevant proteins. Fractions were pooled, dialyzed 18 h against 50 mM Tris-HCl, pH 8.0, 100 mM KCl (1 L x 2 changes), and either adjusted to 50% (v/v) glycerol and stored at -20 °C or flash-frozen (H6AckA) in liquid N_2 and stored at -80 °C. Specific activities were determined for H6AckA (Ferry, 2011) and H6PanK (Francois et al., 2006).

N-propylpantothenamide and *N*-ethylpantothenamide were synthesized as described previously (Strauss and Begley, 2002). Sodium pantothenate (2.0 g, 8.3 mmol) was converted to the free acid using a Dowex 50W (H^+ form) column (1.7 cm x 10 cm). Pantothenic acid (1.7 g, 7.8 mmol) was dissolved in 10 mL dry DMF and either propylamine or ethylamine (0.82 mL, 10 mmol) was added dropwise with continuous stirring under a N_2 atmosphere at 22 °C. Diphenylphosphoryl azide (2.2 mL, 10 mmol) was then added dropwise and the reaction mixture was placed in an ice bath. After 10 min, triethylamine (1.39 mL, 10 mmol) was added dropwise and the reaction mixture was

stirred at 0 °C for 2 h, then 22 °C for 15 h. A portion (0.3 mL) of the reaction mixture above was mixed with deionized water (1.2 mL), solids were removed by centrifugation (16000g, 10 min), and solvent was removed under reduced pressure at 60 °C. The resulting clear, viscous oil was dissolved to give a ~0.1 M aqueous solution. A final volume of 5 mL contained 50 mM Tris-HCl, pH 8.0, 5 mM $MgCl_2$, 5 mM ATP, 300 µg H6PanK (2.7 units), 300 µg H6CoaD, 1500 µg H6CoaE, and either 10 mM *N*-propylpantothenamide or *N*-ethylpantothenamide. After 4 h at 37 °C, 0.5 mL formic acid (98%) was added and solids were removed by centrifugation (16000g, 10 min). The quenched reaction mixture was injected (5 mL) onto an Agilent 110 series HPLC equipped with a Luna 5 µm C18(2) 250x21.2 mm column equilibrated in 0.1% (v/v) trifluoroacetic acid (TFA), 2.0% methanol. The column was developed in a gradient of 2% to 90% methanol in 0.1% TFA and large peaks were collected, frozen, and lyophilized to dryness. The resulting solid, containing **2a** or **3a** (Figure 3.2), was resuspended in 5 mM HCl and concentrations were determined by the absorbance at 260 nm assuming a molar extinction coefficient of 16.4 $mM^{-1}cm^{-1}$. The molecular mass and purity of 3'-phosphoadenosine 5'-(*O*-(*N*-propyl-*R*-pantothenamide))pyrophosphate (**2a**) and 3'-phosphoadenosine 5'-(*O*-(*N*-ethyl-*R*-pantothenamide))pyrophosphate (**3a**) were assessed using LCMS (Agilent 1100 HPLC G1946B).

AarC production and characterization.

AarC and AarC mutants were expressed in C41(DE3) pREP4-*groESL*, purified, and characterized by VisR and LCR activity assays as described previously (Mullins et al., 2008; Mullins and Kappock, 2012). Sodium borohydride inactivation experiments were performed as described previously (Mullins et al., 2008). Activities for AarC and other enzymes are expressed in units, defined as 1 µmol product formed per min.

Crystal growth and X-ray data collection.

Crystals were grown at 22 ºC using the hanging-drop vapor-diffusion method by modifying a published method (Mullins and Kappock, 2012). Reservoir solutions (0.5 mL) contained 0.9 M sodium citrate, 0.1 M imidazole•HCl, pH 8.2, and 25 mM 2-mercaptoethanol. Drops contained 2 µL of reservoir solution mixed with 2 µL of protein solution (6.0 mg/mL AarC, 45 mM Tris•HCl, pH 8.0, 90 mM potassium chloride, either 10 mM CoA, 10 mM **1a**, or 1–3 mM **2a**). Some drops contained 1–50 mM sodium acetate, pH 8.2, instead of (or in addition to) a CoA analogue. Three d before cryoprotection, sodium acetate (~50 mM final, added from a 1 M stock at pH 8.2) was gently added to several drops containing crystals grown in the presence of **2a**. Crystals were soaked for 13 h in a cryoprotectant solution containing 15% (w/v) sorbitol, 1.1 M sodium citrate, 0.1 M imidazole, pH 8.2, 25 mM 2-mercaptoethanol, and any additional ligands (each at 110% of the concentration used for crystallization). No special measures were undertaken to exclude microbial contaminants. Crystals were loaded into Nylon loops, flash-cooled by rapid immersion in liquid N_2, and kept at or below 100 K (Teng, 1990). X-ray diffraction

data were collected at LS-CAT beamlines at the Advanced Photon Source at Argonne National Laboratory. Diffraction data were indexed, integrated, and scaled using HKL2000 (Otwinowski and Minor, 1997).

Determination, refinement, and analysis of crystal structures.

Automatic and manual refinement were performed using PHENIX (Adams et al., 2010) and Coot (Emsley et al., 2010), respectively. Ligand coordinates and restraints were obtained from HIC-Up (Kleywegt, 2007) and modified using PHENIX.

All structures were solved using a hybrid model of translation-libration-screw (TLS) groups and isotropic atomic B-factor (B_{iso}) terms for all protein atoms. PHENIX analysis of the 4eu9 coordinates was used to define a set of twelve TLS groups. The starting model for direct refinement was protein atoms from AarC-R228E•CoA (PDB entry 4eu9) coordinates, with initial B_{iso} values set to 30 $Å^2$ and minor alternative conformations set to zero occupancy. Initial TLS refinement (15 cycles) (Merritt, 2012) was followed by positional (Cartesian, real-space, and rigid-body) and ADP refinement (5 cycles). CoA or an analogue was then added (except PDB entry 5dw4) and superfluous alternate conformations were deleted using COOT. Subsequent refinement rounds omitted rigid-body refinement, added occupancy refinement, and were alternated with manual model adjustments in COOT. Ligands, known buffer components, and hypothetical **1a** degradation products (smaller CoA analogues and, in one structure, a formate molecule) were built into continuous difference electron density. Cys15 in some structures showed evidence of sulfur oxidation and was modeled as cysteine sulfenic acid (CSX form; Furdui

and Poole, 2014). Riding hydrogens used during positional refinement steps were deleted before a final round of ADP refinement (10 cycles).

Structures were checked using MOLPROBITY (Chen et al., 2010) and the worldwide Protein Data Bank (Berman et al., 2003) validation pipeline (Read et al., 2011). Cavities and pores were identified using MOLEonline 2.0 (Sehnal et al., 2013). Several figures were prepared using Pymol (DeLano, 2002).

Stability of 1a and 2a.

A final volume of either 0.5 or 1.0 mL contained 50 mM potassium phosphate, pH 8.0, 100 mM KCl, 100 µM **1a**, and 10 µM (subunit concentration) of either AarC (21.5 units, 0.28 mg or 43 units, 0.56 mg) or AarC-E294A (≤ 0.0043 units, 0.56 mg) was incubated at 22 °C in a polypropylene microcentrifuge tube. One complete AarC reaction mixture was sterile-filtered (surfactant-free cellulose acetate syringe filter with 0.22 µm pores; Nalgene, Rochester, NY) to remove microbes and placed in a sterile, silanized microcentrifuge tube (MidSci; St Louis, MO). A no-enzyme control and reaction mixtures containing 10 µM **2a** instead of **1a** were processed in parallel. Aliquots (0.1 mL) were withdrawn periodically, placed in a microcentrifuge tube, and heated in a sand bath (95°C, 15 min). Solids were removed by centrifugation (16,000 g, 10 min), an ultraviolet spectrum was recorded, and the clarified reaction mixture was stored at -20 °C. **2a** derivatives were quantitated using a Waters (Milford, MA) Breeze HPLC system equipped with an Agilent (Santa Clara, CA) Zorbax Eclipse XBD-C18 column (4.6 x 150 mm, 5 µm) and a Waters 717 autosampler. A portion of each quenched reaction mixture (20 µL) was mixed with an equal volume of 10% trichloroacetic acid (TCA) and applied to the column,

which was developed isocratically [200 mM sodium phosphate, 150 mM sodium acetate, pH 4.6, adjusted to 2% (v/v) acetonitrile] at 26 °C at a flow rate of 1 mL/min with detection at 260 nm. CoA analogues were identified by comparison to standard mixtures (run daily to correct for variable retention patterns) and their concentrations were determined by reference to the analogue peak area in an immediately quenched (t=0) complete reaction mixture.

Additional small aliquots (2.7 µL) were periodically removed from reaction mixtures, either containing or lacking **1a**, and diluted to a final volume of 0.15 mL in phosphate/KCl buffer with or without 10 mM sodium borohydride. After 10 min at 25 °C, aliquots (5 µL) were removed and residual SCACT activity was measured in LCR assays (Mullins et al., 2008).

Identification of acetate.

A 1 M, pH 8.0 acetate standard was prepared from solid sodium acetate. A final volume of 20 µL contained 50 mM potassium phosphate pH 8.0, 100 mM KCl, 25 mM $MgCl_2$, 16 µL of either the quenched **1a** degradation mixture or an acetate standard, 1.0 mM CoA, 1.8 mM ATP, and acetyl-CoA synthetase (0.004 units) at 22 °C. After 45 min, TCA [20 µL, 10% (w/v)] was added and solids were removed by centrifugation (16000g, 10 min). Waters HPLC analysis (25 µL injections) revealed a single large peak, not present in a control reaction mixture lacking acetyl-CoA synthetase that co-migrated with an authentic AcCoA standard. AcCoA concentrations, determined by reference to AcCoA standard injections, were taken to be the lower limit for acetate production in **1a** stability.

Quantitation of acetate.

A final volume of 70 µL in a microcentrifuge tube contained 50 mM potassium phosphate pH 8.0, 100 mM KCl, 6.7 mM $MgCl_2$, 10 µL of either a quenched **1a** stability assay reaction mixture or an acetate standard, 0.14 mM NADH, 1 mM ATP, 2 mM phosphoenolpyruvate (PEP), H6AckA (3 units), pyruvate kinase (6 units), and lactate dehydrogenase (6 units) at 22 °C. Reactions were initiated by the addition of H6AckA. After 40 min, the entire reaction mixture was transferred to a black-walled microvolume quartz cuvette (70 µL capacity) and a spectrum was recorded. Acetate concentrations were determined by subtracting the absorbance at 340 nm (A340) of a control reaction lacking H6AckA ($\Delta\varepsilon_{340}$ = 6.22 mM^{-1} cm^{-1}).

MALDI-TOF analysis of 1a degradation products.

Quenched **1a** stability assay reaction mixtures were thawed and an aliquot (1 µL) was mixed with 9 µL 1% (v/v) formic acid. A portion of the acidified mixture (0.5 µL) was mixed with 0.5 µL matrix solution (1 mg/mL α-cyano-4-hydroxycinnamic acid in 50% acetonitrile and 0.1% TFA), deposited on a stainless steel MALDI plate, and air-dried for ~2 h. Analysis was performed in positive ion mode. Batch method cation exchange (PSE cation exchange resin) and solid phase extraction using ZipTip pipette tips (Millipore) was also attempted on **1a** stability assay time points.

3.3 Results

Parameterized active site conformations.

We have defined four stages in the closing of the AarC active site, ranging from fully open (exemplified by AarC, PDB entry 4eu3) to fully closed (exemplified by AarC-E294A•CoA, PDB entry 4eub) that engage, immobilize, and desolvate acyl-CoA substrates and Glu294 adducts (Mullins and Kappock, 2012). Characteristic side chain conformations for residues Arg228, Asn229, Phe232, and Val270 were associated with each stage to catalogue the underlying complex dynamics and multiple roles of the 230s loop (residues 228-234) and the 270s loop (residues 270-274). Using external oxyanion hole component Gly388 N as a fixed reference point, active site closure can be quantitatively described using four interatomic distances that capture 230s loop motion (the sum of distances to Asn229 CG and Phe232 CG), active site constriction (the distance to Val270 CB), and the in/out conformations of Arg228 (the distance to Arg228 CG), which occur twice per half-reaction and are typically reciprocal to the movements of Asn229. This parametrization groups closed conformations (cluster at lower left in Figure 3.3) and open conformations (upper right in Figure 3.3) and allows ready identification of intermediate states such as those associated with covalent enzyme adducts (e.g., the acetylglutamyl anhydride 4eu6A and and the glutamyl-CoA thioester 4eu6B).

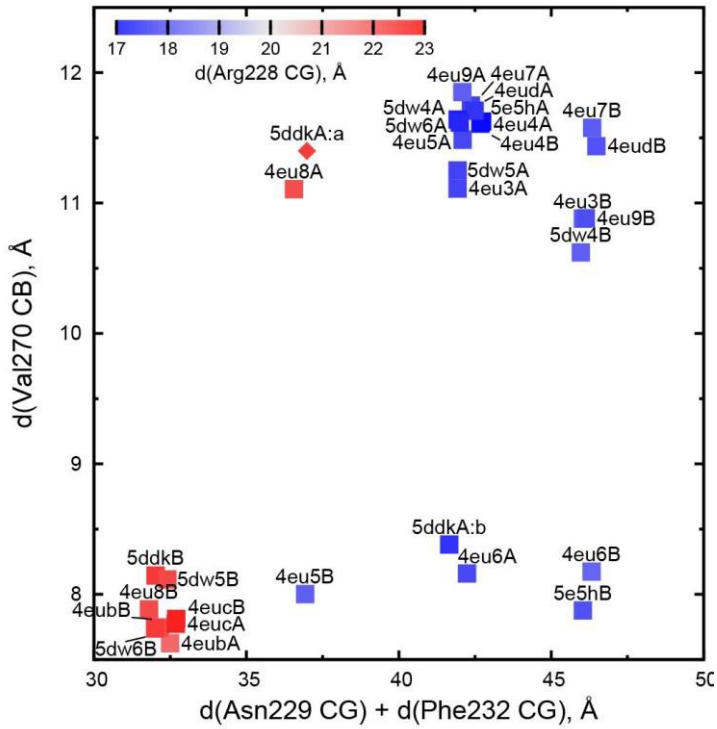

Figure 3.3. Parametrization of AarC(H6) active site conformations. Each point represents one subunit of AarC (PDB entry 4eud) or AarCH6 and its mutant forms (remaining points). The values are derived from distances (d) between Gly388 N, a fixed reference point within the active site, and the indicated atom(s) in a wild-type or mutant subunit. All proteins crystallized in an orthorhombic lattice apart from 4eu4, which is in a hexagonal lattice (Mullins and Kappock, 2012). Note that the two hexagonal subunits adopt almost identical open conformations. The open conformations of subunit B in orthorhombic crystals form a sub-cluster (upper right) due to crystal contacts described in the text. One Val270 CB position was estimated for one minor conformer (5ddkA:a, diamond symbol) using real-space refinement.

Different sub-clusters for subunit A and B open conformations (Figure 3.3) arise from crystal-packing interactions in the orthorhombic lattice adopted in the majority of AarC(H6) crystals. The loop containing Phe232B contacts helix alpha-4 in subunit A from a neighboring asymmetric unit, which leads to a slightly larger separation of this region from a reference point in each active site (the intra-subunit Phe232 CG-Gly388 N distance is 21.7 ± 0.1 Å [n = 9] in subunit A and 24.9 ± 0.1 Å [n = 5] in subunit B). An open-

conformation structure solved in a hexagonal lattice (PDB entry 4eu4) has no comparable crystal-packing contacts and resembles orthorhombic subunit A (the Phe232 CG-Gly388 N distance is 21.9 Å for both subunits). The other three residues considered appear to be unaffected by subunit-specific differences in crystal packing.

A misaligned nucleophile in AarC-N347A.

AarC-N347A lacks the carboxamide moiety proposed to contact the internal oxyanion formed during thiolysis of the acylglutamyl anhydride intermediate (Figure 3.1). The mutant retains appreciable (~15% of wild-type) specific activity (Mullins and Kappock, 2012). A data set obtained from a crystal grown in the presence of CoA was used to determine a structure in an orthorhombic space group. Like all structures described here, the protein fold and CoA binding site were the same as described previously (Mullins and Kappock, 2012). Chloride ions were bound, as expected, near the pseudo-twofold axis or between C-terminal domains of each subunit. Three imidazole ligands were also included at the latter interface.

The final refined model (PDB entry 5ddk) contained alternate conformations for both CoA ethanethiol moieties and residues Arg228A-Asp236A, with the major and minor contributions from closed and open conformations, respectively. The subunit A 230s loop conformations differ by tandem flips of the two peptide bonds to Asn229. The subunit A 270s loop adopted multiple conformations, with the closed conformation most abundant. Difference electron density peaks consistent with the 270s loop open conformation were observed but too weak to justify inclusion in the final model. All three regions in subunit

B adopted the closed conformation. The differences in CoA complex structures for wild-type and mutant AarC (open and closed, respectively; subunit B) do not affect this region of the active site (Figure 3.4).

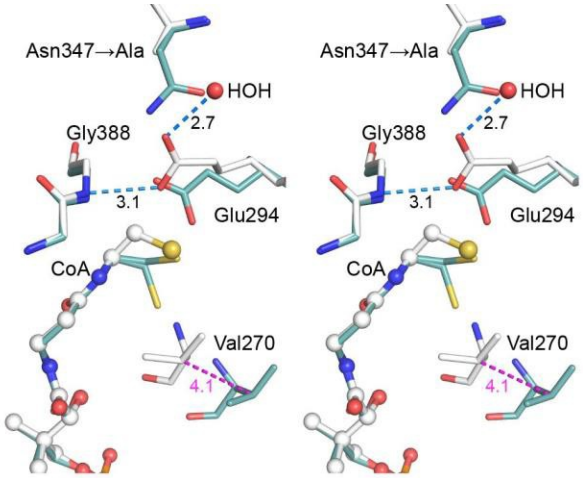

Figure 3.4. Stereogram of the AarC-N347A active site. The B subunits of AarC-N347A (PDB entry 5ddk, white carbon atoms) and AarC (PDB entry 4eu7, blue carbon atoms), each bound to CoA, are superposed. Spheres are shown for ligand atoms in AarC-N347A. The Glu294 carboxylate shifts by about the width of the carboxylate moiety, allowing a different oxygen atom to interact with Gly388 N (separated by 0.33 Å here). The Glu294 rotamer changes from *mt-10* (open) to *tt-0* (closed), as illustrated here, but the closed χ_3 value is unusual. Distances (Å) in blue show hydrogen bonds involving the Glu294 nucleophile, including one to the "new" HOH in the AarC-N347A•CoA complex. The distance colored magenta depicts the motion of the Val270 CB between open (AarC) and closed (AarC-N347A) conformations.

Since AarC-N347A retains significant activity, our hypothesis was that a polar group would simply supplant the missing Asn347 carboxamide and restore its function. As anticipated, an active site solvent molecule was observed at this location in each subunit, with a lower *B*-factor in subunit B (HOH 775A and 787B: 58 and 34 $Å^2$). The solvent substitution, however, additionally appears to influence the conformation of Glu294. While Glu294 in the N347A mutant adopts the tt-0 rotamer observed in other

closed structures, its χ_3 value is unusual, corresponding to a rotation of the attacking oxygen towards the mutated residue (i.e., away from the CoA binding site). [Any value of χ_3 is permitted in the Glu tt-0 rotamer (Lovell et al., 2000).] The resulting misalignment of the key nucleophile would decrease the probability of productive attack on an incoming acyl-CoA substrate.

Since AarC-N347A appears to favor the closed conformation and potentially substrate exchange, the deleterious effect of the mutant might also be a consequence of impeded acyl-CoA dissociation and binding during steady-state turnover. We disfavor this alternative hypothesis since all four N347A K_M values are similar to wild-type AarC K_M values (Mullins and Kappock, 2012). Our working model therefore remains that Asn347 polarizes and positions Glu294, aiding in its roles as nucleophile and, potentially, as the leaving group in the CoA thiolysis reaction. The principal impact of the N347A mutation would therefore appear to be on enzyme-mediated, unimolecular chemical steps.

Conversion of 1a during crystallization with AarC.

The AcCoA ketone analogue **1a**, in which the thioester sulfur atom is replaced by a methylene group, was tested for its ability to form a hemiacetal analogue of the tetrahedral hemithioacetal intermediate stabilized by the external oxyanion hole (Figure 3.5). Cleavage of a **1a**-derived hemiacetal is prevented because an alkyl carbanion cannot serve as a leaving group, affording a chance to study a stabilized external oxyanion. AarC-E294A readily formed crystals containing **1a** in a closed active site (PDB entry 4euc). Structure comparisons led us to predict that a severe steric clash with the Glu294

carboxylate (Figure 3.1, insert) would favor anhydride formation but might preclude formation of a closed AarC•**1a** complex (Mullins and Kappock, 2012).

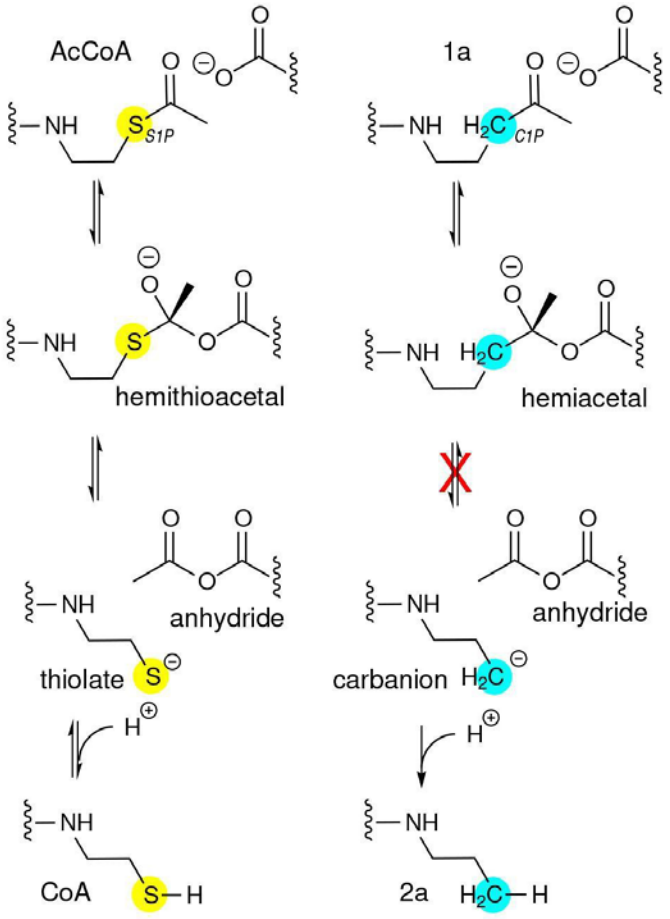

Figure 3.5. CoA analogues as probes of CoA-transferase mechanism. Left, reactions involving the external carbonyl of the acetylglutamyl anhydride. Thiolate protonation is possible but unlikely to be part of the normal reaction coordinate. Right, attempted trapping of a tetrahedral external oxyanion intermediate. The atomic substitution in **1a** has comparatively small effects on electronegativity and sterics so could allow formation of a hemiacetal intermediate resembling the external oxyanion and perhaps enable insight into how its reactivity is modulated. The tetrahedral intermediate formed by nucleophilic attack by AarC on the **1a** carbonyl cannot be resolved into cleavage products. The very high pK_a of an unactivated alkyl methyl, perhaps 50, would preclude formation of the alkyl carbanion required, even considering the exothermic subsequent protonation.

AarC was crystallized in the presence of **1a** and its structure was determined (Table 2; PDB entry 5e5h). Glu294A was modeled as a mixture of free carboxylate and acetylglutamyl anhydride adduct in a 0.4/0.6 ratio, with a relatively narrow range of *B*-factors. Since density associated with the 3'-phosphate was ambiguous and weak, the large ligand in subunit A was modeled as **2b** (Figure 3.2). Excess density was noted near the 2'-hydroxyl that might be due to a minor contribution from a 2'-phospho isomer, **2c**. [Iso-CoA forms during the chemical synthesis of CoA (Burns et al., 2005).] The electron density associated with the large ligand in subunit B did not extend beyond carbon atom C3P, so it was modeled as 3'-phosphoadenosine 5'-(*O*-(*N*-methyl-*R*-pantothenamide))pyrophosphate (Figure 3.2; **4a**). Unlike subunit A, convincing electron density was associated with the 3'-phosphate group in subunit B, stabilized by the side chain of Lys408B. An active site acetate ligand was also included in subunit B.

Subunit A (5e5hA) adopted an open conformation distinctly different from a partially closed conformation observed for an AcCoA-derived acetylglutamyl anhydride (PDB entry 4eu6A) (Figure 3.3). The former appears to be less able to shield a labile acetylglutamyl anhydride from hydrolysis. Subunit B (5e5hB) adopted a partially closed conformation similar to that observed for the glutamyl-CoA thioester adduct bound to acetate (PDB entry 4eu6B) (Figure 3.3), even though **1a** and truncated derivatives (e.g., **2a** and **4a**) cannot form thioesters. An acetate contacting Ser71B OG was included in the model.

Acetate observed previously in an AcCoA-soaked AarC crystal, in an active site containing a glutamyl-CoA thioester (PDB entry 4eu6B), was presumed to arise from

AcCoA hydrolysis (Mullins and Kappock, 2012). No chemical process of which we are aware could convert the ketone in **1a** to **2a** and acetate, let alone an acetylated molecule capable of producing an anhydride. The apparent formation of an anhydride seems to imply that AarC converts the **1a** ketone into a two-carbon activated acetyl group, with the remaining atoms forming **2a** or a related compound. No CoA-transferase has been reported to perform oxidation activity, suggesting that the conversion of **1a** to an AarC acylating agent may be due to an unknown contaminating enzyme or microbe. Subsequent hydrolysis (n.b., not the normal thiolysis) of the anhydride would account for the formation of acetate in subunit B. Positive evidence for these transformations cannot be gleaned from electron density maps alone. We therefore attempted to obtain chemical evidence for the formation of **1a** -derived compounds. Partial disorder of the **1a** ketone did not appear to account for smaller ligand **2b**. The "acetyl" moiety of **1a** would clash with Glu294, even in the relatively open subunit A. The closed active site of subunit B would enforce even more stringent steric constraints on the bound ligand, which might be a partially disordered **2a** or **3a** instead of the modelled **4a**.

Attempted trapping of acetylglutamyl anhydride with sodium borohydride.

Borohydride can inactivate class I CoA-transferases supplied a valid substrate, by reducing an activated Glu carboxylate thioester to 5-hydroxynorvaline (Solomon and Jencks, 1969). While both the acylglutamyl anhydride (internal carbonyl) and glutamyl-CoA thioester adducts could be inactivated, **1a** cannot form the latter. To test for anhydride formation, AarC and 1a were incubated together for a week. Aliquots of the

reaction mixture were withdrawn at intervals, mixed with sodium borohydride, and tested for residual SCACT activity. No loss of enzyme activity was observed in this experiment or in a control reaction lacking **1a** (Figure 3.6). This finding suggests that no anhydride adduct of AarC is present in solution, although the 5e5h structure suggests that one may be stabilized by the crystalline lattice.

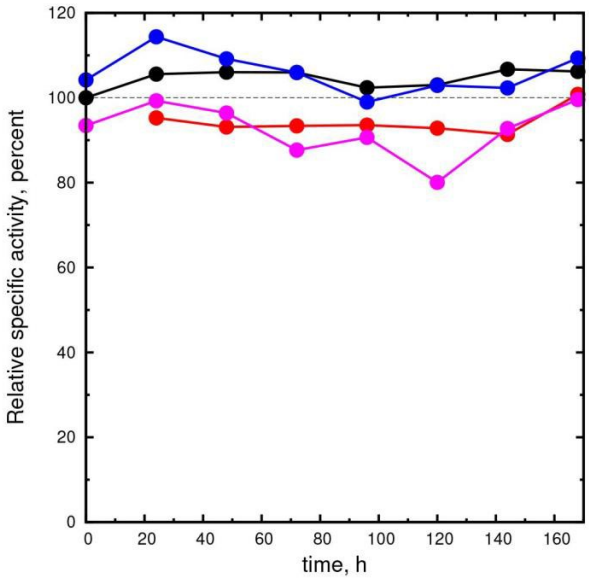

Figure 3.6. Attempted borohydride trapping of covalent adducts of AarCH6. Treatment with reductant is expected to inactivate AarCH6 by irreversible reduction of either the Glu294 acetylglutamyl anhydride or glutamyl-CoA thioester adducts. The latter has been directly detected in a AarC mutant, presumably as a consequence of protein production in E. coli (Mullins et al., 2008). Aliquots were withdrawn at the indicated times from either 1a stability assays or no- 1a controls and transferred to either 10 mM NaBH4 or a water control. Specific activities are given relative to the zero-time point of a no- 1a control that was not exposed to NaBH4 (black symbols; 100% = 112 units/mg). Other experiments showed no time-dependent loss of SCACT activity: no 1a, 10 mM NaBH4 (red symbols; missing t=0 point); 100 µM 1a, no NaBH4 (blue symbols), 100 µM 1a, 10 mM NaBH4 (purple symbols).

Stability of 1a.

Direct detection of **1a** cleavage by analysis of small molecules formed in AarC crystal mother liquor was deemed to be infeasible. Instead, an **1a** stability assay was devised to detect the formation of truncated CoA analogues in reaction mixtures containing AarC. Analogues **2a** and **3a** were synthesized for use as authentic standards (Figure 3.7). HPLC chromatographic conditions that resolved **1a**, **1c**, and **2a** were identified (Figure 3.8). Under these conditions, the detection threshold for **2a** (in the presence of a ~20-fold molar excess of **1a**) was ~0.02 nmol.

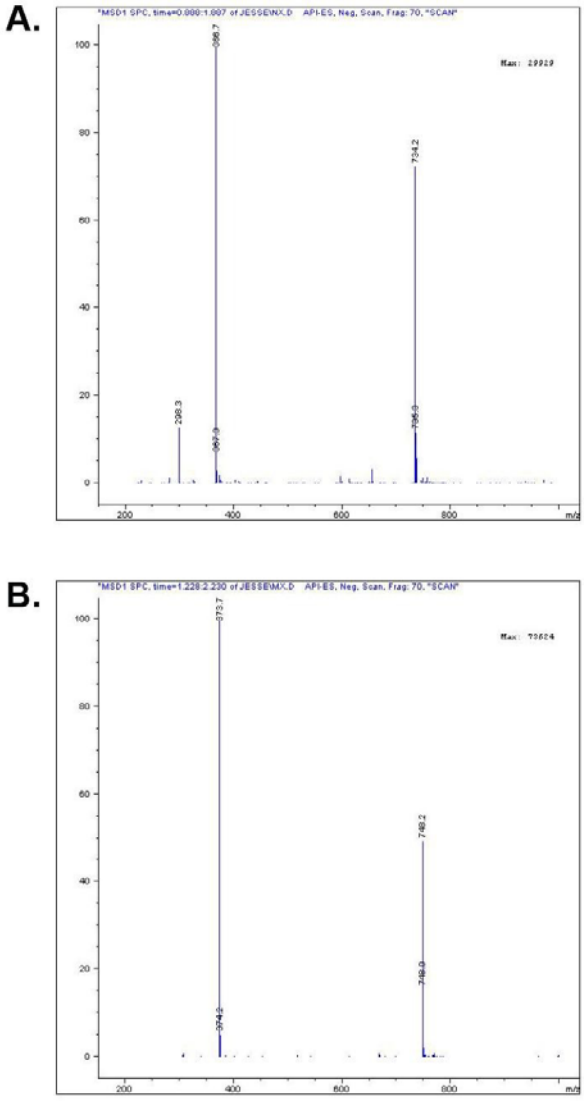

Figure 3.7. LCMS analysis (negative ion mode) of CoA analogues 2a and 3a. (A) 2a showed peaks at m/z 748 and 373.5, corresponding to singly and doubly deprotonated forms (expected parent molecule mass 749.16 Da), presumably one or more of the phosphate moieties. (B) 3a showed peaks at m/z 734 and 366.5, corresponding to singly and doubly deprotonated forms (expected parent molecule mass 735.14 Da).

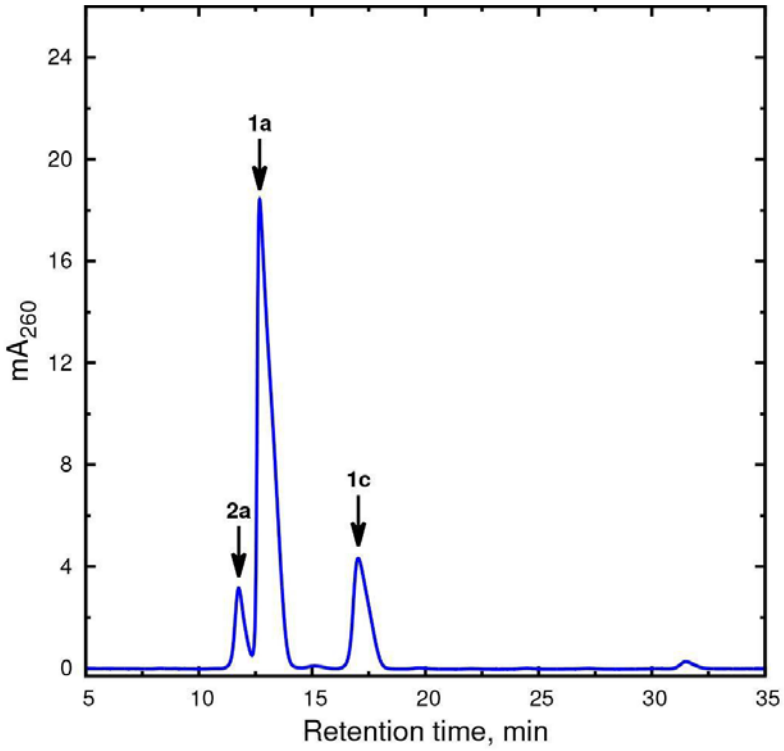

Figure 3.8. HPLC analysis of synthetic 1a and 2a. A 9:1 mixture of 1a and 2a was injected at t=0 and the absorbance profile at 260 nm was recorded (mA = milli AU). Conditions were otherwise identical to those used to quantitate analogues in the 1a stability assay (Figure 3.10). Peaks observed under these conditions were assigned using single-compound injections: 1a, 15.4 min; 2a, 17.0 min; and 1c, 19.3 min.

The stability of **1a** was assessed by serial HPLC analysis of reaction mixtures incubated at ambient temperature. CoA analogues including **1a** were identified by retention time and **1a** was quantitated by comparing its peak area to a reference reaction mixture quenched immediately after the addition of enzyme.

First, **1a** was incubated in buffer without added enzyme. Under these conditions, **1a** was stable and no new peaks were observed in HPLC chromatograms, with 94–100% remaining after 168 h (Figure 3.9).

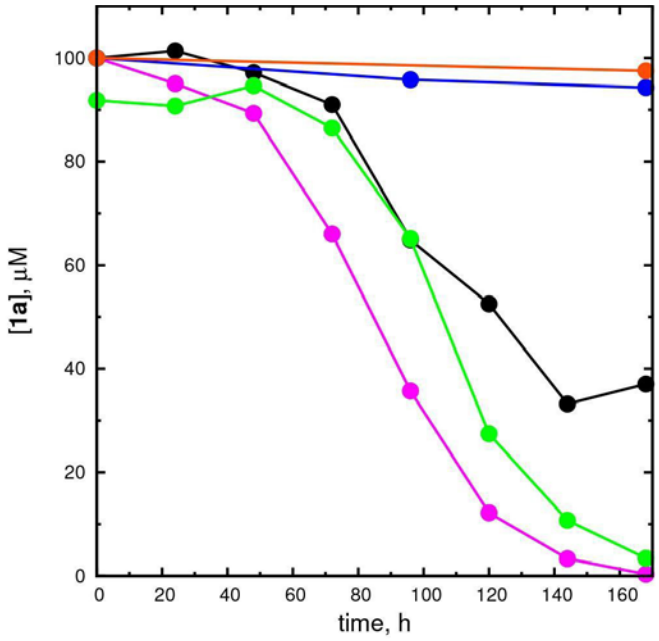

Figure 3.9. Active enzyme is not required for 1a degradation. Absorbance spectra or HPLC analysis after heat quenching was used to monitor the decay of 1a (initially 100 µM) in reaction mixtures containing: 10 µM AarCH6, magenta (HPLC) and green (A260) symbols; 10 µM AarCH6-E294A, black symbols; no enzyme, blue symbols; and 10 µM AarCH6 that was sterile-filtered immediately after mixing, red symbols.

Second, **1a** and AarC were incubated together at a 10:1 molar ratio (subunit concentration). Delayed but complete loss of the HPLC peak corresponding to **1a** was observed (Figure 3.10). A parallel experiment monitoring the absorbance spectrum of crude reaction mixtures showed a progressive decrease at 260 nm (Figure 3.9), consistent with disintegration of the adenine moiety.

Third, **1a** and the inactive mutant AarC-E294A were incubated together at a 10:1 molar ratio. Delayed but incomplete loss of the HPLC peak corresponding to **1a** was observed (Figure 3.9), with ~37% remaining after 168 h. Therefore active enzyme was not required for **1a** degradation.

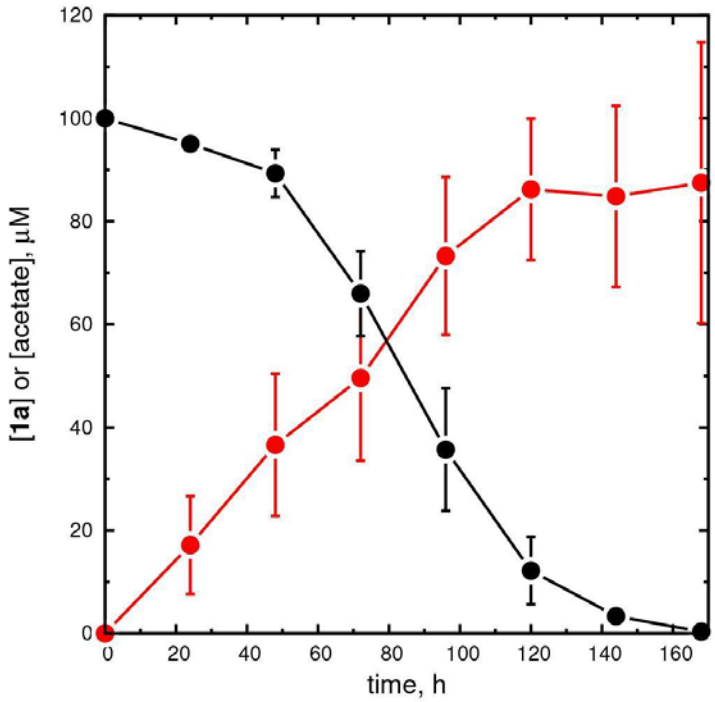

Figure 3.10. Unfiltered reaction mixtures containing AarCH6 decompose 1a. Stability of 1a in a reaction mixture initially containing 10 µM AarCH6 and 100 µM **1a** at room temperature. Aliquots were withdrawn at the indicated time points and HPLC (**1a**, black filled circles), AK-ATPase assay (acetate, red filled circles), and MALDI-MS analyses were performed. The circles and error bars respectively depict average concentrations and standard deviations for three independent time courses. An alternative time course using ACS to detect acetate is shown in Figure 3.18.

Fourth, a reaction mixture containing **1a** and AarC, using the same conditions as the second experiment, was sterile-filtered shortly after mixing. After 168 h, 98% of the original **1a** was recovered, demonstrating that it is stable under these conditions. Furthermore, this result suggested that **1a** truncation is a microbe-mediated process. A new peak observed in HPLC traces coincided with rapid loss of **1a** (Figure 3.11). This late-eluting peak was collected, analyzed by MALDI-TOF MS, and found to have m/z = 712.13, corresponding to an $[M+H-P_i]^+$ ion (expected m/z 712.20) (data not shown). This

compound was tentatively assigned as 3'-dephospho-AcMX (**1b**), and it appeared to be preferentially formed from **1a** not **1c** (Figure 3.11). Peaks corresponding to **2a**, **3a**, or a peak likely to correspond to **4a** were not detected by HPLC analysis of **1a** stability assay reaction mixtures.

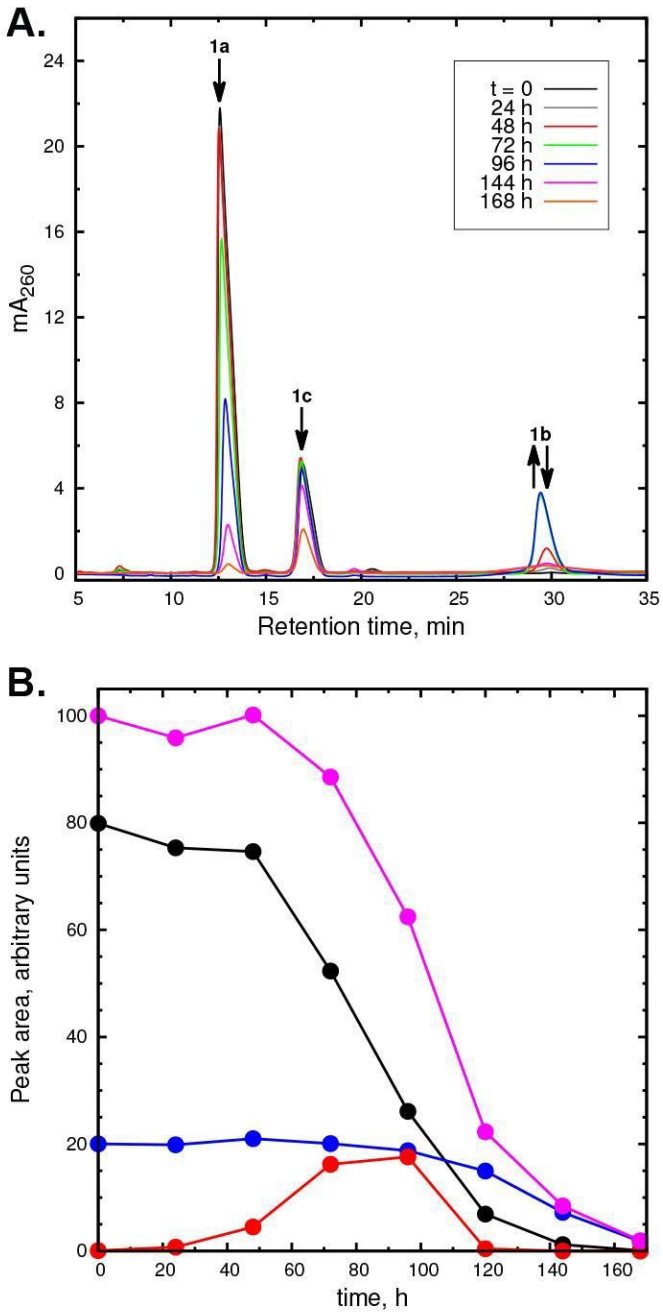

Figure 3.11. Transient formation of 1b. (A) Sequence of HPLC chromatograms for a representative 1a degradation time course. The peak at 29.4 min was found to contain a species consistent with 1b, with m/z = 712.17 (Figure 3.13); m/z = 712.21 expected ($C_{24}H_{40}N_7O_{14}P_2^+$). 2a was not detected in this or other HPLC experiments. (B) Peak areas for the chromatograms shown in panel A (total t=0 peak area set arbitrarily to 100): 1a, black symbols; 1b, red symbols; 1c, blue symbols; total peak area, magenta. 1b appears to be formed primarily from 1a not 1c.

Stability of 2a.

One potential explanation for the failure to detect **1a** -derived **2a** in solution stability assays would be rapid degradation of **2a**. Conversely, **2a** present in a crystal might be protected from degradation. The solution stability of **2a** was assessed as described for **1a**. In unfiltered reaction mixtures containing AarC, **2a** decomposed completely, with an initial lag ~24 h longer than that observed for **1a** (Figure 3.12). The substitution of inactive AarC-E294A did not prevent degradation, but **2a** was stable in a no-enzyme control.

A microbe-mediated **2a** degradation process was again suggested by the correlated loss of the **2a** HPLC peak and the adenine chromophore (data not shown). We concluded that rapid **2a** decomposition could explain why it was not detected by HPLC, since only a small amount of **2a** may accumulate. We next attempted to detect **2a** using sensitive but non-quantitative MS techniques.

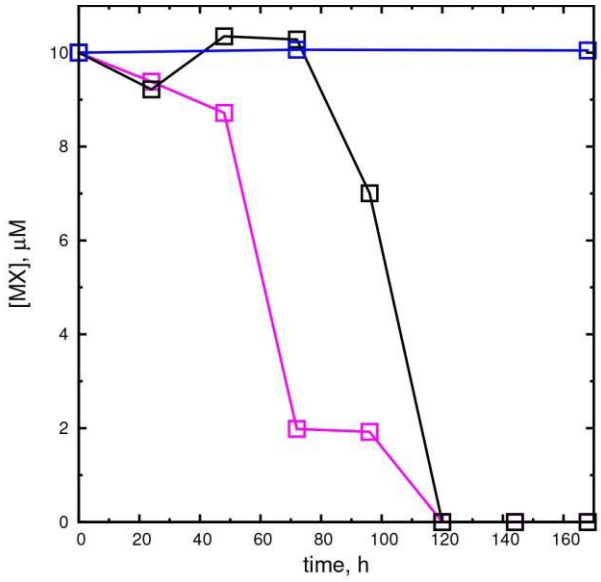

Figure 3.12. 2a decomposes in unfiltered reaction mixtures containing AarCH6. HPLC analysis after heat quenching was used to monitor the decay of 2a (initially 10 µM) in reaction mixtures containing: 10 µM AarCH6, magenta symbols; 10 µM AarCH6-E294A, black symbols; no enzyme, blue symbols. Only the no-enzyme control contained detectable 2a after 96 h (detection threshold 1 µM).

Identification of 1a-derived compounds containing adenine.

MALDI-TOF analysis of **1a** stability assay reaction mixtures was used to detect **1a**-derived compounds (Table S1). Spectra acquired over 168 h showed an increasing proportion of species with smaller m/z values, many of which were not identified. The largest new peaks (m/z 712, 750, and 788) corresponded to the $[M+H]^+$, $[M+K]^+$, and $[M+2K]^+$ ions of **1b** (Figure 3.13). This trio of peaks was only detected at 48, 72, and 96 h (Table S1), as expected for a transient intermediate in a multi-step **1a** degradation process. Since the **1b** $[M+K]^+$ and **2a** $[M+H]^+$ ions are isobaric (expected m/z 750.17), MS/MS daughter ion fragmentation patterns were recorded and compared to those for authentic **1a** (Figure 3.14) and **2a** (Figure 3.15) standards. A MS/MS spectrum of the m/z

750.17 peak observed at 96 h in a **1a** stability assay contained several daughter ions unique to **1b** but none unique to **2a**, together with daughter ions that could derive from either compound (Figure 3.16). In addition, several prominent daughter ions in the synthetic **2a** spectrum (Figure 3.15) were not detected. While we cannot rule out the possibility of a small amount of **2a** formation, **1b** is the best assignment of the m/z 750.17 ion.

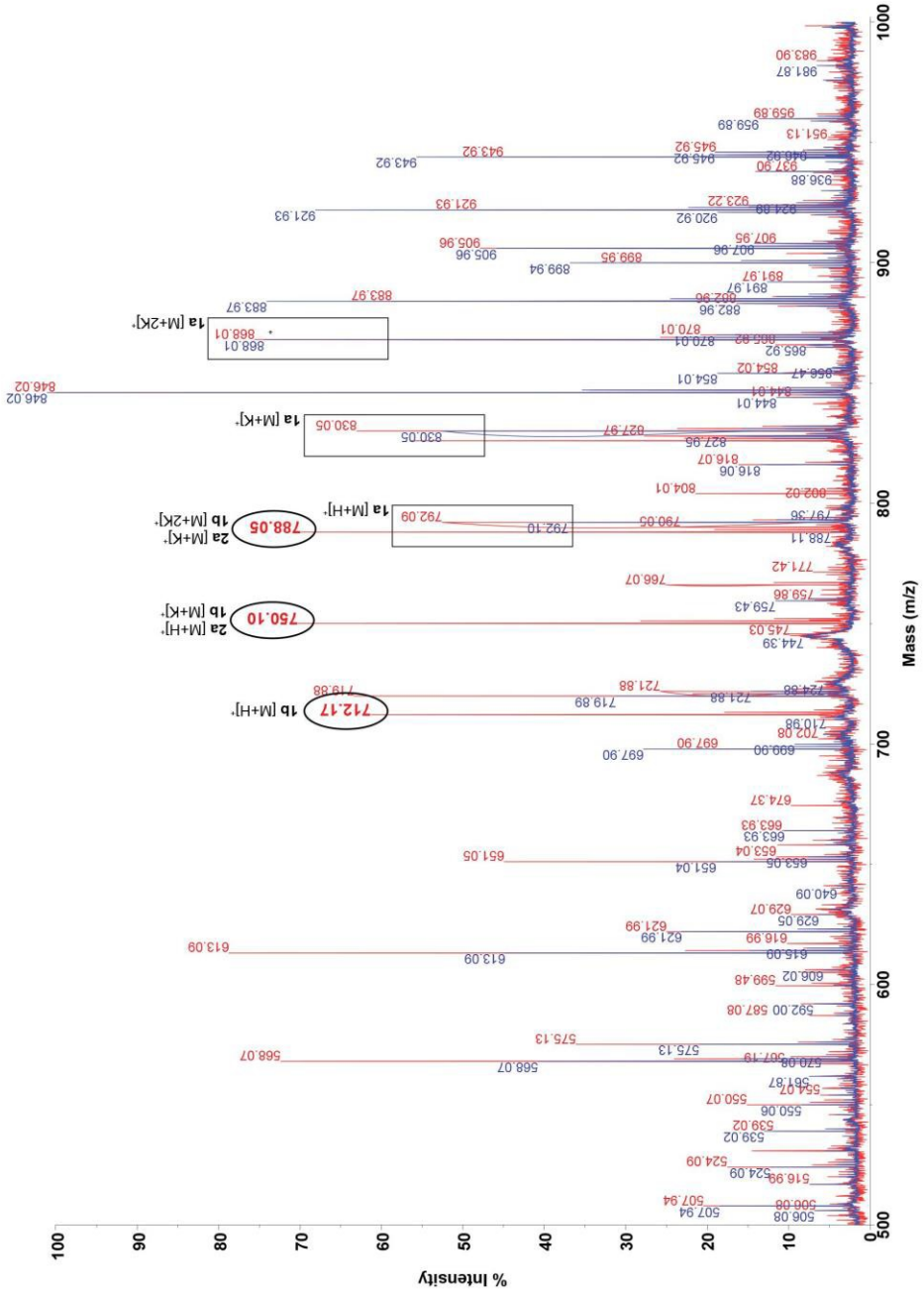

Figure 3.13. MALDI-TOF detection of compounds formed during 1a decomposition. Spectra (positive ion mode) obtained using complete reaction mixtures from t=0 (blue spectrum) and 96 h (red spectrum) are superimposed. Boxes highlight 1a peaks and circles new peaks consistent with the production of 2a (expect m/z 750.17 for [M+H]+, m/z 788.12 for [M+K]+) or 1b (expect m/z 719.21 for [M+H]+, m/z 750.17 for [M+K]+). Note that the 2a and monopotassium 1b ions are isobaric. These peaks were only detected at 48, 72, and 96 h.

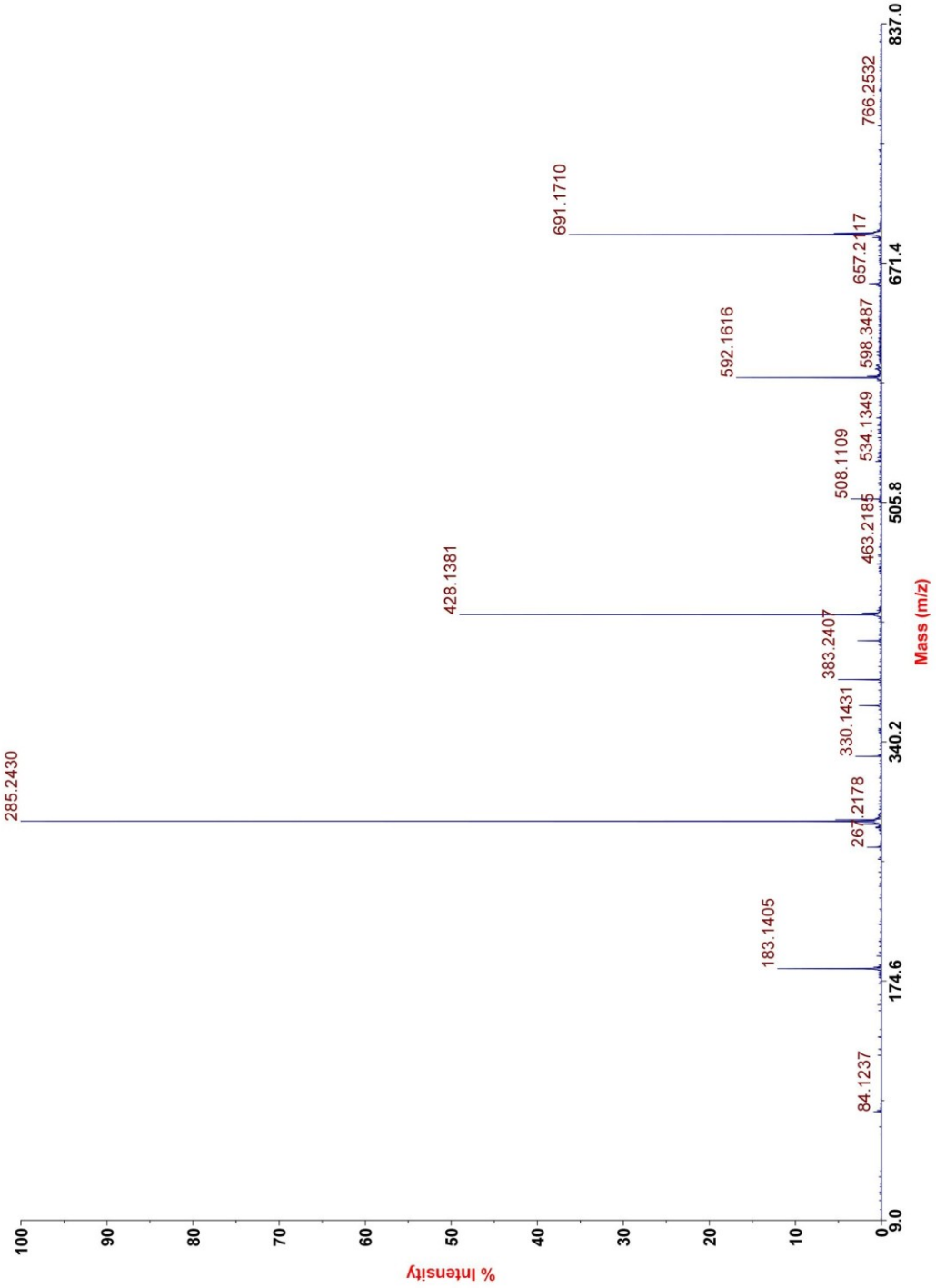

Figure 3.14. MS-MS spectrum of synthetic 1a.

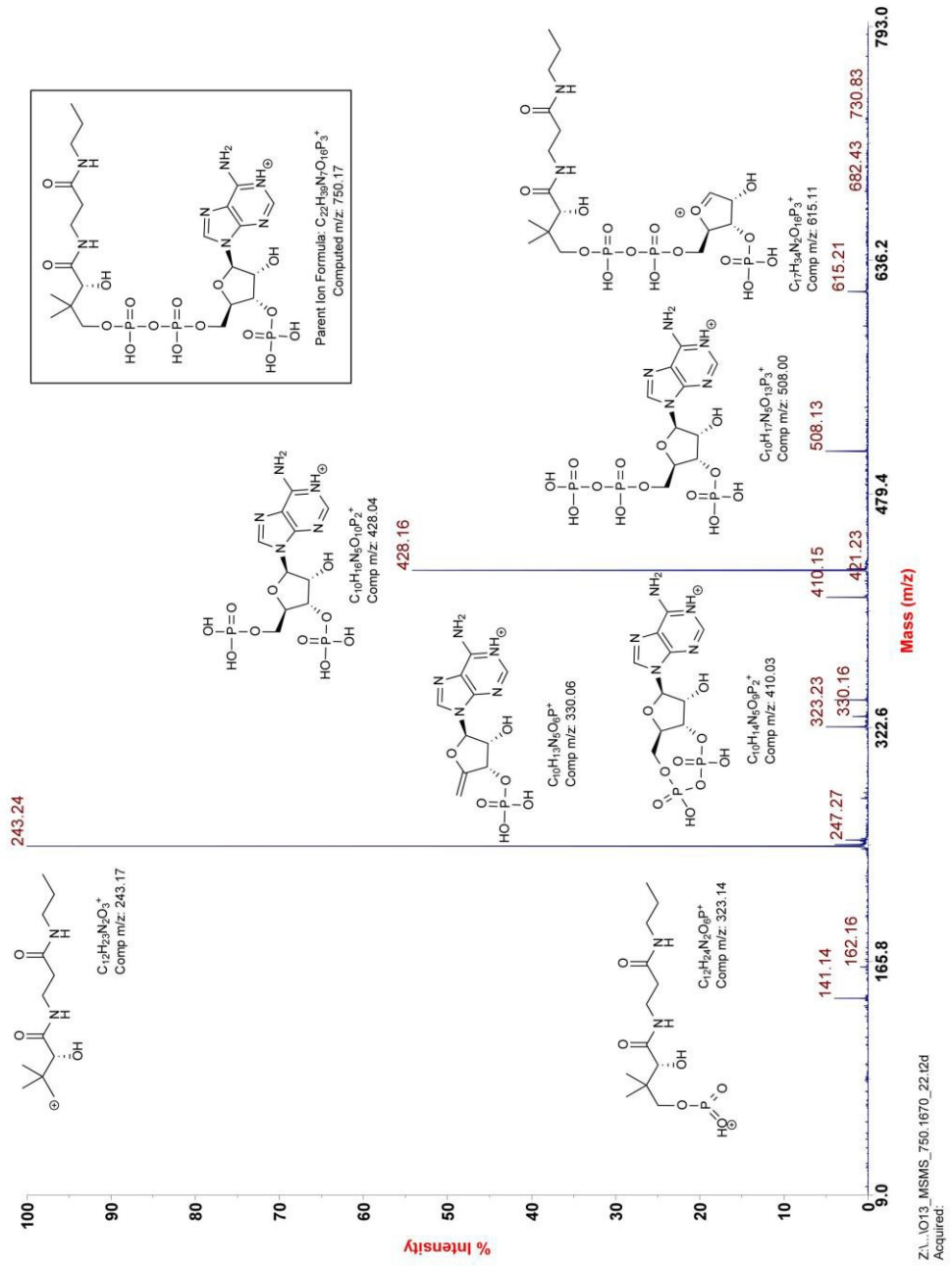

Figure 3.15. MALDI-MS/MS (positive ion mode) fragmentation of a m/z 750.17 ion obtained from synthetic 2a. Potential daughter ion structures, chemical formulae, and computed m/z values are provided for prominent peaks. Protonation is presumed to occur at adenine N1 (pKa ~3.6; Kapinos et al., 2011) in daughter ions that possess an adenine ring, but is speculative for others.

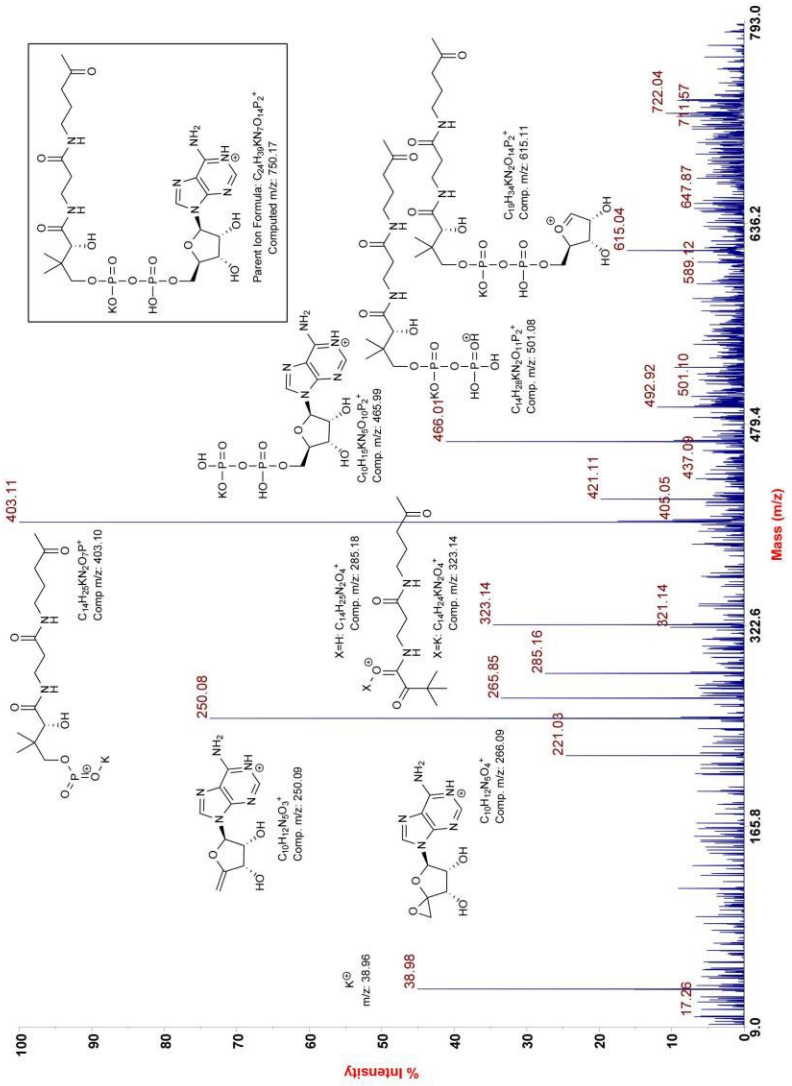

Figure 3.16. MS/MS analysis of a candidate 1b ion formed during 1a decomposition. 2a and monopotassium 1b (Figure 3.13) give isobaric parental ions (m/z 750.17). To discriminate between these possibilities, an MS/MS spectrum of the 750.17 ion was obtained from the 96 h sample (red spectrum, Figure 3.15). The observed MS/MS spectrum is a poor match to the MS/MS spectrum of synthetic 2a (Figure 3.15). Speculative structures for selected potassium 1b daughter ions are given.

As a preliminary test of whether **1b** is an obligatory intermediate in **1a** decomposition, CoaE (dephospho-CoA kinase) and ATP were added to a **1a** stability assay. After 196 h, 98% of the original **1a** was recovered, compared to 27% in a reaction mixture lacking CoaE and ATP, and 105% of a no-enzyme control. The protective effect of CoaE, together with kinetic evidence that **1c** is a non-preferred substrate (Figure 3.11), is most consistent with **1a** dephosphorylation as the first step in **1a** decomposition.

MS spectra were searched for ions consistent with known or hypothetical compounds that might be produced during **1a** decomposition. This was hampered by a mass ambiguity: the replacement of a phosphoryl group with a hydrogen leads to a loss of 80 amu, as does the replacement of an acetyl group and a potassium with two hydrogens. Attempts were made to eliminate these ambiguities by cation exchange and solid phase extraction. Both attempts resulted in loss of all previously detected ions (data not shown). As one consequence of the mass ambiguity, the all-protonated **2a** ion is isobaric with the monopotassium **1b** ion (Figure 3.13). First, we looked for ions that appeared during the course of **1a** decomposition that would be consistent with shortening of the aminopentanone moiety in **1a** or **1b**. Singly charged ions (containing 0, 1, or 2 potassium atoms) consistent with **3a**, **4a**, or dephosphorylated (Figure 3.2; **3b** and **4b**, respectively) products were not detected. We also did not identify ions consistent with oxygenated (+14 or +16 amu) forms of **3** or **4** (Table S1). Second, we searched for any other ions that appeared during the course of **1a** decomposition. MALDI-TOF spectra acquired at 48, 72, and 96 h also contained new peaks at m/z 766 and 804 (Table S1),

which were consistent with either (a) $[M+K]^+$ and $[M+2K]^+$ ions of **1b** plus an oxygen atom or (b) $[M+H]^+$ and $[M+K]^+$ ions of **2a** plus an oxygen atom. (Potential structures for these ions are discussed below.) We conclude that, if progressive shortening of the **1a** or **1b** aminopentanone moiety occurs, many or all subsequent degradation steps are rapid and appear to prevent accumulation of detectable levels of chain-shortened intermediates.

Identification of 1a-derived acetate.

Acetate from an unknown source was tentatively detected in the crystal structure of AarC crystallized with **1a**. Removal of the terminal two carbon atoms from **1a** (or **1b**) might result in the formation of acetate. On the basis of this consideration, we performed two sets of experiments intended to (1) unambiguously identify acetate as a product of **1a** degradation and (2) maximize acetate recovery, to estimate the stoichiometry of acetate production from **1a**.

In the first set of experiments, ACS was used to convert acetate to AcCoA, which was in turn positively identified by HPLC retention time and quantitated by comparison to an authentic AcCoA standard (Figure 3.17). An acetate standard solution was used to determine that this assay method recovers 92% of the original acetate as AcCoA (data not shown), with losses presumed to originate from sample processing and transfer steps. After 168 h, approximately 40 µM acetate was produced, corresponding to a 40% yield (uncorrected) relative to the initial **1a** concentration (Figure 3.18). No other acyl-CoA peaks were detected in HPLC chromatograms. This experiment is highly specific for acetate and places a *lower* limit on the stoichiometry of acetate recovered from **1a.**

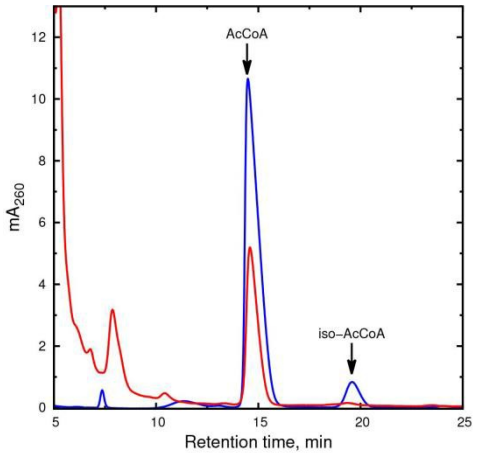

Figure 3.17. Acetate is produced during 1a decomposition. ACS was used to convert acetate present in 1a stability assay reaction mixtures to AcCoA, which was in turn unambiguously identified by HPLC analysis. Unambiguously identifying acetate production. Blue trace, chromatogram obtained using an authentic AcCoA standard. Red trace, chromatogram demonstrating ACS-mediated formation of AcCoA from 1a stability assays (96 h time point).

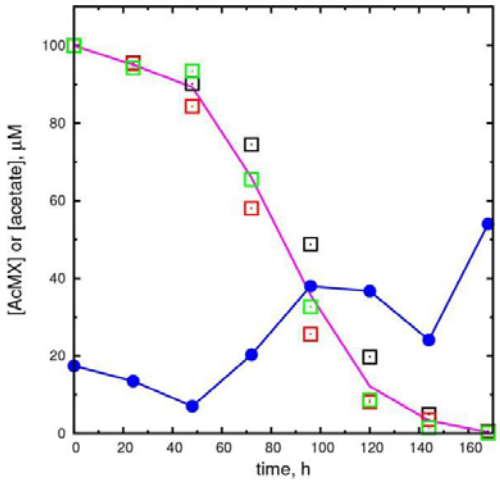

Figure 3.18. Alternative method for quantitation of acetate produced from 1a. Intact 1a was detected and quantitated by HPLC in three independent time courses (open squares of different colors). The average [1a] is depicted here with a magenta line, and in Figure 3.7 with a line and error bars. The blue filled circles depict acetate detected using ACS in aliquots from 1a stability assay (green open squares).

In the second set of experiments, AK was used to convert acetate and ATP to acetyl phosphate and ADP, which was quantitated using a standard PK/LDH coupled ATPase assay. A set of standards demonstrated quantitative recovery of acetate, a detection limit of 0.1 nmol acetate (1–2% of the initial **1a**, and linearity to at least 100 μM acetate (Figure 3.19). Decomposition reaction mixtures analyzed with a no-AK control showed negligible NADH oxidation. Acetate was detected after 20 h of **1a** incubation and reached a maximum at 168 h, corresponding to a 88% yield relative to the initial **1a** concentration. As a one-pot assay, this assay minimizes sample losses but does not rule out the possibility of uncoupled ATP hydrolysis or that alternate substrates for coupling enzymes are produced during **1a** breakdown. This experiment therefore places an *upper* limit on the stoichiometry of acetate recovered from **1a** breakdown.

To identify the source of acetate, **2a** (100 μM) was allowed to degrade and products were analyzed using the quantitative (AK-coupled) method. After 168 h, 80% of the **2a** was gone, but little or no acetate was produced: ~5 μM, or 5% of the initial [**2a**]. Given an uncertainty of perhaps 10 μM, the evidence from this preliminary experiment indicates that **2a** does not serve as a source of acetate. We therefore infer that the near-stoichiometric conversion of **1a** to acetate requires a microbe-mediated cleavage of the aminopentanone moiety, and may involve excision of the terminal two-carbon unit.

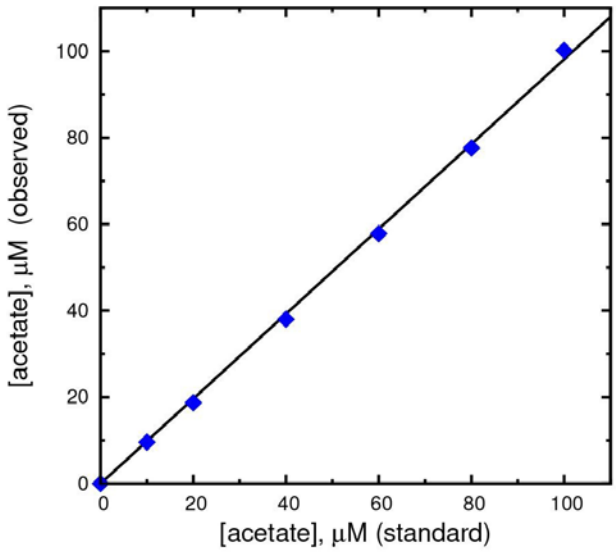

Figure 3.19. Linear response of acetate determination assay. A standard acetate solution was analyzed using the AK-dependent PK/LDH ATPase assay. A final volume of 70 µL contained 0→100 µM acetate (0→7 nmol acetate total). The ΔA340 value recorded in the zero-acetate sample was used as a background for the other concentrations (symbols). A linear fit to the data, forced to pass through the origin, has slope 0.981 ∓ 0.009 (solid line).

Crystallization of AarC with acetate.

Acetic acid or acetate (collectively "acetate") has been observed in several AarC structures without being provided in the crystallization solution. *A. aceti* normally contains high levels of cytoplasmic acetate (Menzel and Gottschalk, 1985; Steiner and Sauer, 2003), which is therefore likely to be the predominant protein-associated small anion. We crystallized AarC with exogenous acetate to identify potential binding sites for **1a**-derived acetate (PDB entry 5dw4). The final model contained three acetate binding sites in each subunit, related by the pseudo-twofold axis.

The first acetate binding site is near the active site and has been observed to bind acetate formed by AcCoA hydrolysis (PDB entry 4eu6 subunit B). Acetate (ACT 606A and

603B) accepts hydrogen bonds from the side chains of Ser71, Thr94, and Arg228 (Mullins and Kappock, 2012). This is the only acetate binding site not located at the rather polar interface between subunits.

The second acetate binding site overlaps a chloride binding site (CL 515) observed in earlier structures and is located on the flanks of the dimer. Acetate (ACT 605A and ACT 605B) accepts hydrogen bonds from the side chains of Asn112, Arg120, and Asn125 of the same subunit and the backbone of Gly443' (the prime denotes a residue from the partner subunit).

The third acetate binding site overlaps the other chloride binding site (CL 516) observed in earlier structures and is located near the pseudo-twofold axis on the flat "top" of the dimer. Acetate (ACT 607A and 601B) accepts hydrogen bonds from the side chains of Arg354 (bidentate) and Arg354' (monodentate) and the backbone NH of Val196'. Protein atoms in the interfacial acetate and chloride binding sites are nearly superimposable, indicating that the acetate displaces chloride ions supplied by the buffers used to isolate and crystallize recombinant AarC(H6).

Acetate crystals lacked the buffer-derived citrate ligands observed in earlier "open" structures (PDB entries 4eu3, 4eu7, and 4eud). As anticipated, each subunit in the AarC•acetate complex possesses active site parameters typical of other open conformations (Figure 3.3).

Crystallization of AarC with 2a.

Crystallography cannot unambiguously identify **2a** as the ligand in AarC crystals grown with **1a** (denoted AarC+**1a**). The putative **2a** propyl sidechain has relatively high B-factors, as expected for a flexible, nonpolar group in an open, polar active site (PDB entry 5e5hA). AarC was crystallized with synthetic **2a** to compare an authentic AarC•**2a** complex with the AarC+**1a** structure. AarC•**2a**•acetate crystals were grown either with acetate present in the initial crystallization solution or with acetate added long after AarC•**2a** crystals formed. Several X-ray data sets were collected using crystals from drops that initially contained either **2a** or **2a**+acetate; all diffracted to 1.66 Å resolution. A better data set (PDB entry 5dw6) was obtained from a crystal that was grown in the presence of **2a** prior to the addition of acetate.

The AarC•**2a** complex (PDB entry 5dw5) contained three chloride ions, one near the pseudo-twofold axis and two on the flanks of the dimer. One of the latter chlorides (CL 601A) and an acetate ligand (ACT 601B) were located so close together we assumed that they could not be simultaneously present. The final refined fractional occupancies were 63% and 37%, respectively. The acetate orientation was different from that observed in the AarC•acetate complex (PDB entry 5dw4): it accepted a hydrogen bond from the side chain of Asn112A. Since acetate was not intentionally added to this crystal, we considered but ultimately discarded the possibility that a formate was carried over from the isolation of **2a**. Other aspects of the structure were essentially the same as described next for acetate-soaked crystals, other than replacing chloride ions associated with two different sites in each subunit (Mullins and Kappock, 2012). An acetate-capped,

solvent-filled tunnel provides a possible path for entry of two buried acetates near the pseudo-twofold axis.

The AarC•**2a**•acetate complex (PDB entry 5dw6) contained **2a** and an acetate in each active site, with four acetate ligands at the subunit interface (two on the flanks of the dimer and two at the pseudo-twofold axis). Subunits A and B adopt the open and closed conformations, respectively (Figure 3.3). An in-plane ~120° rotation of the active-site acetate ligand in subunit B, relative to previous orientations (e.g., PDB entry 4eu6), gave a slightly better fit to the data. This may be related to the exclusion of the carboxylate-binding residue Arg228B from the closed active site. A bow-shaped, 65 Å long, narrow (average width ~2 Å), and hydrophilic tunnel was plugged by the two flank-binding acetates that supplant chloride ions (Figure 3.8). Eight basic and zero acidic residues line the tunnel, but only the acetate binding sites have a substantial positive charge. Crystals containing **2a**, including those grown without added acetate, did not contain ordered citrate ligands, even though subunit A adopts an open conformation and the crystallization conditions were, apart from CoA, identical to those that yielded AarC(H6) crystals with a citrate in each active site (PDB entries 4eu7 and 4eud).

The CoA analogue **2a** binds in the same orientation in the two active sites (Figure 3.20), which is notable because one is open (subunit A) and the other is closed (subunit B). In the fully closed conformation, a hydrogen bond was observed between Val270 carbonyl and the OAP hydroxyl in the pantoic acid moiety of **2a**. Relative to the AarC+**1a** structure (PDB entry 5e5h), the **2a** propyl group is closer to a fully extended conformation; the orientations differ by a 107° rotation about the C2P–C3P bond. The terminal group

that is modeled as a methyl in the **1a**-derived molecule has a close contact with the nearest carboxylate oxygen atom in Glu294A (3.1 Å). In contrast, the structure containing authentic **2a** adopts an almost perpendicular conformation that buries the terminal methyl in a largely hydrophobic region ~4 Å from Gln267A CG, Glu294A CG, Gly388 CA, and the Phe392 phenyl ring. Density associated with the 3' phosphoryl was unambiguous for the AarC•**2a**(•acetate) structure but not for the **1a**-derived molecule. In summary, AarC crystals grown with chemically defined ligands including **2a** did not recapitulate the structure obtained with **1a** under conditions associated with its decomposition. This likely arises from differences in crystallization kinetics and conditions or the presence of different ligands. We favor the latter as a working hypothesis, as the terminus of the **1a**-derived ligand appears to be more polar and perhaps somewhat larger than the aminopropyl group in **2a**.

Attempts to crystallize AarC with **3a**, with and without exogenous acetate, yielded only clear drops devoid of crystals.

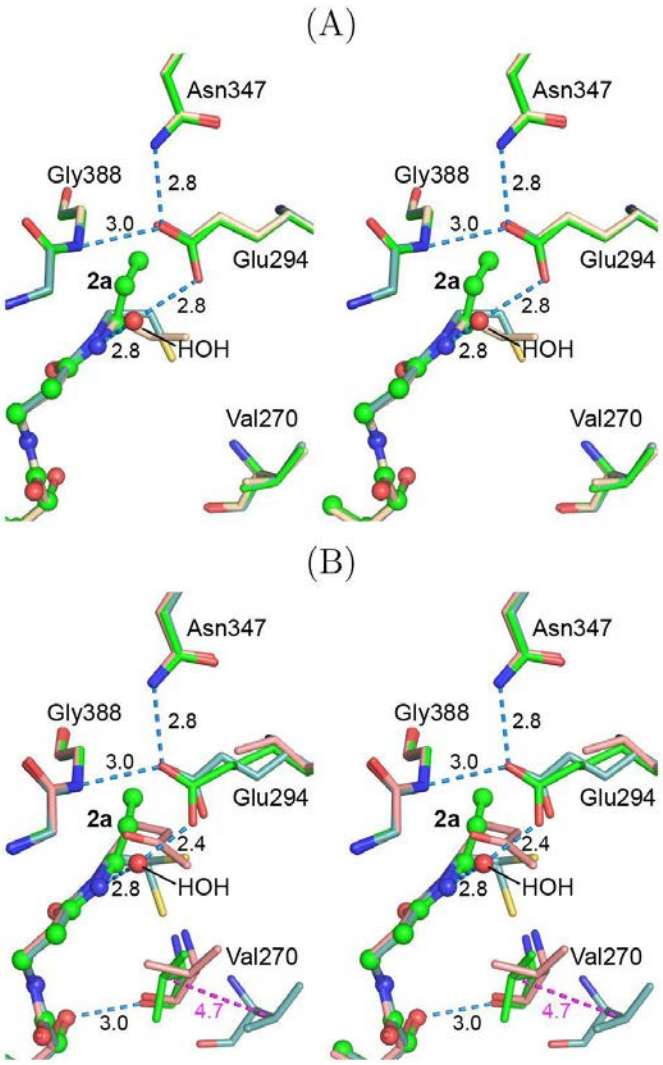

Figure 3.20. Stereograms of the AarCH6●2a●acetate active sites. (A) Subunit A, in the open conformation for all structures depicted. Carbon atoms in superposed B subunits are green in AarCH6●2a●acetate (PDB entry 5dw6; spheres are shown for 2a and HOH 923A), wheat in AarCH6+1a (PDB entry 5e5h), and light blue in AarCH6●citrate (PDB entry 4eu7). (B) Subunit B, in the closed conformation except where indicated. Carbon atoms in superposed B subunits are green in AarCH6●2a●acetate (PDB entry 5dw6; spheres are shown for 2a and HOH 713B), salmon in AarCH6-E294A●**1a** (PDB entry 4euc), and light blue in AarCH6●citrate (PDB entry 4eu7, open conformation). Distances (in dashed lines) are shown for 5dw6 hydrogen bonds and the shift of Val270B CB from the open to closed conformation (magenta). The orientation is the same as Figure 3.4.

3.4 Discussion

Enzyme substrates that incorporate large cofactors, such as acyl-CoAs, form extensive protein-ligand interfaces that can increase substrate specificity, enzyme reaction rates, and thereby metabolic flux. For example, bacterial biosynthetic enzymes recognize NADPH, against a 20-fold excess of NAD+ (Bennett et al., 2009), using its remote 3'-phosphate. Nonreactive regions of a large substrate contribute "intrinsic binding energy" that enzymes such as the CoA-transferases may exploit in catalysis (Jencks, 1975). Jencks and co-workers showed that remote interactions further accelerate successive acyltransfer and thiolysis reactions (Moore and Jencks, 1982a) initiated by tight clamping of the acyl-CoA thioester by the enzyme (White and Jencks, 1976). This prediction was later confirmed by crystal structures showing progressive constriction of the AarC active site (Mullins and Kappock, 2012).

Analogue studies show that the ADP and pantoate moieties of CoA have opposing effects on glutamyl-CoA thioester stability: the nucleotide supplies binding energy used to pull the pantoate moiety into the active site and form a thioester whereas subsequent interactions between the enzyme and pantoate moiety are destabilizing and increase thioester reactivity toward carboxylates (Whitty et al., 1995). A substrate split into "pieces" can sometimes form an alternative Michaelis complex that undergoes chemical conversion (Amyes and Richard, 2013). Class I acyl-CoA transferases, however, fail this test: only a covalently linked ADP moiety confers a rate increase (Fierke and Jencks, 1986). This suggests that substrate conformational dynamics and mechanical coupling within the

ligand are important aspects of harnessing binding affinity to achieve catalytic rate accelerations.

Analogue studies have not yet explained how CoA-transferases productively engage valid acyl-CoA substrates but discriminate against unproductive interactions with free CoA, which possesses nearly all of the same features (Fierke and Jencks, 1986). Most interactions of free CoA with the open conformation of AarC are mediated by waters that are squeezed out when the active site closes, with a corresponding gain in entropy (Mullins and Kappock, 2012). One practical advantage of this inability to close the active site, and thereby assemble a functional active site, is that free CoA is not a strong enzyme inhibitor (Blair, 1969); inhibition of AarC by CoA is competitive (K_i = 16 μM) and comparable to acyl-CoA substrate K_M values (Mullins, 2012). In addition to the important role the "viselike grip" exerted in the immediate vicinity of the acyl-CoA thioester has on catalysis (White and Jencks, 1976), we suggest that AarC, and by extension other class I CoA-transferase active sites, positively recognizes free CoA to prevent the final stage of active site closure.

Distinguishing CoA from acyl-CoA.

Conformational dynamics regulate CoA-transferase chemistry, since only completely closed complexes contain both a complete external oxyanion hole and properly oriented Val270, which are needed to initiate reactions with acyl-CoA substrates. A key to furthering the understanding of CoA-transferases is therefore to generate crystals containing closed active sites, using mutant enzymes or substrate analogues that cannot undergo a complete enzymatic reaction.

In our first set of AarC structures (Mullins and Kappock, 2012), we observed complete active site closure but only in complexes of mutants with, among other effects, enlarged active site pockets (S71A or E294A in PDB entries 4eu8B, 4eub, and 4euc; Figure 3.3). The most closed structure of wild-type AarC bound to CoA (PDB entry 4eu5B) shows Val270 in a closed conformation, Arg228 in the open (inward) position, and the 230s loop in an intermediate location (Figure 3.3). Crystal-packing interactions characteristic of the subunit B active site may bias the protein conformation and favor formation of a Val270 amide-CoA thiolate contact.

In the current work, we have used substrate analogues to trap closed complexes. While co-crystallization of AarC with **1a** gave ambiguous results, the attempt to reproduce this complex with authentic **2a** yielded the first completely closed complexes of the wild-type enzyme (PDB entries 4dw5B and 4dw6B; Figure 3.3). The position of Glu294, buttressed by Asn347, remains largely unchanged in the closed complex, lending further support to the idea that enzyme closing exerts mechanical forces that favor attack of the nucleophile with the acyl-CoA substrate (inset, Figure 3.1). Other polar groups within the active site, such as the mobile Val270 residue, occupy locations that are consistent with roles in catalysis proposed previously. Moreover, these residues adopt similar orientations in crystal structures of mutant AarC complexes. By pre-positioning the Val270 amide that is proposed to stabilize the CoA thiolate leaving group, the enzyme facilitates reactions involving the key acylglutamyl anhydride intermediate.

In PDB entry 4eu6A, the CoA thiol(ate) adopts a near-attack position equidistant from the external and internal carbonyl carbon atoms of a trapped acetylglutamyl anhydride. In **2a** complexes, an inward rotation of the C2P-C3P bond moves the corresponding methyl terminus into a small pocket in both open (PDB entries 4dw5A and 4dw6A) and closed (PDB entries 4dw5B and 4dw6B) complexes (Figure 3.4). A CoA sulfur forced into this pocket would encounter electrostatic clashes with electron-rich carbonyl oxygen atoms in Gly388 and the Glu294 carboxylate. The **2a** terminus is rotated by ~120° relative to the outward-facing CoA thiol(ate) observed in open active sites and the mostly closed active site (PDB entry 4eu5B). In this location, the **2a** methyl terminus appears unlikely to affect active site conformational dynamics. A detailed comparison shows that other regions of bound CoA and **2a** adopt the same conformations. Similarly, there are few differences in the protein region between CoA and the surface-located 230s loop that might account for the more-open conformation of the latter.

The principal difference seems to be whether the ligand makes a polar contact with the Glu294 carboxylate, an interaction that we propose "props open" the active site and inhibits the final steps in active site closure. In PDB entry 4eu5B, the outwardly rotated CoA sulfur atom is 2.9 Å from the closest Glu294B carboxylate oxygen atom, 3.4 Å from the Val270 nitrogen atom, and 12 Å from the closest guanidinium nitrogen atom of the inward-facing Arg228B. Since a CoA thiolate could not form so close to a carboxylate, a CoA thiol may be stabilized by a hydrogen bond involving Glu294. No such interaction is possible in the fully closed complexes observed for AarC-E294A•CoA (PDB entry 4eub), AarC-E294A•**1a** (PDB entry 4euc), or AarC•**2a** (PDB entries 4dw5/6B).

Maintaining CoA at the proper cytoplasmic concentration and relative ratio to the acyl-CoA pool allows effective carboxylate utilization and regulates flux through central metabolism (reviewed recently by Hentchel and Escalane-Semerena, 2015). The ability to positively recognize CoA and prevent diversion of its binding energy into the formation of a dead-end closed complex would therefore confer an evolutionary advantage on diverse CoA-transferases. Positive and highly specific selection for CoA binding could also explain why oxy-CoA is more potent than CoA as an inhibitor of mammalian succinyl CoA:3-ketoacid CoA-transferase (Jencks, 1973).

The mechanism by which a single polar contact might prevent the distant 230s loop from fully closing may involve protein-ligand dynamics sensitive to the CoA thiol-carboxylate contact. The failure of "split substrates" to support efficient CoA-transferase catalysis similarly implicates dynamic effects of an intact CoA moiety as a regulator of the open/closed protein conformational equilibrium.

Internal oxyanion hole residue Asn347 reinforces Glu294.

Oxyanion holes are typically rigid features tasked with precise dipole positioning (Kamerlin et al., 2010). The AarC-N347A mutant was designed to perturb the internal oxyanion hole and thereby to slow enzyme chemistry, which is not rate-limiting in wild-type enzyme steady-state kinetics (White and Jencks, 1976). A relatively high residual activity (Mullins and Kappock, 2012) suggested that an additional active site water might restore the function of the mutated internal oxyanion hole. Ordered waters observed near the site of each missing carboxamide appear to confirm this suspicion, which

indicates that AarC-N347A cannot be used to completely stop CoA thiolysis nor preferentially stabilize acylglutamyl anhydride intermediates. The crystal structure suggests that Asn347 orients and thereby affects the function of Glu294 in multiple roles: as nucleophile, part of internal oxyanions, and in positioning external oxyanions. While these findings are consistent with our prior hypothesis that the N347A mutant primarily affects enzyme chemistry, it now seems more likely that reactions at *both* anhydride carbonyls are affected, not just those involving the internal carbonyl.

Two large families within the class I CoA-transferase superfamily have different, highly conserved carboxamide residues, which suggests that the internal oxyanion hole is more tolerant of variation than the strictly conserved external oxyanion hole. One potential reason for this difference is that the internal oxyanion hole is preorganized whereas part of the external oxyanion hole is mobile, delivered by the CoA itself, and must adopt the correct configuration prior to or during active site closure (Mullins and Kappock, 2012). In addition, the covalent attachment of Glu294 to the rigid C-terminal beta-sheet may limit the intrinsic flexibility of the anhydride internal carbonyl, thereby increasing its reactivity relative to the distal external carbonyl.

*A working hypothesis for **1a** cleavage.*

The class I CoA-transferase external oxyanion hole is composed of two amide dipoles, the backbone nitrogen of Gly388 and the distal amide nitrogen of the substrate itself (Mullins and Kappock, 2012). We hypothesized that **1a**, a competitive inhibitor that binds tightly to AarC (K_i = 17 μM, K_d = 0.8 μM; Mullins et al., 2008), could be used to trap a stable hemiacetal analogue of the external oxyanion in a fully closed active site. This

experiment was thwarted by unexpected microbe-mediated truncation of the substrate analogue, which ultimately resulted in complete consumption of the organic ligand. (Attempts to crystallize the hemiacetal complex under sterile conditions are ongoing.)

Since **1a** degradation is slow and follows a long lag period, it was not previously detected during routine activity assays but it was remarkably reproducible: **1a** degradation was observed in eight out of nine trials with independently purified batches of AarC or an inactive mutant, indicating that **1a** cleavage has nothing to do with AarC activity. We speculate that the lag in **1a** degradation is due to the induction of microbial enzymes, including the postulated 3'-phosphatase.

We prepared AarC•**2a** crystals in an attempt to positively identify the **1a**-derived species, but instead obtained a fully closed complex (discussed above) that was distinctly different from the partly open complex obtained from AarC and **1a**. One explanation might be the presence of a 3'-phosphate moiety in **2a**, which was missing in at least one subunit of the structure derived from AarC and **1a**. We discount this explanation, given that the 3'-phosphate is largely solvent-exposed and prior work that indicates that it has little influence on substrate affinity (Whitty et al., 1995; Mullins and Kappock, 2012). A more likely explanation for the difference is the absence of an acetylglutamyl anhydride from the AarC•**2a** crystals; crystals obtained from AarC+**1a** adopt an intermediate conformation characteristic of other covalent adducts (Figure 3.3, lower right quadrant) that may protect the labile anhydride. Indeed, the absence of a CoA thiolate in **2a** would facilitate anhydride hydrolysis, particularly in solution, which could explain why the borohydride-trapping treatment failed to detect anhydride adducts.

The observation of an acetylglutamyl anhydride in the crystalline lattice (PDB entry 5e5h) and the direct detection of acetate production in solution from **1a** but not **2a** indicate that the **1a** ketone is converted to an activated acetyl donor. Oxidation of **1a** or a degradation product by at least one microbial enzyme provides a straightforward and concise, albeit speculative, route to an activated acetyl group: a Baeyer-Villiger monooxygenase (BVMO) acting on **1a** could yield ester **5a** (Figure 3.21). Short-chain alkyl methyl ketones that resemble the aminopentanone terminus of **1a** are converted to acetate esters by a *Pseudomonas* BVMO (Onaca and Kieninger, 2007).

Intriguingly, while **5a** resembles AcCoA and would be well-suited to acylate Glu294, the product alcohol **6a** (Figure 3.21) could not perform subsequent steps in the AarC reaction. For example, **6a** would be less nucleophilic than CoA, which might selectively stabilize the acetylglutamyl anhydride and account for its detection by crystallography. The near-stoichiometric appearance of acetate and disappearance of **1a** in solution studies is also consistent with irreversible conversion of **1a** to an activated acetyl donor (Figure 3.7).

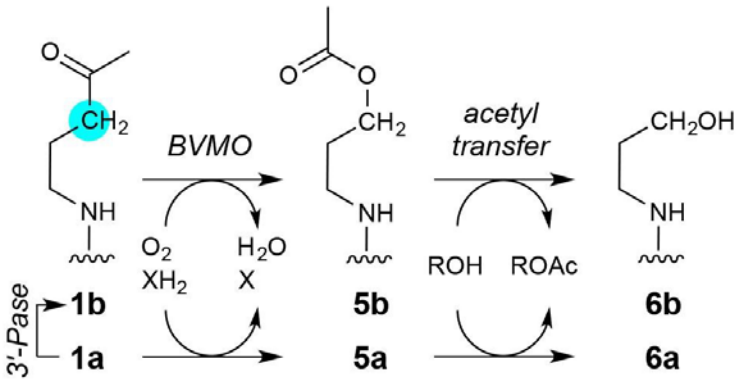

Figure 3.21. Speculative pathway for 1a degradation by microbial enzymes. The key step would be oxidation of the **1a** ketone carbonyl by a Baeyer-Villiger monooxygenase (BVMO), yielding **5a**. Unlike **1a**, **5a** contains an activated acetyl moiety capable of producing both an acetylglutamyl anhydride adduct (Figure 3.6) and free acetate (Figure 3.10). The other product of acyl transfer, **6a**, appears to be degraded rapidly by undefined enzymes. The intermediate detection of 1b suggests that a 3'-phosphatase (3'-pase) may compete with, or form the substrate for, BVMO. Mass spectrometric evidence supporting the first alternative, parallel pathways for **1a** degradation, is detailed in Figure 3.22.

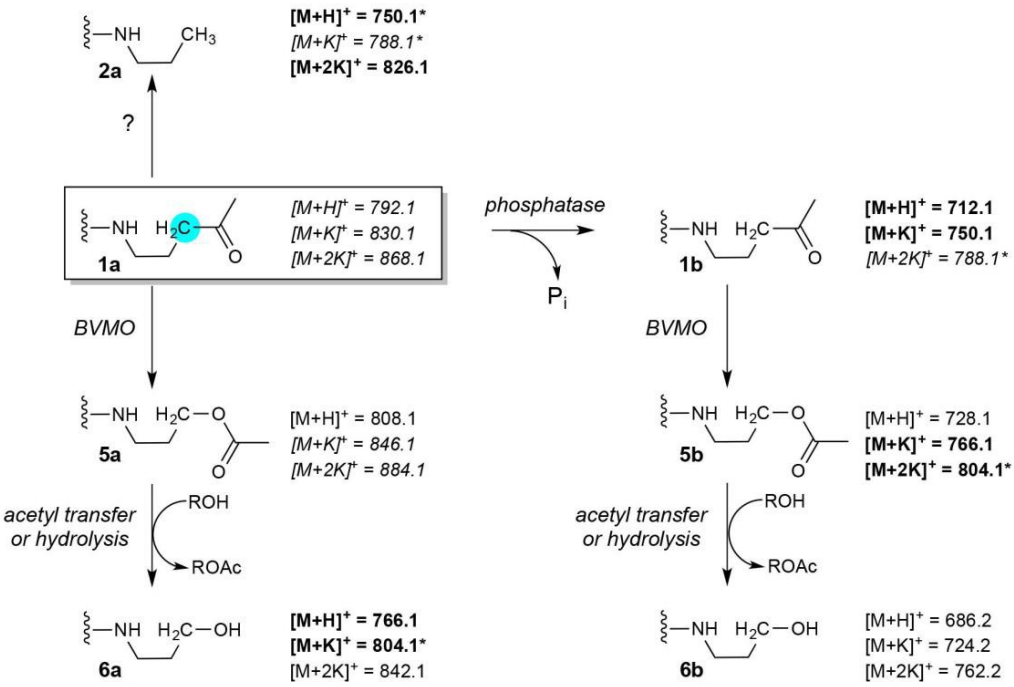

Figure 3.22. Speculative pathways for 1a degradation by microbes. If BVMO is present, it could act on either 1a or 1b. m/z peaks indicated with an asterisk were detected in spectra other than t=0, italicized values were detected at time points including t=0, and normal text were not detected.

The terminus of the **1a**-derived CoA analogue, presently modeled as an alkyl chain (PDB entry 5e5h), occupies a more open active site and a more polar region than the terminus of authentic **2a**. These discrepancies might be explained if the former is actually **6a** with a partially disordered alcohol terminus. Finally, the possibility that **5a** can form a long-lived anhydride intermediate suggests future experiments with authentic **5a** or *O*-acetyl oxyCoA, an analogue with one fewer methylene. AarC acylating reagents like these may enable the stoichiometric preparation and trapping of fully closed, covalently modified enzyme active sites.

3.5 References

1. Adams, P. D., Afonine, P. V., Bunkóczi, G., Chen, V. B., Davis, I. W., Echols, N., et al. (2010). *PHENIX*: a comprehensive Python-based system for macromolecular structure solution. *Acta Crystallogr. D Biol. Crystallogr.* 66, 213–221. doi:10.1107/S0907444909052925

2. Amyes, T. L. and Richard, J. P. (1992). Generation and stability of a simple thiol ester enolate in aqueous solution. *J. Am. Chem. Soc.* 114, 10297–10302. doi:10.1021/ja00052a028

3. Amyes, T. L. and Richard, J. P. (2013). Specificity in transition state binding: the Pauling model revisited. *Biochemistry* 52, 2021–2035. doi:10.1021/bi301491r

4. Bennett, B. D., Kimball, E. H., Gao, M., Osterhout, R., Van Dien, S. J., and Rabinowitz, J. D. (2009). Absolute metabolite concentrations and implied enzyme active site occupancy in *Escherichia coli*. *Nat. Chem. Biol.* 5, 593–599. doi:10.1038/nchembio.186

5. Berman, H., Henrick, K., and Nakamura, H. (2003). Announcing the worldwide Protein Data Bank. *Nat. Struct. Biol.*10, 980. doi:10.1038/nsb1203-980

6. Blair, J. B. (1969). Skeletal muscle coenzyme A transferase. Purification and properties. *J. Biol. Chem.* 244, 951–954

7. Bürgi, H. B., Dunitz, J. D., and Shefter, E. (1973). Geometrical reaction coordinates. II. Nucleophilic addition to a carbonyl group. *J. Am. Chem. Soc.* 95, 5065–5067. doi:10.1021/ja00796a058

8. Burns, K. L., Gelbaum, L. T., Sullards, M. C., Bostwick, D. E., and May, S. W. (2005). Iso-coenzyme A. *J. Biol. Chem.* 280, 16550–16558. doi:10.1074/jbc.M411898200

9. Calder, R. B., Williams, R. S., Ramaswamy, G., Rock, C. O., Campbell, E., Unkles, S. E., et al. (1999). Cloning and characterization of a eukaryotic pantothenate kinase gene (*panK*) from *Aspergillus nidulans*. *J. Biol. Chem.* 274, 2014–2020. doi:10.1074/jbc.274.4.2014

10. Chen, V. B., Arendall, W. B., III, Headd, J. J., Keedy, D. A., Immormino, R. M., Kapral, G. J., et al. (2010). MolProbity: all-atom structure validation for macromolecular crystallography. *Acta Crystallogr. D Biol. Crystallogr.* 66, 12–21. doi:10.1107/S0907444909042073

11. DeLano, W. L. (2002). *The PyMOL molecular graphics system*. Palo Alto, CA.

12. Emsley, P., Lohkamp, B., Scott, W. G., and Cowtan, K. (2010). Features and development of *Coot*. *Acta Crystallogr. D Biol. Crystallogr.*66, 486–501. doi:10.1107/S0907444910007493

15 Ferry, J. G. (2011). Acetate kinase and phosphotransacetylase. *Methods Enzymol.* 494, 219–231. doi:10.1016/B978-0-12-385112-3.00011-1

16 Fierke, C. A. and Jencks, W. P. (1986). Two functional domains of coenzyme A activate catalysis by coenzyme A transferase. Pantetheine and adenosine 3'- phosphate 5'-diphosphate. *J. Biol. Chem.* 261, 7603–7606

17 Francois, J. A., Starks, C. M., Sivanuntakorn, S., Jiang, H., Ransome, A. E., Nam, J.-W., et al. (2006). Structure of a NADH-insensitive hexameric citrate synthase that resists acid inactivation. *Biochemistry* 45, 13487–13499. doi:10.1021/bi061083k

18 Furdui, C. M. and Poole, L. B. (2014). Chemical approaches to detect and analyze protein sulfenic acids. *Mass Spectrom. Rev.* 33, 126–146. doi:10.1002/mas.21384

19 Hentchel, K. L. and Escalante-Semerena, J. C. (2015) Acylation of biomolecules in prokaryotes: a widespread strategy for the control of biological function and metabolic stress. *Microbiol. Mol. Biol. Rev.* 79, 321–346. doi:10.1128/MMBR.00020-15

20 Herscovitch, M., Perkins, E., Baltus, A., and Fan, M. (2012). Addgene provides an open forum for plasmid sharing. *Nat. Biotechnol.* 30, 316–317. doi:10.1038/nbt.2177

21 Jencks, W. P. (1973) "Coenzyme A transferases," in *The Enzymes*, ed. P. D. Boyer (New York; Academic Press), 3rd ed., vol. 9B, 483–496.

22 Jencks, W. P. (1975). Binding energy, specificity, and enzymic catalysis: The Circe effect. *Adv. Enzymol. Relat. Areas Mol. Biol.* 43, 219–410

23 Kamerlin, S. C. L., Chu, Z. T., and Warshel, A. (2010) On catalytic preorganization in oxyanion holes: highlighting the problems with gas-phase modeling of oxyanion holes and illustrating the need for complete enzyme models, *J. Org. Chem.* 75, 6391–6401. doi:10.1021/jo100651s

24 Kapinos, L. E., Operschall, B. P., Larsen, E., and Sigel, H. (2011) Understanding the acid-base properties of adenosine: the intrinsic basicities of N1, N3 and N7. *Chem. Eur. J.* 17, 8156–8164. doi:10.1002/chem.201003544

25 Kleywegt, G. J. (2007). Crystallographic refinement of ligand complexes. *Acta Crystallogr. D Biol. Crystallogr.* 63, 94–100. doi:10.1107/S0907444906022657

26 Lovell, J., Simon C., Word, J. M., Richardson, J. S., and Richardson, D. C. (2000). The penultimate rotamer library. *Proteins* 40, 389–408.

27 Malabanan, M. M., Amyes, T. L., and Richard, J. P. (2010). A role for flexible loops in enzyme catalysis. *Curr. Opin. Struct. Biol.* 20, 702–710. doi:10.1016/j.sbi.2010.09.005

28 Menzel, U. and Gottschalk, G. (1985). The internal pH of *Acetobacterium wieringae* and *Acetobacter aceti* during growth and production of acetic acid. *Arch. Microbiol.* 143, 47–51. doi:10.1007/BF00414767

29 Merritt, E. A. (2012). To B or not to B: a question of resolution? *Acta Crystallogr. D Biol. Crystallogr.* 68, 468–477. doi:10.1107/S0907444911028320

30 Moore, S. A. and Jencks, W. P. (1982). Formation of active site thiol esters of CoA transferase and the dependence of catalysis on specific binding interactions. *J. Biol. Chem.* 257, 10893–10907

31 Mullins, E. A. (2012). *A specialized citric acid cycle requiring succinyl-coenzyme A (CoA):acetate CoA-transferase (AarC) confers acetic acid resistance on the acidophile* Acetobacter aceti. Ph.D. Thesis, Washington University in St. Louis, St. Louis, Missouri

32 Mullins, E. A., Francois, J. A., and Kappock, T. J. (2008). A specialized citric acid cycle requiring succinyl-coenzyme A (CoA):acetate CoA-transferase (AarC) confers acetic acid resistance on the acidophile *Acetobacter aceti*. *J. Bacteriol.* 190, 4933–4940. doi:10.1128/JB.00405-08

33 Mullins, E. A. and Kappock, T. J. (2012). Crystal structures of *Acetobacter aceti* succinyl-coenzyme A (CoA):acetate CoA-transferase (AarC) reveal specificity determinants and illustrate the mechanism used by class I CoA-transferases. *Biochemistry* 51, 8422–8434. doi:10.1021/bi300957f

34 Onaca, C., Kieninger, M., Engesser, K.-H., and Altenbuchner, J. (2007). Degradation of alkyl methyl ketones by *Pseudomonas veronii* MEK700. *J. Bacteriol.* 189, 3759–3767. doi:10.1128/JB.01279-06

35 Otwinowski, Z. and Minor, W. (1997). Processing of X-ray diffraction data collected in oscillation mode. *Methods Enzymol.* 276, 307–326. doi:10.1016/S0076-6879(97)76066-X

36 Read, R. J., Adams, P. D., Arendall III, W. B., Brunger, A. T., Emsley, P., Joosten, R. P., et al. (2011). A new generation of crystallographic validation tools for the protein data bank. *Structure* 19, 1395–1412. doi:10.1016/j.str.2011.08.006

37 Sehnal, D., Svobodová Vařeková, R., Berka, K., Pravda, L., Navrátilová, V., Banáš, P., et al. (2013). MOLE 2.0: advanced approach for analysis of biomacromolecular channels. *J. Cheminform.* 5, 39. doi:10.1186/1758-2946-5-39

38 Solomon, F. and Jencks, W. P. (1969). Identification of an enzyme-*γ*-glutamyl coenzyme A intermediate from coenzyme A transferase. *J. Biol. Chem.* 244, 1079–1081

39 Steiner, P. and Sauer, U. (2003). Long-term continuous evolution of acetate resistant *Acetobacter aceti*. *Biotechnol. Bioeng.* 84, 40–44. doi:10.1002/bit.10741

40 Strauss, E. and Begley, T. P. (2002). The antibiotic activity of *N*-pentylpantothenamide results from its conversion to ethyldethia-coenzyme A, a coenzyme A antimetabolite. *J. Biol. Chem.* 277, 48205–48209. doi:10.1074/jbc.M204560200

41 Studier, F. W. (2005). Protein production by auto-induction in high density shaking cultures. *Protein Expr. Purif.* 41, 207–234. doi:10.1016/j.pep.2005.01.016

42 Teng, T.-Y. (1990). Mounting of crystals for macromolecular crystallography in a free-standing thin film. *J. Appl. Cryst.* 23, 387–391. doi:10.1107/S0021889890005568

43 White, H. and Jencks, W. P. (1976). Mechanism and specificity of succinyl-CoA:3-ketoacid coenzyme A transferase. *J. Biol. Chem.* 251, 1688–1699.

44 Whitty, A., Fierke, C. A., and Jencks, W. P. (1995). Role of binding energy with coenzyme A in catalysis by 3-oxoacid coenzyme A transferase. *Biochemistry* 34, 11678–11689. doi:10.1021/bi00037a005

45 Yang, W. and Drueckhammer, D. G. (2003). Computational study of the citrate synthase catalyzed deprotonation of acetyl-coenzyme A and fluoroacetyl-coenzyme A: Demonstration of a layered quantum mechanical approach. *J. Phys. Chem. B* 107, 5986–5994. doi:10.1021/jp034717v

CHAPTER 4. PROTON EXCHANGE WITHOUT CONDENSATION IN *ACETOBACTER ACETI* CITRATE SYNTHASE

4.1 Introduction

The citrate synthase (CS) condensation reaction joins the terminal methyl carbon of acetyl-CoA (AcCoA) to the carbonyl carbon of oxaloacetate (OAA). An aspartate serves as the general base and, together with a histidine, stabilizes the resulting AcCoA carbanion/enolate nucleophile (Figure 4.1A). The subsequent citryl-CoA (CitCoA) hydrolysis reaction forms citrate and CoA. As the gateway to central carbon metabolism, CS catalyzes one of the most significant carbon-carbon bond-forming reactions in the biosphere, one that is particularly important to energy harvesting by aerobes. The condensation reaction performed by CS and the mechanistically related malate synthase requires a weak base (a carboxylate) to somehow overcome the substantial kinetic and thermodynamic barriers associated with carbon deprotonation (Gerlt and Gassman, 1993; Gerlt, 2007; Amyes and Richard, 2007) to generate and stabilize a carbanion prior to carbon-carbon bond formation (Clark et al., 1988).Exchange of substrate hydrogen atoms for deuterium atoms, most often provided by bulk D_2O solvent, was the first, and remains the most common, method used to detect transient carbanion intermediates (Rose, 1958). In D_2O solvent, CS catalyzes hydrogen- to-deuterium exchange (HDX) of the

Declaration of collaborative work: Hong Jiang measured the rate of HDX catalyzed by AaCS•OAA by NMR, Sandra Kerfoot measured the rate of HDX by ESI-MS, Charles Constantine made single Trp mutants, and Julie Francois measured inhibition constants of AcCoA analogues. All other biochemical experiments and analysis were done by Jesse Murphy.

terminal methyl protons in AcCoA (Figure 1B) if OAA or an analogue such as D-malate is also present (Marcus and Vennesland, 1958; Bové etal., 1959; Srere, 1967; Efferer, 1965; Myers and Boyer, 1984; Kurz et al., 1997). Exchange is detected only in one methylene of the product citrate, not in free AcCoA, suggesting that proton transfer commits bound substrates to catalysis (Kurz et al., 2000). Active site residues, including several within the pig CS (PCS) binding site for OAA, affect the rate and extent of HDX (Kurz et al., 1995; Kurz et al., 1998). The nonhydrolyzable ketone analogue of AcCoA, dethiaAcCoA (AcMX) has been used to study proton transfer because AcMX can only undergo the condensation reaction. PCS•OAA catalyzes rapid HDX of methyl protons in AcMX or a methylene proton in the poor substrate propionyl- CoA (Kurz et al., 1997). If AcMX enolization is necessary and sufficient for CS•OAA- mediated HDX, the rate-limiting step could be enolization (k_{-H}) itself. However, the rate- limiting step could be the subsequent solvent exchange of the buried, protonated Asp (k_{ex}) (Figure 1C). Protonation (k_H) and deuteration (k_D) are less likely to be rate-limiting, given the instability of carbanion intermediates (Thibblin and Jencks, 1979), and therefore less likely to be associated with a detectable kinetic isotope effect (KIE).

Like PCS, the CS from the thermoacidophilic euryarchaeon *Thermoplasma acidophilum* (TpCS) (Sutherland et al., 1990; Russell et al., 1994; Kurz et al, 2000) is a dimer (type I), with one active site per subunit, each located at the subunit interface. The CS from the Gram-negative bacterium *Acetobacter aceti* (AaCS) is a hexamer (type II CS) comprising three protomers, each of which resembles the type I dimer.

X-ray crystal structures of animal CS (Remington et al., 1982; Wiegand et al., 1984) and diverse additional CS forms depict a high degree of conservation of overall structure and within the active site, despite substantial sequence divergence. Crystal structures of CS ternary complexes containing OAA and the AcCoA enolate analogue carboxymethyldethia-coenzyme A (CMX) reveal virtually superimposable active sites in type I chicken CS and type II AaCS (Usher et al., 1994; Francois et al., 2006). CS forms from all three kingdoms of life appear to use the same chemical mechanism (Kurz, et al., 2000). However, differences in the complete free energy profile for PCS and the partial free energy profile for TpCS indicate that there are differences in on-enzyme equilibria and kinetic barriers for these two most intensively studied CS forms (Kurz et al., 2009).

The purpose of this study is to examine the AaCS condensation reaction to test the hypothesis that it is essentially the same as other CS forms.OAA strongly quenches Trp fluorescence emission, in both type I TpCS and type II AaCS (Kurz et al., 2000; Francois et al., 2006). Quenching is due to the polarized OAA carbonyl, which binds near TpCS Trp348, and it is not observed in CS forms that lack this semiconserved Trp (Kurz et al., 2005). In contrast, the addition of CitCoA transiently *increases* TpCS fluorescence emission intensity (Kurz et al., 2005; Kurz et al., 2009). The condensation reaction can therefore be monitored directly, as a proportional increase in intrinsic Trp fluorescence reports directly on $sp^2 \rightarrow sp^3$ conversion during carbon-carbon bond formation.

Similarly, the addition of AcMX to TpCS•OAA alleviates fluorescence quenching, indicating it undergoes the condensation reaction forming dethiacitryl-CoA (CitMX) (Kurz

et al., 2009). The formation of a stoichiometric TpCS•CitMX complex was confirmed by an X-ray structure of crystals grown in the presence of OAA and AcMX (PDB entry 2r9e; C. Lehmann and Z. Chen, unpublished observations). There is, however, no detectable CitMX accumulation in solution, suggesting that CitMX is bound too tightly to TpCS to dissociate. Furthermore, the extent of HDX in AcMX is superstoichiometric with respect to enzyme concentration. For this to occur, CitMX must undergo the reverse-condensation reaction to re-form OAA and AcMX (Figure 1D). In D_2O, AcMX formed this way can acquire one or more deuterium atoms in the terminal methyl group, depending on whether HDX occurs only during the reverse condensation reaction (i.e., one deuterium per CitMX formed) or may occur during carbanion formation (i.e., multiple deuteria per binding event). HDX can either occur multiple times per AcMX binding event, suggesting a *processive* mechanism of HDX during enolate formation, or HDX could occur once per binding event, suggesting a *distributive* mechanism.

Stopped-flow fluorescence (SFF) studies of the conversion of TpCS•OAA+AcMX to TpCS•CitMX were used to develop a kinetic model consistent with successive AcMX binding and condensation steps (Kurz et al., 2009). This type of analysis was made possible in TpCS because it happens to contain a reporter Trp (Kurz et al., 2000). Pre-steady-state kinetic analysis on TpCS catalyzed condensation shows a primary deuterium KIE with [methyl-d3] AcCoA (Kurz et al., 2009). This finding, together with the million-fold steady-state kinetic impairment of the TpCS-D317A mutant suggested that proton transfer(s) and the Asp general base are involved in the rate-limiting step in the condensation reaction.

Ordinarily, the subsequent hydrolysis reaction is rate-limiting in steady-state turnover by TpCS (Kurz et al., 2000). Additional insight into this might be gleaned from presteady-state studies of the stepwise deuteration of AcMX (Figure 1B). However, the ability of TpCS to form CitMX introduces uncertainty about whether HDX occurs within the ternary complex or during the reverse-condensation reaction that cleaves CitMX (Figure 1D).

In this work, we show that addition of AcMX does not affect OAA-mediated Trp fluorescence quenching, indicating that a binary AaCS•CitMX complex either does not form or does not accumulate to a substantial degree. AcMX nevertheless undergoes rapid HDX catalyzed by AaCS•OAA. Progress curves monitoring the levels of isotopomer intermediates formed during HDX are consistent with a distributive reaction characterized by a single rate constant for all three exchange steps.

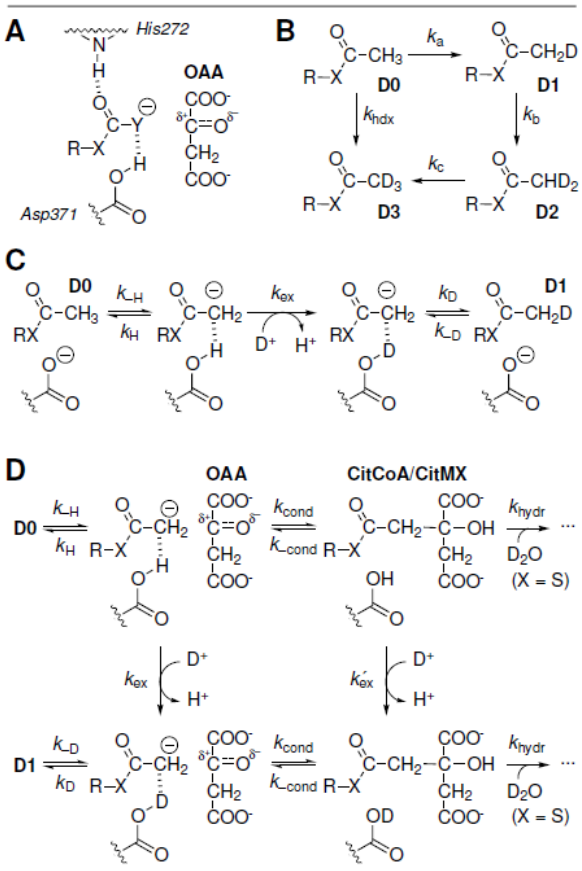

Figure 4.1. Carbanion formation by ternary CS complexes and relationship to HDX of AcCoA analogues. (A) AaCS residues interacting with a putative AcCoA enolate intermediate (X = S and Y = CH_2; R is the remainder of CoA), which undergoes reaction with the highly polarized OAA carbonyl carbon during the condensation reaction. Corresponding TpCS residue numbers are His222 and Asp317. Corresponding PCS residue numbers are His274 and Asp375. AcMX (X = Y = CH_2) is an AcCoA analogue. CMX (X = CH_2; Y = O) is an AcCoA enolate analogue. (B) Site exchange rate constants for CSOAA-catalyzed AcCoA or AcMX methyl HDX (k_{hdx}) are subject to geometric selection effects of 3:2:1:0 for isotopomers **D0**–**D3**. (C) HDX without condensation. Rate constants for proton abstraction (k_{-H}) and addition (k_H), the corresponding deuterium rates (k_{-D} and k_D), and solvent washout (k_{ex}) are assumed to have similar values for **D0**–**D3**. **D1** can undergo either proton abstraction (k_H), which may result in **D2** formation, or futile deuteron abstraction (k_{-D}). (D) HDX with condensation. CS OAA complexes that allow reversible condensation of AcCoA or AcMX with OAA have the potential to take up a deuteron during the reverse condensation reaction (k_{-cond}) following solvent washout (k'_{ex}), in addition to the sequence illustrated in panel C (left hand sequence). Only AcCoA (X = S) is a substrate for the subsequent hydrolysis reaction that forms citrate (k_{hydr}).

4.2 Materials and Methods

Materials.

All chemicals were obtained from Sigma-Aldrich or Fisher in the highest grade available and were used as received. AcMX and CMX were synthesized as previously described (Francois et al., 2006). QuikChange mutagenesis kits were obtained from Agilent (Santa Clara, CA).

Synthesis of AcCoA-h3 and AcCoA-d3.

AcCoA-d3, where the terminal methyl group is fully deuterated, was synthesized as previously described (Gauthier et al., 2013). AcCoA-h3 was synthesized in parallel so that it would contain the same contaminants present in AcCoA-d3. CoA (25 mg, 0.033 mmol) was dissolved in cold water (2 mL in a 15 mL conical tube). Either acetic anhydride or d_6-acetic anhydride (100 µL, 23 mmol) was added in 20 µL increments, with each addition followed by immediate mixing and a 30 min incubation in an ice-water bath. The pH was maintained near neutrality by the addition of saturated sodium bicarbonate and monitored throughout the reaction by spotting small aliquots onto pH test strips (Hydrion, New York). The progress of each reaction was monitored by removing aliquots (5 µL) and quantifying any remaining unreacted CoA at 412 nm $\Delta\varepsilon = 14.1\ mM^{-1}\ cm^{-1}$ after reduction of the thiol reagent DTNB (Collier, 1973). When the CoA concentration was steady for 30 min, the reaction was quenched by the addition of 98% formic acid (200 µL, 5.3 mmol). Each reaction mixture was lyophilized to dryness. Solids were re-suspended in

5 mM (5 mL) HCl, centrifuged at 16,000 g for 10 min, and the full volume was injected onto an Agilent 110 series HPLC equipped with a Luna 5 µm C18(2) 250 × 21.2 mm column (Phenomenex; Torrance, CA) equilibrated in water containing 0.1% (v/v) trifluoroacetic acid (TFA) and 2.0% (v/v) methanol. The column was developed in a linear gradient of 2% to 90% methanol in 0.1% TFA with absorbance monitoring at 260 nm. The peak corresponding to AcCoA was collected, frozen, lyophilized to dryness, and resuspended in 5 mM HCl (0.1 mL).

Synthesis of AcMX-d3.

AcMX (250 nmol) was incubated in 250 µL deuterated SCACT buffer (50 mM potassium phosphate, pD = 8.0, 100 mM KCl in 99.9 % D_2O (Cambridge isotope labs, Andover, MA)) containing 0.6 mM OAA (from a 10 mM stock prepared in 1× deuterated SCACT buffer), and 4 µM TpCS (from a concentrated stock prepared in 1× deuterated SCACT buffer) at 22 ˚C in a 1.5 mL microfuge tube. After 15 h, the reaction was quenched by the addition of 98% formic acid (30 µL, 0.8 mmol) and solids, including denatured enzyme, were removed by centrifugation at 16,000 g for 10 min in microfuge tubes. The reaction mixture was applied to a C18 Sep Pak (Waters) cartridge that had been washed with methanol (10 mL) and then washed and equilibrated in 0.1% formic acid (10 mL). The cartridge was washed with 0.1% formic acid (10 mL) and the sample was eluted with methanol (3 mL). The sample was dried using a vacuum concentrator (Eppendorf; Hauppauge, New York) and resuspended in 5 mM HCl (0.1 mL).

General analytical methods.

Protein masses were determined by electrospray-ionization mass spectrometry (ESI-MS) by the staff of the Washington University Mass Spectrometry Resource. Absorbance measurements were recorded using a Varian Cary 100 Bio UV-visible spectrophotometer thermostated at 25 °C. ^{1}H NMR spectra were obtained at 500 MHz using a Varian Unity Inova 500 spectrometer equipped with a 5 mm Varian reverse probe. The pL (pH or pD) was determined using a glass electrode. pD was calculated by adding 0.4 to the displayed pH value. (Lumry et al., 1951). All curve fitting was performed using gnuplot 4.4, Origin 8.6 (OriginLab; Northampton, MA), or DynaFit (Kuzmic, 1996).

Protein expression, purification, and analysis.

Plasmids pJK136 and pJK225 encode AaCS and AaCS with the octapeptide LEHHHHHH appended to the C-terminus (AaCSH6), respectively (Francois et al., 2006). QuikChange mutagenesis of pJK225 with oligodeoxynucleotides 898 and 899 (sequences given in Supporting information, Table S1) furnished plasmid pJK241 (AaCSH6-W404F). QuikChange mutagenesis of pJK225 with oligodeoxynucleotides 959 and 960 furnished plasmid pJK708 (AaCSH6-W400F).

AaCS^{dye}, a wild-type AaCS isolated by dye-ligand affinity, and AaCSH6 were produced as described (Francois et al., 2006). AaCSH6 mutants were overproduced in BL21(DE3) cells transformed with a suitable plasmid and purified using the procedure reported for AaCSH6. Protein concentrations were measured using the Bradford assay (Bio-Rad) with bovine serum albumin used as the standard (Bradford, 1976).

Inhibition patterns and constants were determined using $AaCS^{dye}$ and assay method B (Francois et al., 2006), modified to use a fixed concentration of 0.1 mM OAA (AcCoA varied from ≤9 to ≥143 μM) and by the addition of candidate inhibitors.

Kinetic methods and substrate concentrations.

Concentrations of AcCoA and AcMX were determined spectrophotometrically assuming an extinction coefficient of 16.4 mM^{-1} cm^{-1} at 260 nm (Dawson, 1993). Citrate synthase activity in H_2O and D_2O with AcCoA-h3 or AcCoA-d3 was determined in reaction mixtures (final volume 0.7 mL) containing 50 mM potassium phosphate pL = 8.0, 100 mM potassium chloride, 400 μM OAA, 300 μM DTNB, varied AcCoA-h3 or AcCoA-d3, and either AaCSH6 (0.076 μg, 0.017 units) or TpCSH6 (0.55 μg, 0.007 units) added last to initiate the reaction (Srere, 1969). A unit is defined as the amount of enzyme required to produce 1 μmol of product per min.

Fluorescence measurements.

Fluorescence measurements were recorded at 25 °C using a Cary Eclipse fluorescence spectrophotometer (Agilent; Santa Clara, CA) or a Fluoromax-3 (Horiba Jobin Yvon; Edison, NJ) (slit widths of 5 nm, except where noted) with continuous stirring. Fluorescence emission spectra were corrected for dilution and for inner filter effects using *N*-acetyltryptophanamide.

AaCS attached to a C-terminal fluorescein (Fl) tag (AaCSFl) was prepared by expressed protein ligation (Supporting Information). The mole fraction of AaCS labelled with fluorescein (Fl), P_{Fl}, was determined by a modified literature method using

Equation1. The AaCS extinction coefficient (ε_{280} = 49,740 M^{-1} cm^{-1}) measured in buffer PK9 (50 mM potassium phosphate, pH 9.0, 100 mM KCl) was comparable to a value (44,760 M^{-1} cm^{-1}) computed assuming reduced cysteines (Gill and von Hippel, 1989). The Fl extinction coefficient ε^{Fl} at pH 9 was 74,000 M^{-1} cm^{-1} (Molecular Probes, Inc).

$$P_{Fl} = \frac{[AaCSFl]}{[AaCS]+[AaCSFl]} = \frac{A_{494}}{\varepsilon_{494}^{Fl}} \frac{\varepsilon_{280}^{AaCS}}{A_{280}-kA_{494}} \quad (4.1)$$

Förster resonance energy transfer (FRET) efficiency (*E*) was computed using Equation 2, where f_{AaCS} and f_{AaCSFl} represent the fluorescence of a 1 M solution of AaCS or AaCSFl, respectively.

$$E = 1 - \frac{I_{DA}}{I_D} = 1 - [\frac{f_{AaCSFl} - f_{AaCS}(1-P_{Fl}}{P_{Fl} f_{AaCS}}] \quad (4.2)$$

Using the Förster radius (R_0) of 27 Å for Trp (donor) and fluorescein (acceptor) (Gill and von Hippel, 1989), the average donor-acceptor distance ($\bar{r}_{DA}$) was computed using Equation 3 (Griep and McHenry, 1990).

$$\bar{r}_{DA} = R_0\sqrt{\frac{1}{E} - 1} \qquad (4.3)$$

Stopped-flow fluorescence spectroscopy.

Transient kinetic experiments were performed on either a SX.18-MV stopped-flow (SF) apparatus (Applied Photophysics, Leatherhead, U.K.) with a cutoff filter (> 305 nm) and an instrumental dead time of 1.2 ms or a SF-61 DX2 SF apparatus (Hi-Tech; TgK, Bradford-on-Avon, UK) with a cutoff filter >320 nm and an instrumental dead time of 2 ms. Intrinsic protein fluorescence was excited at 296 nm. OAA binding interactions were initiated at 25 °C by mixing equal volumes of AaCS + varied OAA concentration. AcMX binding interactions were initiated at 25° by mixing equal volumes of AaCS•OAA (equilibrated in either H_2O or D_2O) and either AcMX or AcMX-d3 in H_2O or D_2O, respectively. For AcMX or AcMX-d3 binding interactions each syringe contained the same concentration of OAA. Parallel control experiments lacking enzyme or ligands were also performed. The instantaneous post-mixing reaction mixture contained 50 mM potassium phosphate, pL = 8, 100 mM KCl, 0.1 or 0.2 mM OAA, 1 or 5 µM AaCSH6, variable AcMX/ AcMX-d3, or AcCoA-h3/AcCoA-d3. Rate constants were obtained by fitting progress curves to Equation 4.4.

$$F(t) = F_\infty + F_0(1 - e^{-k_{obs}t}) \qquad (4.4)$$

$$E + L \underset{}{\overset{K_{d1}}{\rightleftharpoons}} E{\bullet}L \underset{k_{-2}}{\overset{k_2}{\rightleftharpoons}} (E{\bullet}L)' \quad (4.5)$$

A reversible two-step binding model with E = AaCS•OAA and L = AcMX (Equation 4.5) is expected to show a hyperbolic dependence of the observed rate (k_{obs}) on [L] (Equation 4.6)

$$k_{obs} = \frac{k_2[L]}{[L]+K_{d1}} + k_{-2} \quad (4.6)$$

NMR spectroscopy.

HDX was monitored by NMR recorded at 500 MHz as described (Kurz et al., 1997), except that spectra were acquired every 8.4 min. The reaction mixture contained 20.5 nM AaCS (subunit concentration), 1.0 mM OAA, 0.987 mM AcMX, and 50 mM potassium phosphate, pD 7.9 at 25 °C. Peak areas recorded at different times, $I(t)$, were subjected to baseline correction and referenced to the peak area (corrected for dilution) measured prior to the addition of enzyme, I_0. The observed HDX rate k_{obs} was determined by a fit of the data to Equation 7. The relative final peak area, I_∞/I_0, was set to 19% to account for any unreactive fraction and the background due to baseline integration.

$$\frac{I(t)}{I_0} = (1 - I_\infty)e^{-k_{obs}t} + I_\infty \quad (4.7)$$

$$k_{HDX} = 3\frac{[AcMX]}{[AaCS{\bullet}\mathrm{OAA}]}k_{obs} \quad (4.8)$$

The k_{obs} value was converted to a specific rate using Equation 4.8 as previously described (Kurz et al., 1997).

NMR spectra of AcMX were examined for evidence of nonenzymatic HDX using data recorded in the same solution conditions without enzyme. A peak with δ = 8.55 ppm and T_1 = 1.91 s (in H_2O), assigned to the adenine H8 proton, was observed to decrease in intensity over 2900 min with a linear slope of $(-7.09 \pm 0.09) \times 10^{-5}$ min^{-1}. A peak with δ = 8.51 ppm appeared at the same rate. A peak with δ = 0.73 ppm and T_1 = 0.48 s (in H_2O), assigned to a pantoate methyl group, appeared to exchange for one with δ = 0.77 ppm, each with a linear slope of $|5.09 \pm 0.03| \times 10^{-5}$ min^{-1}.

Mass spectrometry.

CS-mediated AcMX HDX reactions were monitored by ESI-MS performed in positive ion mode on a Finnegan LCQ Classic with sheath gas flow rate 20, auxiliary gas flow rate 5, spray voltage 4 keV, capillary temperature 200 °C, capillary voltage 45 V, and tube lens offset 10 V. The sample was directly infused at 5 µL min^{-1} using a syringe pump. An exchange reaction equilibrated at 23 °C contained (final volume of 0.76 mL) 50 mM ammonium formate, pD 7.9, 1 mM OAA, 0.9 mM AcMX, and 20 nM AaCS. HDX was initiated by the addition of enzyme. At intervals ranging from 5–10 min, an aliquot (1 µL) was diluted into quench solution (249 µL of 50% acetonitrile in water adjusted to pH 2.5 with formic acid), vortexed briefly, and then directly infused for 5 min of data accumulation. The data were acquired in zoom scan mode centered at *m*/*z* 795 with a 10 amu window. Scans were summed and peaks were picked using a homebuilt algorithm

(D. Rempel, unpublished program). Picked peak intensities were corrected for isotopic abundances in the AcMX stock solution in D_2O. This correction was necessary due to slow exchange of a single proton within the adenosine nucleotide. The mole fraction (χ) of each AcMX terminal methyl isotopomer (**D0** – **D3**) was obtained by normalizing each peak area to the sum of corrected peak areas at M, M+1, M+2, and M+3.

Analysis of exchange kinetics.

HDX in the terminal methyl group of AcMX was modeled as a sequence of three sequential, irreversible, first-order reactions (Figure 4.1) described by four differential equations (Equations 4.9-12).

$$\frac{\partial \chi^{D0}}{\partial_t} = -k_a \chi^{D0} t \quad (4.9)$$

$$\frac{\partial \chi^{D1}}{\partial_t} = k_a \chi^{D0} t - k_b \chi^{D1} t \quad (4.10)$$

$$\frac{\partial \chi^{D2}}{\partial_t} = k_b \chi^{D1} t - k_c \chi^{D2} t \quad (4.11)$$

$$\frac{\partial \chi^{D3}}{\partial_t} = k_c \chi^{D2} t \quad (4.12)$$

An integrated rate expression was obtained for each isotopomer using the boundary condition $\chi_0^{D0} = 1$ (Equations 4.13-16).

$$\chi^{D0} = e^{-k_a t} \quad (4.13)$$

$$\chi^{D1} = \frac{k_a}{k_b - k_a}[e^{-k_a t} - e^{-k_b t}] \quad (4.14)$$

$$\chi^{D2} = k_a k_b [\frac{e^{-k_a t}}{(k_a - k_c)(k_a - k_b)} - \frac{e^{-k_b t}}{(k_b - k_c)(k_a - k_b)} + \frac{e^{-k_c t}}{(k_b - k_c)(k_a - k_c)}] \quad (4.15)$$

$$\chi^{D3} = [1 - \frac{k_b k_c e^{-k_a t}}{(k_a - k_c)(k_a - k_b)} + \frac{k_a k_c e^{-k_b t}}{(k_b - k_c)(k_a - k_b)} + \frac{k_a k_b e^{-k_c t}}{(k_b - k_c)(k_a - k_c)}] \quad (4.16)$$

Equation 13 was modified to account for the contribution of a molecule that is isobaric with D0, χ_{∞}^{D0}, but does not undergo reaction during the experiment (Equation 4.17).

$$\chi^{D0} = e^{-k_a t} + \chi_{\infty}^{D0} \quad (4.17)$$

If the observed rate of HDX is the same for all three HDX reactions, subject only to a geometric factor that scales the observed rate constant to the average rate constant for the removal of a proton (i.e, $k_a = 3k_{\bar{c}}, k_b = 2k_{\bar{c}}, k_c = k_{\bar{c}}$), the integrated rate expressions simplify to Equations 18-21.

$$\chi^{D0} = e^{-3k_{\bar{c}} t} + \chi_{\infty}^{D0} \quad (4.18)$$

$$\chi^{D1} = 3e^{-2k_{\bar{c}} t} - 3e^{-3k_{\bar{c}} t} \quad (4.19)$$

$$\chi^{D2} = 3e^{-k_{\bar{c}} t} - 6e^{-2k_{\bar{c}} t} + 3e^{-3k_{\bar{c}} t} \quad (4.20)$$

$$\chi^{D3} = 1 - 3e^{-k_{\bar{c}} t} - 3e^{-2k_{\bar{c}} t} + e^{-3k_{\bar{c}} t} \quad (4.21)$$

HDX progress curves were fit globally to both sets of four integrated rate expressions.

4.3 Results

OAA primarily quenches AaCS Trp400 fluorescence.

The addition of OAA strongly quenches TpCS fluorescence (Kurz et al., 2000). TpCS Trp348, a buried and immobile residue that is about 9 Å from the OAA carbonyl, is the primary fluorescence emitter and is most sensitive to OAA binding (Kurz et al., 2005). AaCS fluorescence is similarly quenched by OAA, albeit to a lesser degree (Francois et al., 2006). Of the four present in AaCS and TpCS, only one (AaCS Trp400) is conserved in both. AaCS Trp400 adopts the same orientation, relative to OAA, as TpCS Trp348 (Figure 2). A second Trp, AaCS Trp404, is farther from OAA than Trp400 but is nearly equidistant to two OAA binding sites and might therefore undergo enhanced quenching by OAA.

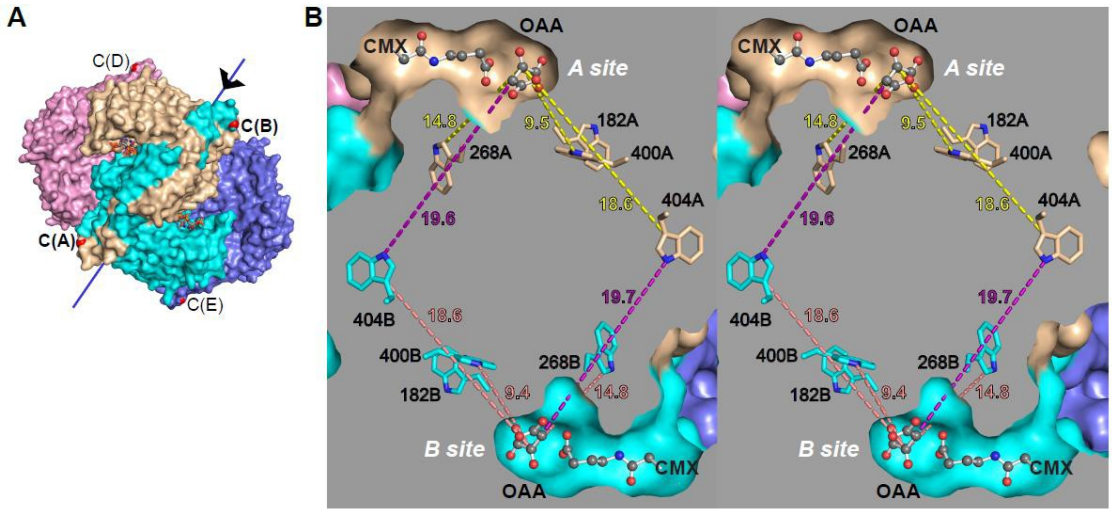

Figure 4.2. Structure of AaCS•OAA•CMX (PDB entry 2H12). (A) AaCS hexamer surface. The view is along the pseudo-twofold axis (center) that relates the subunits in each dimeric protomer (subunit A, light brown; subunit B, cyan). A perpendicular pseudo-threefold axis (blue rod with triangular symbol, shown in the plane of the page) defines the hexameric assembly. The hexameric interface is much smaller than the extensive dimeric interface (Nguyen et al., 2001). Red spheres indicate the locations of the C-terminal residue (Arg436) in four subunits; the last 15 residues in each subunit are draped over the N-terminal domain of the partner subunit. Part of the AcCoA analogue CMX (stick rendering) is visible in both active sites of the AB protomer. (B) Walleyed stereodiagram depicting the interior of the AaCS dimer. The interior of the protein is light gray; the exterior surfaces have the same colors as panel A. Active site ligands are shown in ball-and-istick rendering; CMX is truncated at the equivalent of CoA C600 PMID 9047322. The Trp residues are shown in stick rendering with carbon atoms colored by subunit. Dotted lines are labeled with the distance (in Å, for separations ≤ 20 Å) between each OAA carbonyl carbon and the closest indole carbon or nitrogen atom; intrasubunit contacts are yellow (chain A) or salmon (chain B) and intersubunit contacts are purple. The closest contact to Trp268 Cg is slightly shorter than the illustrated contact to Cd 1 (14.7 Å and 14.8 Å, respectively), but would have been obscured behind the purple dotted line. Trp182 is 27 Å from OAA carbonyls in the same protomer, but is the closest to an OAA carbonyl in an adjacent protomer (37 Å). Dotted lines and ligand models extend beyond the near clipping plane used to generate the interior section.

To assess the relative contribution of each Trp to fluorescence emission spectra, and ligand-dependent changes in those spectra, AaCS forms lacking either Trp400 or Trp404 were isolated by the method developed for AaCSH6 and found to retain

substantial enzymatic activity (Table 4.1). The mutant containing Trp400, AaCSH6-W404F, was analyzed by ESI-MS.

Two main forms were observed, one with *m/z* 49018 (49020.3 expected for [M-Met+H]) and one with *m/z* 48958 (48960.3 expected for [M-Met- Gdn+H]). The second peak is proposed to be due to gas-phase loss of a guanidinium group, as previously observed with AaCS forms (Francois et al., 2006).

Table 4.1. Selected kinetic and binding constants for AaCS forms.

parameter	AaCSH6	AaCSH6-W404F	AaCSH6-W400F	AaCSFl
k_{cat} (s^{-1})	95	66	65	78
K_{M}^{AcCoA} (μM)	29	31.7	87	52
K_{d}^{OAA} (μM)	14.2[b]	19.6	NA[c]	25
K_{d}^{AcMX} (μM)	6.7[d]	ND[e]	ND[e]	5.1[f]/ 8.2[g]

[a] Data from Ref 17
[b] Previously reported to be 21 μM (17).
[c] NA, not applicable. No protein fluorescence change was noted upon the addition of OAA (Figure 3C). An earlier experiment with AaCSH5-W400F, i.e., a mutant lacking one residue in the affinity tag, gave a fluorescence decrease associated with an OAA K_d = 180 μM (data not shown).
[d] Based on a titration with AcMX-d3 in D_2O-containing buffer.
[e] ND, not done. [f]ultraviolet [g]visible

The fluorescence emission spectrum of AaCSH6-W404F was quenched by the addition of OAA, to an extent similar to AaCSH6 (Figure 3B). In contrast, AaCSH6-W400F showed no quenching by OAA (Figure 3C). This indicates that AaCS Trp400 fluorescence is the only one sensitive to OAA binding. Trp404 may, however, contribute more than

Trp400 to the basal fluorescence emission intensity of AaCS. The OAA binding affinities for AaCS and AaCS W404F were determined by fluorescence titration. The data were fit to a simple hyperbolic isotherm (Figure 3D) with binding affinities listed in Table 4.1.

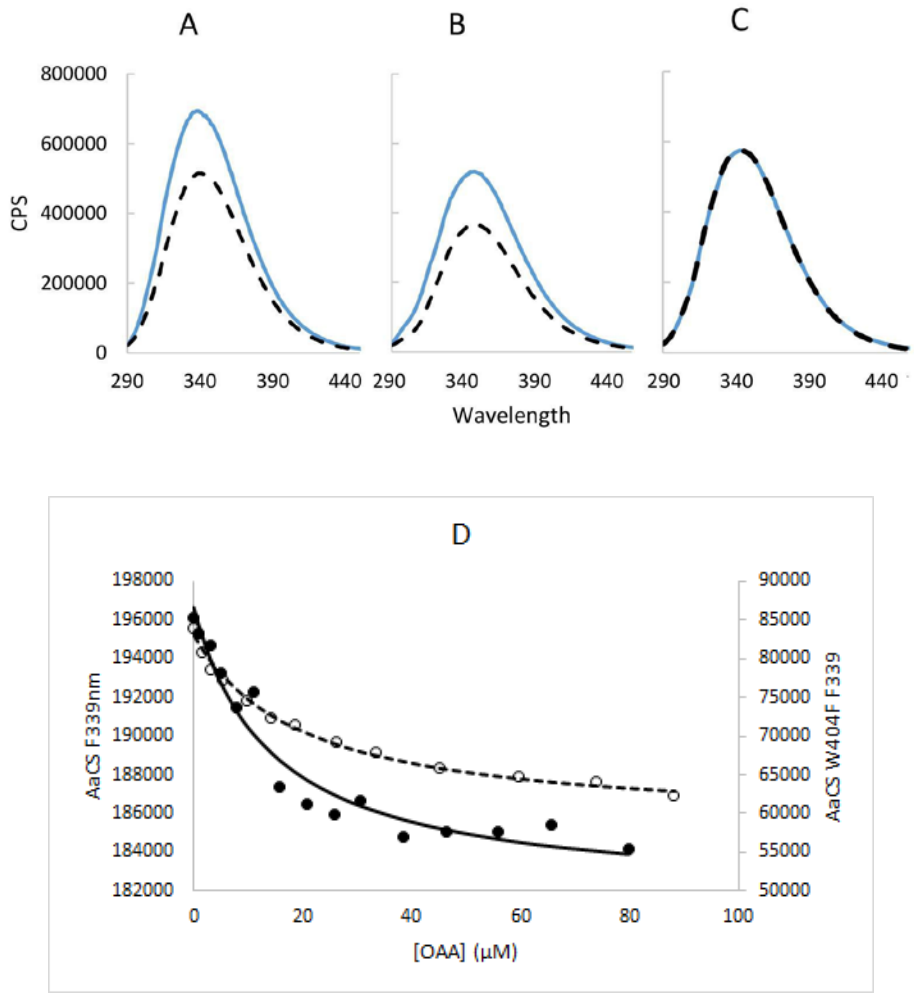

Figure 4.3. Effect of OAA on AaCS fluorescence emission. In panels A–C, the solid line is the fluorescence emission spectra of unbound AaCS or single Trp mutants and the dashed line is recorded in the presence of 100 μM OAA. (A) AaCSH6. (B) AaCSH6-W404F (contains Trp400). (C) AaCSH5-W400F (contains Trp404). (D) OAA titrations of AaCSH6, filled circles fit is solid black line; AaCSH6-W404F, open circles fit is dashed line. OAA binding affinities from these data are listed in Table 4.1.

A preliminary stopped-flow fluorescence (SFF) study of AaCS (0.4 µM subunit concentration, post-mixing) binding to OAA (4–100 µM) at 25 °C and pH 8 showed very fast fluorescence changes, with every observed rate k_{obs} >650 s^{-1} (data not shown). OAA binding to AaCS forms appears to be very rapid.

Competitive inhibition of AaCS•OAA by AcCoA analogues.

AcCoA or AcCoA enolate analogues CoA, AcMX, carboxymethyl-coenzyme A (CMCoA), and CMX are progressively potent, competitive inhibitors of PCS (Bayer et al., 1981; Martin et al., 1994)). These compounds are progressively potent, reversible inhibitors of AaCS and all are competitive with respect to AcCoA (Figure 4.4). PCS has $K_i^{AcMX} \approx K_m^{AcCoA}$(Martin et a., 1994). AcMX was a more potent inhibitor of AaCS in both absolute and relative terms: $K_i^{AcMX}$was ten times smaller than K_m^{AcCoA}(table 4.2).

Table 4.2: Inhibition of AaCS by AcCoA analogues.

	K_i (μM)	
Inhibitor	AcCoA varied[a]	OAA varied[b]
CoA	31 ± 3	~120
AcMX	2.8 ± 0.2	~130
CMCoA[c]	0.30 ± 0.04	ND[d]
CMX	0.047 ± 0.007	ND[d]

[a] Competitive inhibition pattern (Figure 4). Determined at pH 8.0 and 25 °C with 25 mM OAA (5 × K_M).
[b] Uncompetitive inhibition pattern (data not shown). Determined at pH 8.0 and 25 °C with 150 mM AcCoA (5 × K_M).
[c] A slight time-dependence of inhibition was noted (Charles Z. Constantine, data not shown). The true K_i may be smaller than the stated value.
[d] ND, not determined.

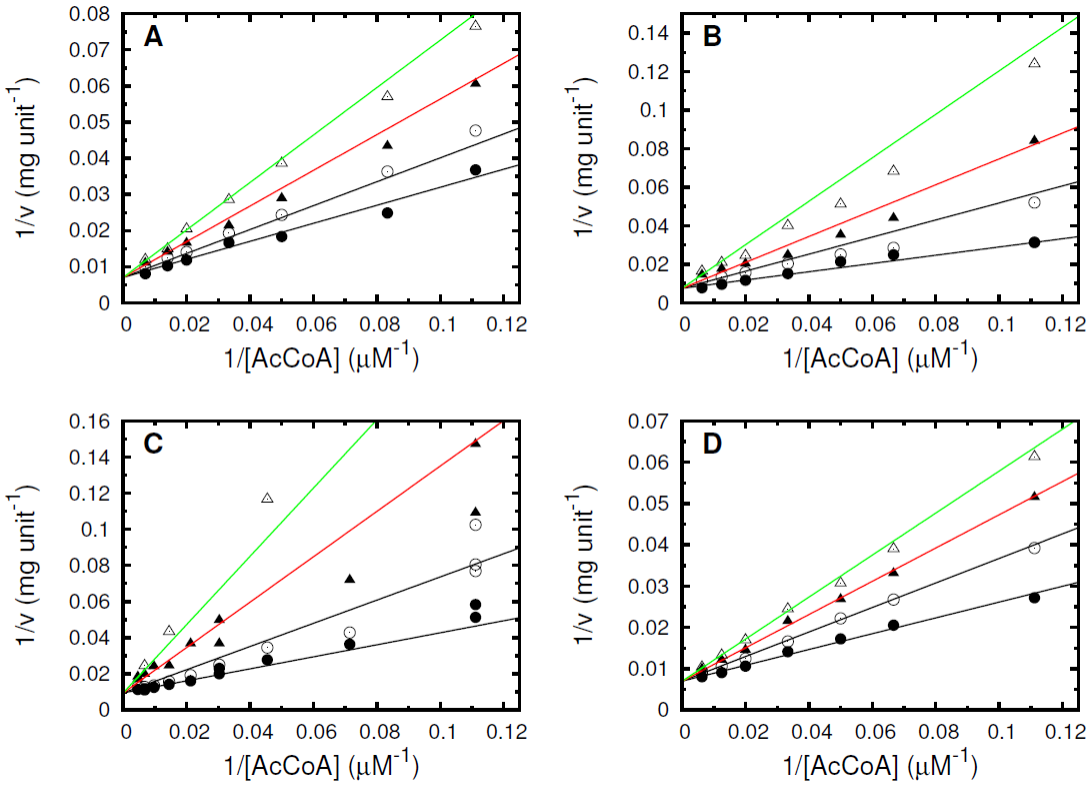

Figure 4.4. Competitive inhibition of AaCS. The line shown at each inhibitor concentration was computed from parameters obtained from a global fit of data obtained at all inhibitor concentrations to a competitive inhibition model. While the fitting was performed using concentration and velocity values, it is shown as a Lineweaver-Burk plot to highlight agreement of the model to the transformed data points. (A) CoA inhibition. The symbols indicate velocity data collected at 0 (filled circles), 10 (open circles), 30 (filled triangles), or 50 μM inhibitor (open triangles). (B) AcMX inhibition. The symbols indicate velocity data collected at 0 (filled circles), 1.55 (open circles), 3.1 (filled triangles), or 4.65 μM inhibitor (open triangles). (C) CMCoA inhibition. The symbols indicate velocity data collected at 0 (filled circles), 0.278 (open circles), 0.83 (filled triangles), or 1.4 μM inhibitor (open triangles). (D) CMX inhibition. The symbols indicate velocity data collected at 0 (filled circles), 0.05 (open circles), 0.1 (filled triangles), or 0.2 μM inhibitor (open triangles).

AaCS•OAA binds AcMX without condensation: fluorescence titrations.

The addition of AcMX to TpCS•OAA eliminates most of the fluorescence quenching due to OAA (18) . AcMX is the only AcCoA analogue associated with this "dequenching" phenomenon: formation converts the OAA carbonyl carbon to a non-quenching sp^3 center (Kurz et al., 2009). In contrast, the addition of AcMX had little effect on fluorescence emission spectra (Figure 4.5, crosses). Since OAA appears to quench AaCS fluorescence by the same mechanism as TpCS fluorescence, AcMX is not converted to CitMX by AaCS•OAA. However, addition of deuterated AcMX (AcMX-d3) to AaCS•OAA in D_2O does cause a decrease in fluorescence that appears to saturate. The data were fit to a simple hyperbolic binding isotherm with a K_d value of 6.7 ± 1.5 μM (Figure 4.6 and table 4.1) which is in good agreement with the AaCSFl binding studies (Figure 4.5).

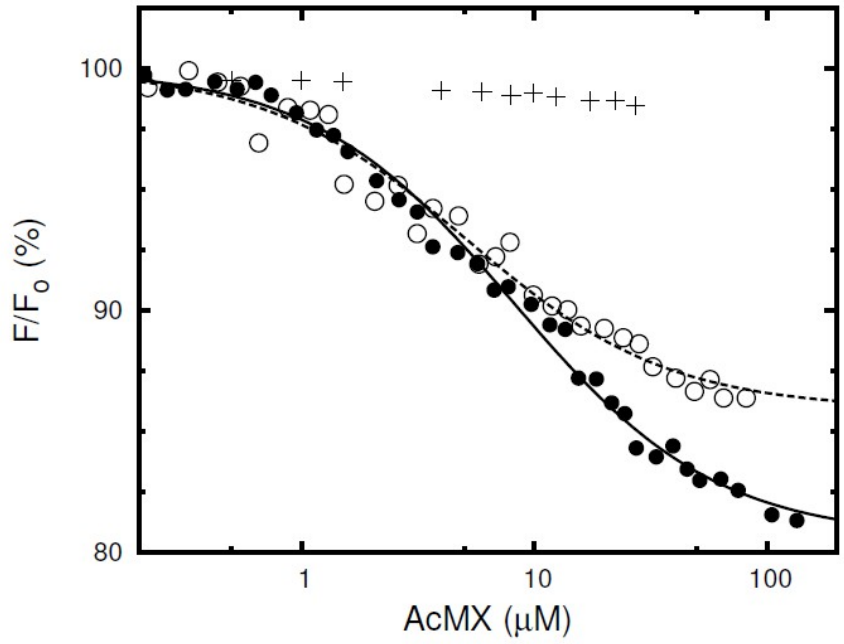

Figure 4.5. Fluorescence detection of AcMX binding to AaCSFl•OAA. All points are derived from fluorescence emission intensities recorded in 50 mM potassium phosphate, pH 8, 100 mM KCl, and 120 μM OAA at 25 °C after 3 min of equilibration at the indicated [AcMX]. Spectra have been corrected for dilution and inner filter effects due to OAA. Crosses, ultraviolet titration of AaCS•OAA (1 mM subunits; excitation: 296 nm; emission: 346 nm). The small fluorescence changes were not fit to a binding isotherm. Open circles, ultraviolet titration of AaCSFl•OAA (1.18 μM subunits; excitation: 295 nm; emission: 346 nm). Dotted line, fit of the fluorescence decrease to Equation 4 (fitted parameters given are in Table 4.1). Filled circles, visible titration of AaCSFl•OAA (0.7484 mM subunits; excitation: 498 nm; emission: 524 nm). Solid line, fit of the fluorescence decrease to Equation 4 (fitted parameters are given in Table 4.1).

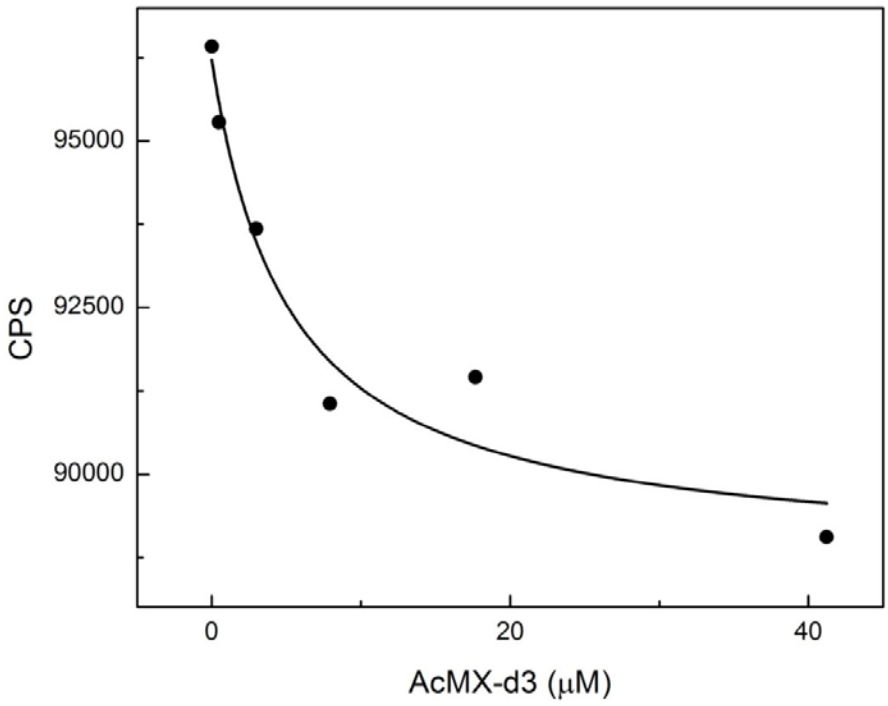

Figure 4.6. Detection of AcMX-d3 binding to AaCS•OAA in D_2O.All points are derived from fluorescence emission intensities recorded in 50 mM potassium phosphate, pH 8, 100 mM KCl, and 100 μM OAA at 25 °C after 3 min of equilibration at the indicated [AcMX]. Spectra have been corrected for dilution and inner filter effects due to OAA.

To facilitate studies of AcMX binding to AaCS•OAA in H_2O, expressed protein ligation (Appendix) was used to fuse a dipeptide containing the fluorescent reporter group 6-carboxyfluorescein (Fl-tag) to the C-terminus of AaCS (AaCSFl). AaCS and AaCSFl had similar enzymatic activity (Table 4.1), OAA affinity (Table 4.1, Figure A1), and indistinguishable mobility on SDS-PAGE gels (not shown). FRET efficiencies of various AaCSFl complexes were determined (Table A2). ESI-MS indicated an approximately 1:1 ratio of AaCS (observed *m*/*z* 47932; 47933.2 expected) to AaCSFl (observed *m*/*z* 48436; 48436.7 expected). Absorbance spectra (Figure A2) were used to compute P_{Fl} = 0.55 ± 0.02, where the standard deviation is based on five replicate preparations. These data

were consistent with an average composition of three Fl per AaCS hexamer, or about one Fl per AaCS protomer.

The addition of AcMX to AaCSFl•OAA in H_2O led to a progressive decrease in fluorescence emission, with either ultraviolet or visible excitation (Figure 4.5B and 4.5C). Titration data were fit by a simple hyperbolic binding isotherm (Table 4.1). Neither transition corresponds to dequenching, since the change in the ultraviolet region has the opposite sign and controls demonstrate that the visible fluorophore would not be effectively quenched by OAA. The fluorescence decreases can be attributed to changes in the fluorophore environment that are induced by AcMX binding, most likely as a consequence of Fl-tag interacting with the partner subunit. AaCS conformational changes observed by peptide HDX are consistent with this interpretation (S. A. Kerfoot, unpublished observations).

AcMX HDX catalyzed by AaCS•OAA: NMR analysis.

Binding of AcMX to AaCS•OAA does not induce the "dequenching" phenomenon observed in TpCS suggesting condensation does not occur to a significant extent. A direct test for AcMX enolization by AaCS•OAA is the observation of HDX in the terminal methyl groups. To prepare for this experiment, the rate of AcCoA dependent turnover in D_2O was determined: k_{cat} = 102 s^{-1} at pD 7.9 appears to have a slightly larger solvent isotope effect ($^{D2O}k_{cat}$ = 1.3 at pL= 8.0) than other CS forms.

^{1}H NMR was then used to monitor HDX as a decrease in the area of the signal corresponding to the terminal methyl protons. A single-exponential fit gave an average rate constant k_{HDX} = 18.8 ± 0.2 s^{-1} (Figure 4.7). AaCS•OAA catalyzes AcMX HDX, albeit at a substantially lower rate than steady-state AcCoA turnover under the same conditions.

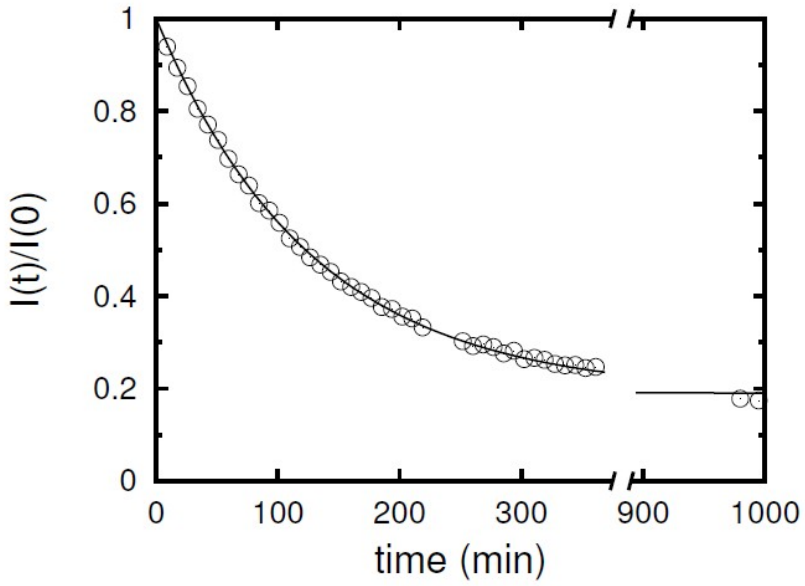

Figure 4.7. AcMX HDX progress curve monitored by ^{1}H NMR at 25 °C. The solid line is a single exponential fit to the data with an observed decay rate v = (7.84 ± 0.08) x 10^{-3} min^{-1}.

NMR analysis shows convergence to a nonzero value (I_∞) that is due to an unreactive fraction with the same methyl chemical shift (**D0**$_\infty$), as well as the background due to baseline integration. HPLC analysis of AcMX shows two peaks, with a 5:1 area ratio (Figure A3). These correspond to AcMX and iso-AcMX, respectively, where iso-AcMX is the 2'-phospho isomer of AcMX (Burns et al., 2005). The unreactive fraction **D0**$_\infty$ may be iso-AcMX, which would suggest it is not accepted by AaCS•OAA as an HDX substrate.

AcMX HDX catalyzed by AaCS•OAA: ESI-MS analysis.

ESI-MS allowed quantitation of individual AcMX isotopomers (Figure 4.8) and the construction of a progress curve for HDX at saturating levels of AcMX (Figure 4.9). Sequential formation of each isotopomer was observed, consistent with a distributive HDX model. A small amount of a species with the same mass as **D0** was not accepted by as an HDX substrate during the period examined. As with the NMR experiments, this unreactive species (**D0**$_\infty$) was presumed to be iso-AcMX. The mole fraction of the unreactive species (χ^{D0}) was fixed at 9% during global fits of progress curves.

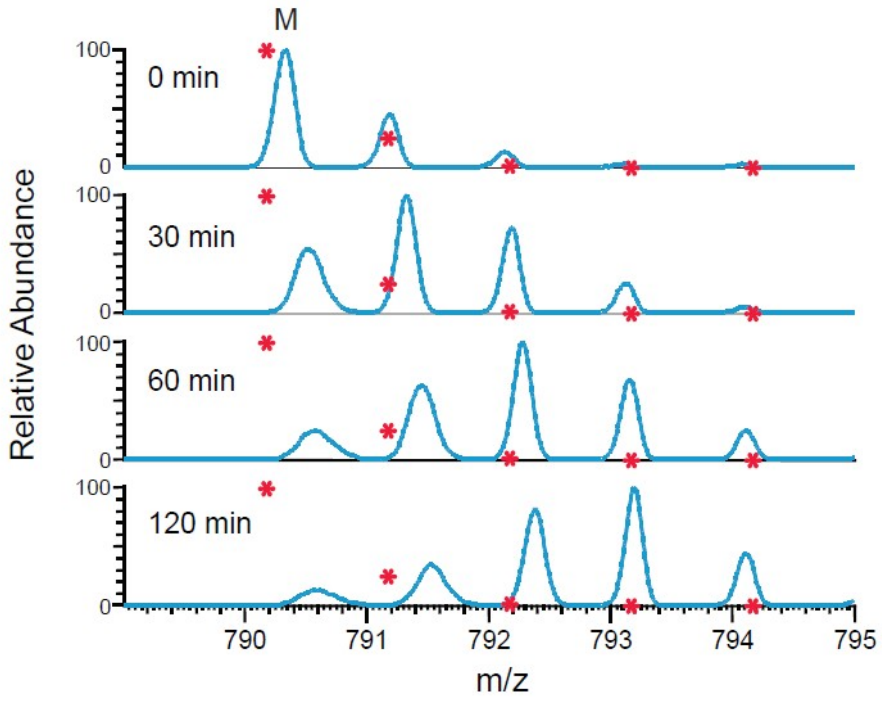

Figure 4.8. AcMX HDX monitored by ESI-MS. The blue lines are experimental spectra recorded after the indicated HDX period. The red symbols in each panel indicate the expected locations and relative peak heights for AcMX at natural isotopic abundance ($C_{24}H_{40}N_7O_{17}P_3$: expect peaks at *m*/*z* 790.2 – 795.2 with relative abundances of 100%, 29.7%, 7.7%, 1.4%, and 0.2%).

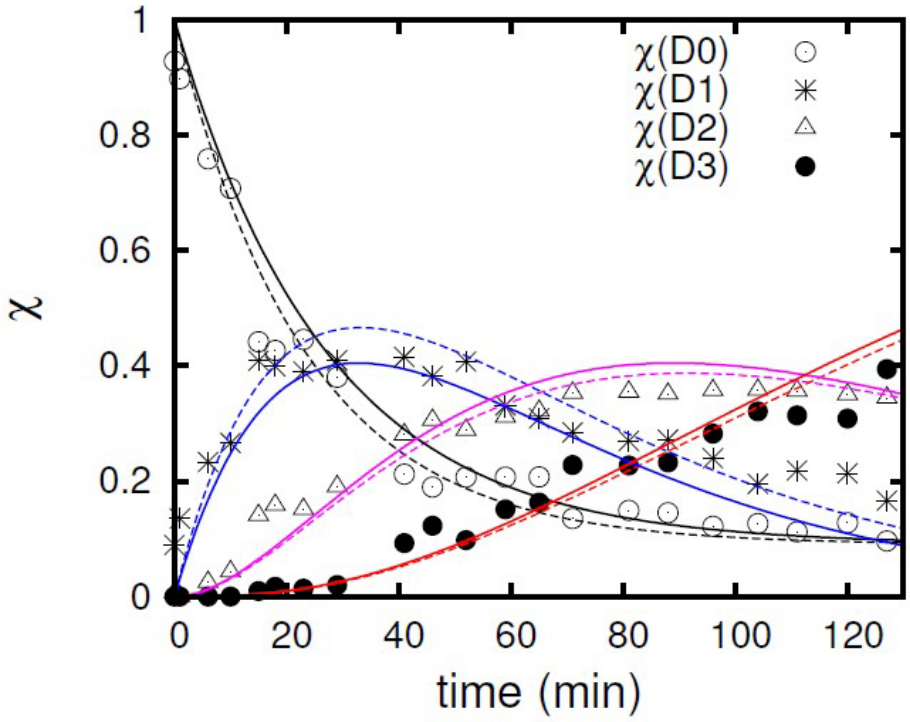

Figure 4.9. AcMX HDX progress curve monitored by ESI-MS. The dotted lines are global fits to the mole fraction of each isotopomer with three independent observed velocities v_a = 0.043 ± 0.019 min^{-1}, v_b = 0.020 ± 0.008 min^{-1}, and v_c = 0.012 ± 0.008 min^{-1}. The solid lines represent a global fit using an average site exchange rate ($v_{\bar{c}}$ = 0.012 ± 0.002 min^{-1}), assuming a geometric selection factor and isotope effects equal to unity. (The unreactivemole fraction $\chi_{\infty}^{D0}$was fixed at 0.9 for both fits. The data points for χ^{D0}incorporate this contribution).

A previously reported kinetic model for methyl group HDX (Pratt, 1977)) that accounts for both processive and distributive processes was simplified to a distributive model of three sequential, irreversible HDX steps with three independent rate constants (Equations 4.14-17). A global fit of all four isotopomer progress curves to this model (Figure 4.9, dotted lines) furnished three velocities (v_a, v_b, v_c). in an approximate 3:2:1 ratio. These results indicate that geometric selection effects are sufficient to account for the relative rate of formation of each isotopomer.

A second, simpler HDX model incorporating a single velocity parameter ($v_{\bar{c}}$), geometric selection, and isotope effects of unity (Equations 4.18-21) also gave a good global fit to all four progress curves (Figure 4.9, solid lines). This fit furnishes $k_{\bar{c}}$, the rate constant for exchange of a single methyl proton, and k_{HDX}, the AcMX methyl HDX rate constant, where $k_{HDX} = 3 \times k_{\bar{c}} = 27 \pm 5\ s^{-1}$.

Binding of AcMX to AaCS•OAA: stopped-flow fluorescence analysis.

A small or undetectable equilibrium fluorescence change can be a consequence of presteady-state fluorescence changes in opposite directions. The ligand AcMX-d3 was chosen for this analysis because the steady-state titration in D_2O, which excludes the possibility of time dependent changes due to HDX, resulted in a larger fluorescence change than the protonated ligand. To detect transient fluorescence changes in AaCS•OAA, it was rapidly mixed with varied concentrations of either AcMX in normal aqueous buffer or AcMX-d3 in D_2O-containing buffers. All fluorescence changes were completed within 20 ms. A very small decrease in fluorescence occurred during the instrument dead time, followed by a monophasic increase in fluorescence emission intensity (Figure 10). Each progress curve was fit to a single exponential equation. These data were analyzed to determine the concentration dependence of the observed rate (k_{obs}) and amplitudes of the fluorescence change.

The maximal amplitude of the fluorescence change appears to saturate at high AcMX-d3 concentrations and was fit to a simple hyperbolic isotherm with an apparent binding affinity, consistent with a K_d, of 12 ± 2 μM (Figure 4.11). This apparent binding

affinity is slightly higher than the K_ds calculated from steady-state titrations (Table 4.1). The observed rate either shows no concentration dependence or is too fast to observe quantitatively given the small signal change (Figure 4.11, inset). Rapid mixing of AcMX with AaCS•OAA in H_2O and D_2O resulted in similar data with lower signal to noise. These data are consistent with rapid equilibrium binding that has a fluorescence change too small to observe.

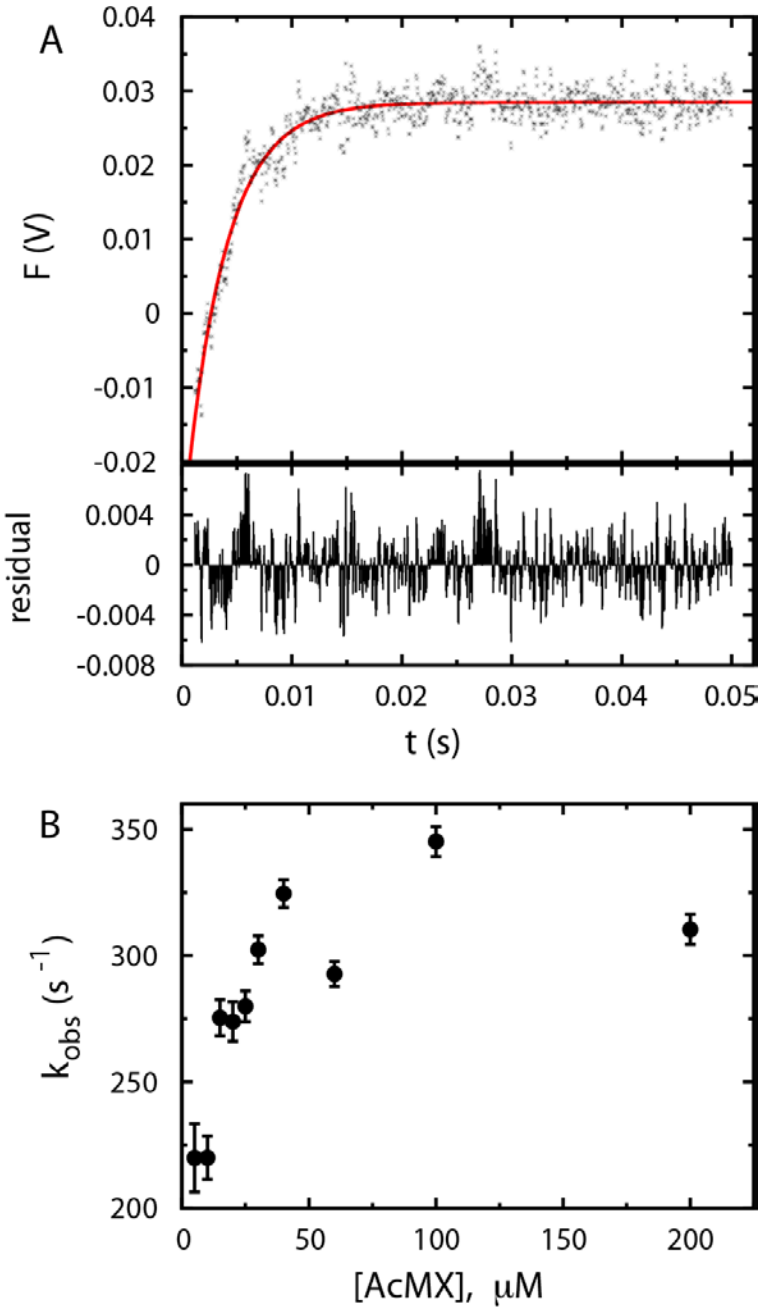

Figure 4.10. SFF analysis of AcMX binding to AaCS•OAA (H_2O buffer). A, A progress curves recorded at final concentrations of 1 μM AaCS, 100 μM OAA, and 20 μM AcMX at 25 °C. Experimental data (symbols) were fit to a single exponential function (solid red line) to obtain observed rate k_{obs} = 280 ± 6 s^{-1}. The bottom panel shows fitting residuals. B, k_{obs} as a function of [AcMX]. The range of values obtained is 220–345 s^{-1} (average 284 s^{-1}). The scatter of the k_{obs} data is too great to allow reliable fitting to a hyperbolic function but it seems likely that the ordinate axis intercept (e.g., k_{off}) is nonzero.

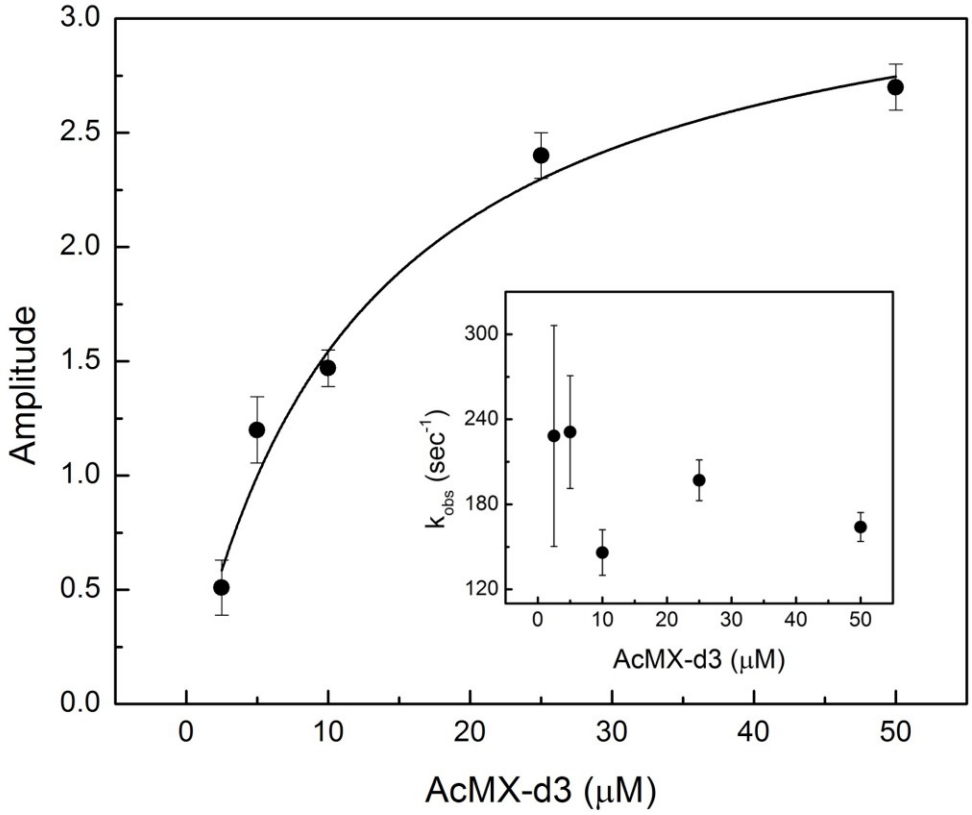

Figure 4.11. Amplitude of the fluorescence increase observed in SFF experiments mixing AaCS•OAA (pre-exchanged) with AcMX-d3 in D_2O. Variable concentrations of AcMX-d3 was ra pidly mixed with 10 μM AaCS (subunit) pre-equilibrated with 200 μM OAA in 50 mM potassium phosphate pD = 8.0, 100 mM KCl at 25 °C. Each data set was fit to a single exponential to determine the amplitude of the fluorescence change and the observed rate constant. The amplitude term appears to saturate at high AcMX-d3 concentrations with a maximum fluorescence increase of 14% at high [AcMX-d3]. *Inset*, concentration dependence of k_{obs}. No concentration dependence on the observed rate constants was observed.

AaCS•OAA + AcCoA-h3 single turnover reactions: stopped-flow fluorescence analysis.

Preliminary AaCS•OAA + AcCoA-h3 single turnover reactions were performed. Unbound AaCS was arbitrarily set to 100%, where buffer alone is 0%, fluorescence and saturating OAA quenched AaCS fluorescence by 21.5% (78.5% remaining fluorescence). The reaction of AcCoA-h3 with excess AaCS•OAA shows a rapid 11% rise in fluorescence during the instrument dead time (~ 2.0 ms). This was followed by a transient fluorescence rise that never returns to the OAA quenched baseline (representative data shown in Figure 12). The cause of the fast initial rise is unclear and not observed in TpCS•OAA (Kurz et al., 2009). These data were fit to a double exponential function (Eqn 4.22) with values for the fitted parameters given in Table 4.3.

$$Y = -A_1 e^{-k_{obs1}t} + -A_2 e^{-k_{obs2}t} + C \quad (22)$$

Rapid mixing of AaCS•OAA with AcCoA-d3 shows an even larger initial rise in fluorescence emission intensity (21% recovery) relative to reactions lacking AcCoA-d3. This is followed by a smaller transient fluorescence rise (Figure 4.12 inset). Qualitatively, there does appear to be a substrate kinetic isotope effect on both observed kinetic phases.

Table 4.3. Summary of fitted parameters from SFF studies mixing AaCS•OAA with a sub-stoichiometric concentration (1.5 µM) of AcCoA-h3.

Parameter	Value
A_1 (%)	1.0 ± 0.3
k_{obs1} (s^{-1})	200 ± 40
A_2 (%)	-1.5 ± 0.3
k_{obs2} (s^{-1})	54 ± 8
C	80.70 ± 0.02

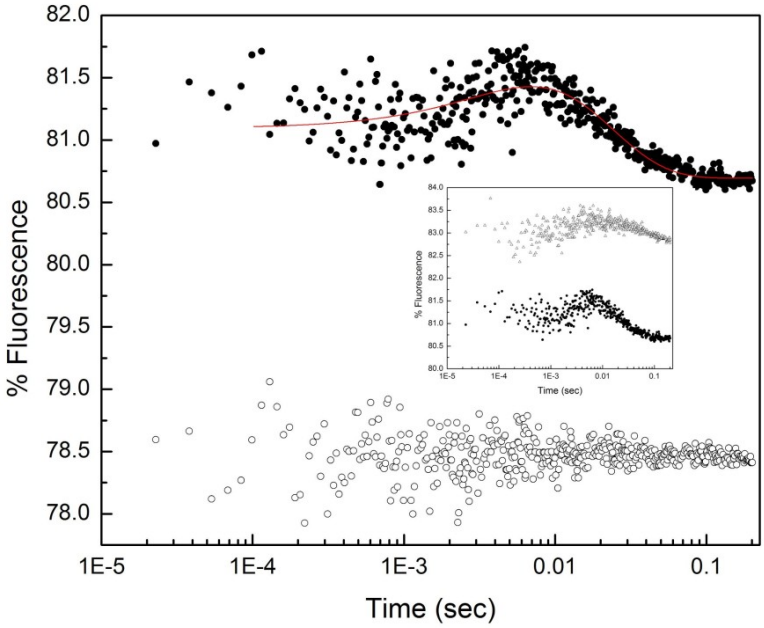

Figure 4.12. Reaction of AaCS•OAA with sub-stoichiometric AcCoA-h3 or AcCoA-d3 (1.5 µM) monitored by SFF. AaCS (10 µM) was pre-equilibrated with 200 µM OAA in syringe 1 and was rapidly mixed with 200 µM OAA + 1.5 µM AcCoA-h3 (black circles). A control reaction lacking AcCoA was also done to show the baseline OAA quenched fluorescence (open circles). The solid red line is a fit to a double exponential and the fitted parameters are given in Table 3. To determine if there is a substrate kinetic isotope effect, parallel experiments containing 1.5 µM AcCoA-d3 were done (open triangles in the inset).

Condensation can be rate-limiting for AaCS.

Steady-state kinetics of TpCS and AaCSH6 were monitored in H_2O or D_2O as a function of [AcCoA-(d3)] with saturating OAA (Figures 13 and 14, respectively). Each data set was fit to the Michaelis-Menten equation to determine V_{max} and K_M (Table 4). These values were used to determine KIEs for TpCS and AaCS (Table 5). TpCS displayed a small substrate KIE on *V/K* with no effect on the maximal rate (Figure 12A) and solvent isotope effect of around 2 for both deuterated and protonated substrates. This is consistent with earlier reports that indicate TpCS is almost entirely rate limited by hydrolysis so no substrate isotope effect was expected (Kurz et al., 2000; Kurz et al., 2009). However, AaCS displays comparatively larger substrate KIE on both V_{max} and V/K with the largest effect on V/K of AcCoA-d3 in D_2O (Table 4.5). AaCS has a substantially larger substrate KIE observed in $^{D}(V_{max}/K_M)$: 2.7 relative to 1.3 for TpCS (Table 5). These data suggest that removal of a deuteron (i.e., not hydrolysis) is at least partially rate-limiting in steady-state conversion of AcCoA-d3 by AaCS.

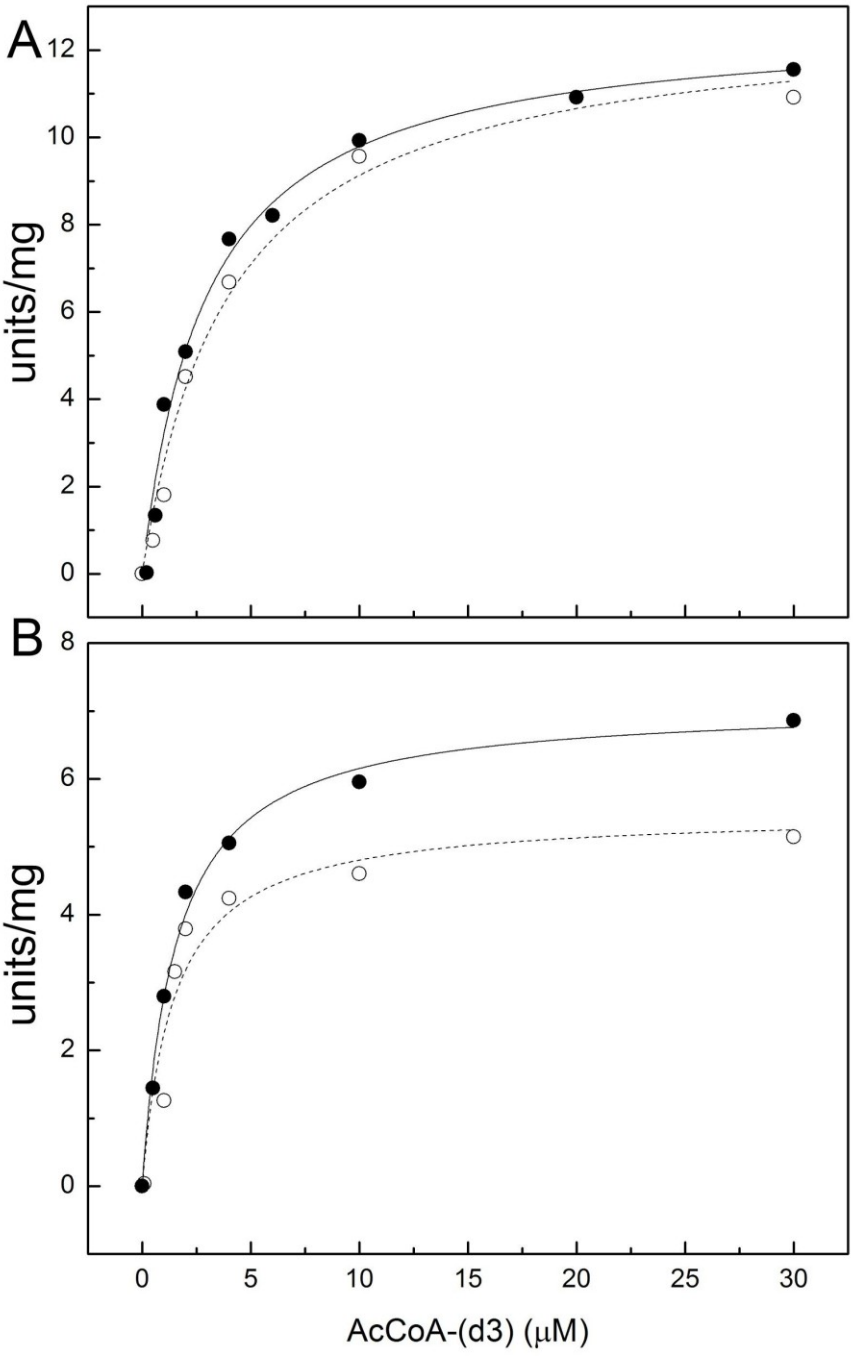

Figure 4.13. Steady-state kinetic characterization of TpCS. Initial velocities were measured with either AcCoA-h3 (black circles) or AcCoA-d3 (open circles) at saturating OAA. Panel A shows data obtained in H_2O and panel B shows data obtained in D_2O. Steady-state kinetic parameters are listed in Table 4.

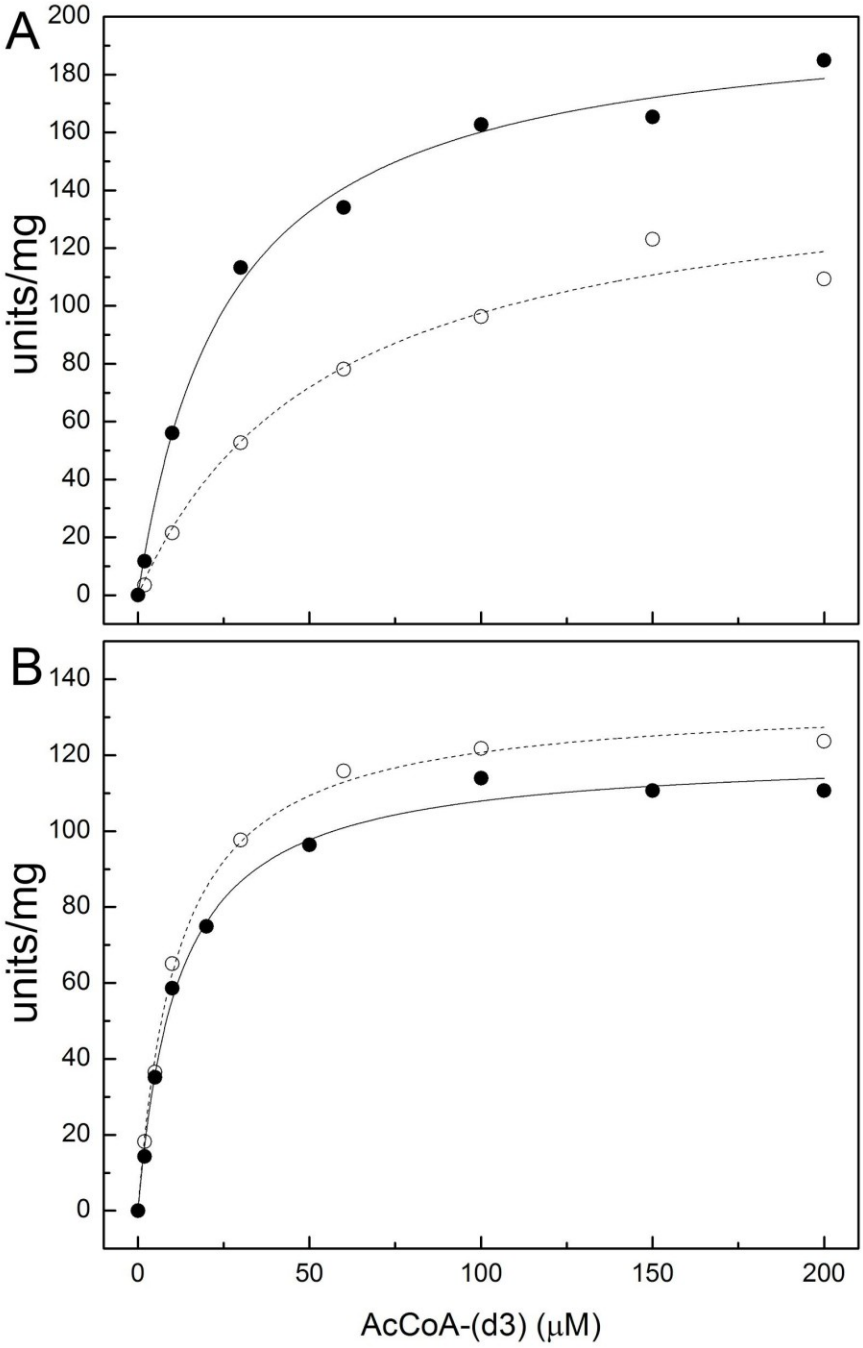

Figure 4.14. Steady-state kinetic characterization of AaCSH6. Initial velocities were measured with either AcCoA-h3 (black circles) and AcCoA-d3 (open circles) at saturating OAA. Panel A shows data obtained in H_2O and panel B shows data obtained in D_2O. Steady-state kinetic parameters are listed in Table 4.

Table 4.4. Steady-state kinetic parameters for TpCS and AaCSH6 obtained in H_2O or D_2O.

	TpCS	AaCSH6
AcCoA-h3 substrate		
V_{max} (units/mg)	12.7 ± 0.5 (H_2O) 7.1 ± 0.2 (D_2O)	202 ± 6 (H_2O) 121 ± 2 (D_2O)
k_{cat} (s^{-1})	9.5 ± 0.4 (H_2O)[a] 5.3 ± 0.1 (D_2O)	171 ± 5 (H_2O)[b] 102 ± 2 (D_2O)
K_M (μM)	3.0 ± 0.4 (H_2O)[c] 1.6 ± 0.2 (D_2O)	26 ± 3 (H_2O)[d] 12 ± 1 (D_2O)
k_{cat}/K_M (μM^{-1} s^{-1})	3.2 ± 0.4 (H_2O) 3.3 ± 0.4 (D_2O)	6.6 ± 0.8 (H_2O) 8.5 ± 0.7 (D_2O)
AcCoA-d3 substrate		
V_{max} (units/mg)	12.8 ± 0.7 (H_2O) 5.5 ± 0.5 (D_2O)	150 ± 10 (H_2O) 135 ± 2 (D_2O)
k_{cat} (s^{-1})	9.5 ± 0.5 (H_2O) 4.1 ± 0.4 (D_2O)	127 ± 8 (H_2O) 114 ± 2 (D_2O)
K_M (μM)	4.0 ± 0.7 (H_2O) 1.5 ± 0.5 (D_2O)	60 ± 10 (H_2O) 12 ± 0.9 (D_2O)
k_{cat}/K_M (μM^{-1} s^{-1})	2.4 ± 0.4 (H_2O) 2.7 ± 0.9 (D_2O)	2.1 ± 0.4 (H_2O) 9.5 ± 0.7 (D_2O)

[a] Reported to be 9.2 s^{-1} (Kurz et al., 2000).
[b] Reported to be 90 s^{-1} (Francois et al., 2006). There is substantial variation in k_{cat} for AaCS, TpCS (Kurz et al., 2000), and other CS enzymes.
[c] Reported to be 0.67 μM (Kurz et al., 2005).
[d] Reported to be 29 μM (Francois et al., 2006).

Table 4.5. Substrate and solvent kinetic isotope effects on TpCS and AaCSH6.

	TpCS	AaCSH6
$^{D}V_{max}$	1.0 ± 0.1 (H_2O)[a] 1.3 ± 0.1 (D_2O)[a]	1.3 ± 0.1 (H_2O) 0.90 ± 0.02 (D_2O)
$^{D}(V_{max}/K_M)$	1.3 ± 0.3 (H_2O) 1.2 ± 0.4 (D_2O)	3.1 ± 0.7 (H_2O) 0.9 ± 0.1 (D_2O)
$^{D2O}V_{max}$	1.8 ± 0.1 (AcCoA-h3)[b] 2.3 ± 0.2 (AcCoA-d3)[c]	1.7 ± 0.1 (AcCoA-h3) 1.1 ± 0.1 (AcCoA-d3)
$^{D2O}(V_{max}/K_M)$	1.0 ± 0.2 (AcCoA-h3) 0.9 ± 0.3 (AcCoA-d3)	0.8 ± 0.1 (AcCoA-h3) 0.20 ± 0.05 (AcCoA-d3)

[a] Reported to be 1.17 in both H_2O and D_2O (Kurz et al., 2000).
[b] Reported to be 2.41 (Kurz et al., 2000).
[c] Reported to be 2.33 (Kurz et al., 2000).

4.4 Discussion

The formation of citrate catalyzed by CS requires a Claisen/aldol condensation reaction followed by hydrolysis of the CitCoA intermediate. Together, these reactions require three chemical steps: proton transfer that forms a reactive carbanion at the terminal methyl group of AcCoA, condensation with the polarized carbonyl of OAA forming CitCoA, and finally hydrolysis which releases the products citrate and CoA. Studying these partial reactions has been difficult by traditional mutagenesis studies because many of the active site residues are thought to participate in both condensation and hydrolysis. The AcCoA substrate analogue AcMX has been previously shown to undergo condensation without subsequent hydrolysis in TpCS (Kurz et al., 2009). However, since TpCS efficiently converts AcMX to CitMX, proton transfer is not isolated

from condensation. While HDX implies carbanion formation, it is unclear if AcMX HDX catalyzed by TpCS•OAA occurs when the enolate is formed or during reverse condensation. We report here that AaCS is the ideal form of CS to study proton transfer because AaCS stabilizes the ternary complex over condensation while undergoing rapid HDX.

Proton transfer without condensation.

In CS forms containing a reporter Trp the reaction chemistry can be readily monitored. Proton transfer may be monitored without the complication of condensation in PCS but PCS lacks a suitable reporter Trp (Kurz et al., 2009). A steady-state fluorescence change is not expected if proton transfer is occurring without condensation but a reporter Trp allows detection of any transient formation of CitMX.

In AaCS Trp400 reports on OAA binding. Despite extensive primary sequence divergence and quaternary structural differences the active sites of AaCS and TpCS are structurally similar. Like TpCS, fluorescence quenching is caused by proximity of a polarized OAA carbonyl to Trp400 upon binding to AaCS. Therefore, any fluorescence "dequenching" upon binding to AcMX would be assumed to be caused by condensation. Addition of AcMX to TpCS•OAA alleviates most of the fluorescence quenching due to destruction of the OAA carbonyl during condensation. However, incubating AaCS•OAA with AcMX in H_2O does not form any detectable CitMX. Interestingly, titrating AaCS•OAA (pre-exchanged) with AcMX-d3 in D_2O does result in a saturating fluorescence change (Figure 6). The cause of the fluorescence change is unclear but because AaCS•OAA is further quenched upon binding AcMX-d3, the formation of CitMX is unlikely.

SFF studies of AaCS•OAA binding to AcMX-(d3) indicate that if CitMX is forming it is extremely transient and would have to occur in the deadtime of the instrument. A very small monophasic increase in fluorescence was observed and may be a consequence of AcMX carbanion formation, reducing the effective positive potential at the OAA carbonyl carbon, or, less likely, a limited amount of CitMX formation. Another potential reason for the difference is the use of a high-pass optical filter for SFF and a monochromator for titration experiments. There is no concentration dependence on the observed rate constants but the amplitude of the fluorescence change does appear to saturate at high AcMX-d3 concentrations with an apparent binding affinity that is similar to the K_d observed by steady-state titrations (Table 4.1).

AaCS•OAA catalyzes HDX without condensation.

HDX at the terminal methyl group of AcMX catalyzed by AaCS is direct evidence that proton abstraction must occur. Deuterium incorporation can be directly monitored by NMR and mass spectrometry. Under the same reaction conditions (pD 7.9, 25 °C), AaCS catalyzes AcCoA-dependent turnover at about four times the rate of HDX measured by NMR or ESI-MS. These differences in rates are consistent with what is observed in TpCS which catalyzes AcCoA-dependent turnover at about five times the rate of HDX (Kurz et al., 2009).

HDX does not need to be kinetically competent for AcCoA-dependent turnover. It is possible that enolization is much faster than deuteron addition. If the ternary complex forms and dissociates faster than the rate of HDX observed by NMR then not

every ternary complex that forms will result in an HDX event. Moreover, rapid and reversible ternary complex formation would allow the dissociated AcMX isotopomer to equilibrate with bulk AcMX, leading to HDX that is distributive in nature (Figure 4.15). In contrast, if the lifetime of the ternary complex is long relative to the time required for methyl group rotation and HDX, multiple HDX events could occur prior to AcMX dissociation. These circumstances would lead to HDX that is processive in nature (Figure 4.15). In distributive HDX, **D1** is the only isotopomer product formed early in the HDX reaction, without an initial lag phase (Figure 4.8). The other isotopomer products will be formed in succession, with distinct lag phases. In contrast, a processive HDX process yields some of each deuterated isotopomer product (**D1–D3**) at early times during the reaction. Even though the introduction of deuterium atoms leads to chemical shift changes in the remaining methyl protons, the overlapping signals mean it is difficult to distinguish between distributive and processive HDX models by NMR.

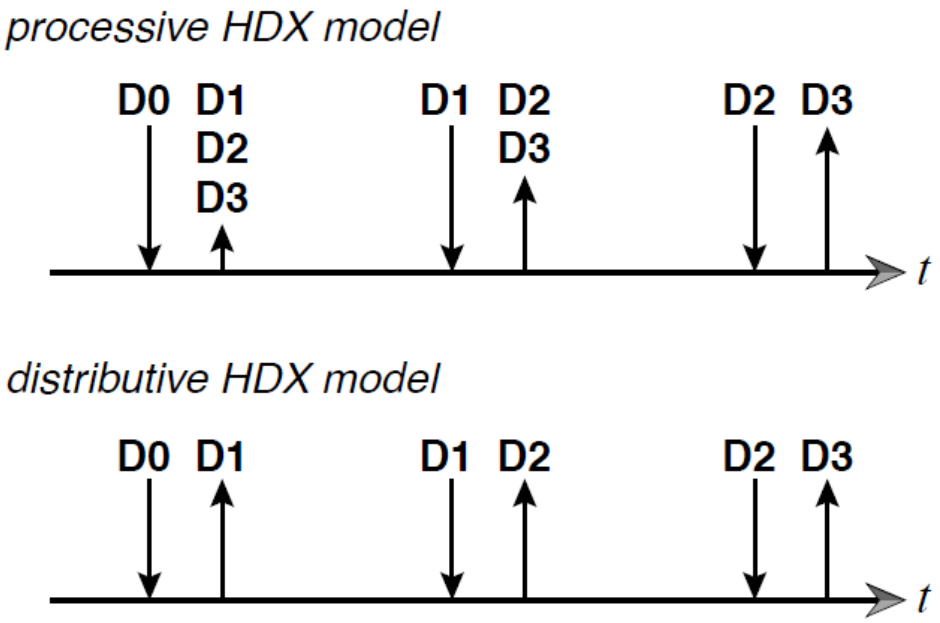

Figure 4.15. Kinetic models for CS•OAA-catalyzed AcMX HDX shown as a Cleland-type diagram. The processive model predicts initial formation of multiple isotopomers (with abundance **D1** > **D2** > **D3**, but with all progress curves increasing from t = 0). The distributive model predicts initial formation of only **D1**, with lags in the production of **D2** and **D3**. All dissociation steps (upward arrows) are presumed to result in equilibration with the bulk AcMX isotopomer pool and are therefore effectively irreversible.

ESI-MS analysis allowed the quantitation of individual AcMX isotopomers and was used to distinguish between the two possible models for HDX of AcMX catalyzed by AaCS•OAA. This technique confirmed a distributive model of HDX, meaning that no more than one exchange event (including silent D→D exchanges accounted for by geometric selection factors) occurs prior to dissociation of AcMX from the ternary complex. This model is consistent with the observation that HDX is slower than AcCoA-dependent turnover but does not identify the step in which HDX is occurring.

Pre-steady-state kinetic analysis is consistent with a distributive mechanism for HDX.

The apparent binding affinity determined by SFF is in good agreement with binding constants determined by steady-state fluorescence titrations of AaCS•OAA with AcMX or AcMX-d3. However, from these data it is not possible to determine if pre steady-state kinetics follow a simple one step binding model or a two-step binding model with rapid pre-equilibrium followed by a slower isomerization step. The off rates estimated by either model are consistent with distributive HDX of AcMX.

Rapidly mixing AaCS•OAA with AcMX-d3 in D_2O best matches the conditions used to determine the rate of HDX by NMR. The SFF k_{obs} values are independent of AcMX-d3 concentration and have an average value of ~200 s^{-1} in D_2O. Using this observed and the apparent binding affinity of 12 µM the upper and lower limit for the off rate can be estimated for both a one-step and two-step binding model. Since HDX requires ACMX isotopomer dissociation, the lower limit of the off rate (k_{off}) is simply the rate of HDX determined by NMR (18 s^{-1}). The off rate determined with a one-step binding model (Eqn 22) is ~90 s^{-1}.

$$k_{off} = \frac{k_{obs}}{1+\frac{[L]}{K_d}} \qquad (23)$$

The ratio of the measured binding affinities by SFF (K_{d1} = 12 µM) and steady-state titration ($K_{d1}K_{d2}$ = 6 µM) indicate that k_2 must be twice k_{-2} in a two-step binding model. In this model, $k_{obs} = k_2 + k_{-2}$ and considering the average k_{obs} in D_2O is ~200 s^{-1}, k_2 must

be ~130 s^{-1}. The lower limit of k_{off} in a two-step binding model can be estimated considering k_{off} must be faster than k_2 for rapid equilibrium to occur. Therefore k_{off} must be at least 130 s^{-1}.

If the binding model is more complex, the off rate must still be less than the observed rates of ~200 s^{-1}. In both cases the calculated rate of AcMX dissociation is faster than the observed rate for HDX suggesting that every AcMX (isotopomers **D0** – **D2**) binding event does not result in HDX. These estimations are consistent with the distributive HDX pattern directly observed by ESI-MS.

The probability of proton exchange can be estimated for one-step or two-step binding models by taking the ratio of the observed rate of HDX from NMR (18 s^{-1}) and the off rates estimated above. In the case of a one-step binding model, 20% of binding events result in proton exchange and 14% of binding events result in proton exchange in a two-step binding model.

The condensation reaction has the potential to be rate-limiting for AaCS.

AcMX-d3, in which the terminal methyl group is fully deuterated and unable to undergo uncatalyzed exchange with solvent H_2O, was used to detect any substrate KIEs. These reactions were also monitored in D_2O to detect any solvent KIEs. Steady-state turnover in TpCS has a negligible substrate KIE, which is not surprising considering that hydrolysis is rate-limiting (Kurz et. al., 2000). However, AcCoA-dependent turnover catalyzed by AaCS•OAA does have a substrate KIE, $^{D}(V_{max}/K_M)$, which indicates that hydrolysis is not rate-limiting. These data suggest that the condensation reaction

catalyzed by AaCS can be made at least partly rate limiting in the steady-state by deuterium substitution.

The ternary AaCS•OAA•AcMX complex is favored over the binary AaCS•CitMX complex.

TpCS stabilizes the binary condensation product TpCS•CitCoA relative to the pre-condensation ternary complex whereas PCS stabilizes both complexes to asimilar extent (Kurz et al., 2009). The preponderance of the evidence obtained with TpCS furthermore suggests that the dead-end complex TpCS•CitMX is preferentially stabilized relative to the Michaelis complex analogue TpCS•OAA•AcMX. HDX in AcMX catalyzed by AaCS•OAA occurs without detectable condensation, which suggests that different CS forms have different on-enzyme equilibria. These conclusions are illustrated best by a schematic depiction of a portion of the complete overall free energy reaction profile below (Figure 4.16) (Kurz et al., 2009).

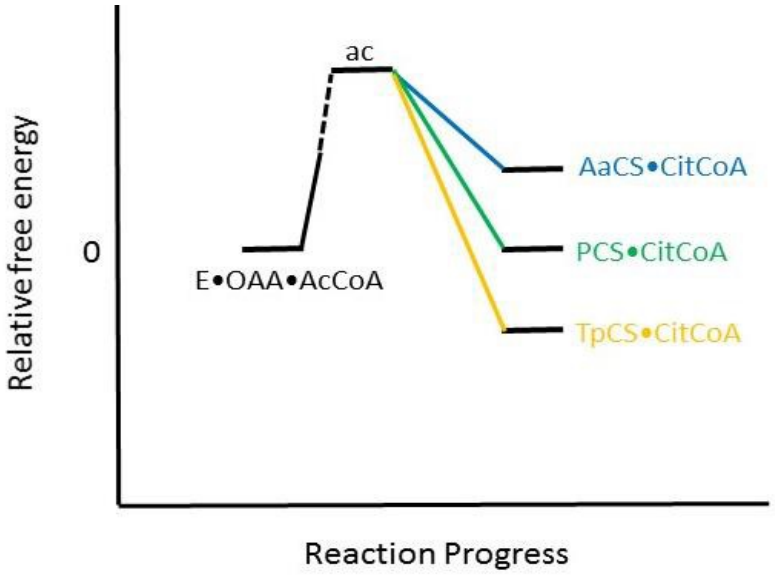

Figure 4.16. Schematic free energy reaction profiles of the condensation reaction catalyzed by CS. The full TpCS and partial PCS profiles are based on measurements with real substrates, not the substrate analogue AcMX, and are quantitatively described in Kurz et al., 2009. The free energy of each ternary complex is arbitrarily set to 0 indicating that anything below that is more stable for a given enzyme form ($\Delta G < 0$). The partial dashed line indicates that is it unlikely that each enzyme has the same kinetic barrier (ac). SFF studies suggest that AaCS does not form a binary complex with CitMX to a significant extent. If this also applies to the reaction of AaCS•OAA with AcCoA, AaCS appears to stabilize the ternary complex relative to the binary condensation product. PCS stabilizes both complexes to a similar extent, and TpCS preferentially stabilizes the binary condensation product.

Preliminary AaCS•OAA + AcCoA-h3 single turnover reactions.

For the binding of AcCoA-h3/AcCoA-d3 to TpCS•OAA, two kinetic phases are observed during single turnover reactions. The first being a rise in fluorescence correspond to destruction of the polarized OAA carbonyl (this reports on a combination of proton transfer and condensation) and the second being a drop in fluorescence back to OAA quenched baseline (this reports on a combination of hydrolysis of CitCoA and dissociation followed the rapid binding of unreacted excess OAA) (Kurz et al., 2009).

Preliminary AaCS•OAA + AcCoA-h3 single turnover reactions were performed. The chemical steps corresponding to the observed fluorescence changes are currently unclear. AaCS appears to have a fast phase occurring during the instrument dead-time using both AcCoA-h3 and AcCoA-d3 substrates that is missing for TpCS (Kurz et al., 2009). The cause of this fluorescence change is currently unknown. The fast phase was followed by a second, observed, kinetic phase with a k_{obs1} = 200 s^{-1}. The third and slowest kinetic phase (k_{obs2} = 54 s^{-1}) is too slow to be kinetically competent in steady-state catalysis (171 s^{-1}, Table 4.1). There are significant differences observed here between AaCS and TpCS and these experiments should be repeated.

4.5 References

1. Amyes, T. L., and Richard, J. P. (1992) Generation and stability of a simple thiol ester enolate in aqueous solution. *J. Am. Chem. Soc. 114*, 10297–10302.

2. Bayer, E., Bauer, B., and Eggerer, H. (1981) Evidence from inhibitor studies for conformational changes of citrate synthase. Eur. *J. Biochem*. 120, 155–160.

3. Bové, J., Martin, R. O., Ingraham, L. L., and Stumpf, P. K. (1959) Studies of the mechanism of action of the condensing enzyme. *J. Biol. Chem*. 234, 999–1003.

4. Bradford, M. M. (1976) A rapid and sensitive method for the quantitation of microgram quantities of protein utilizing the principle of protein-dye binding. *Anal. Biochem*. 72, 248–254.

5. Burns, K. L., Gelbaum, L. T., Sullards, M. C., Bostwick, D. E., & May, S. W. (2005). Iso- coenzyme A. *J. Biol. Chem*, *280*(17), 16550-16558.

6. Clark, J. D., O'Keefe, S. J., and Knowles, J. R. (1988) Malate synthase: proof of a stepwise Claisen condensation using the double isotope fractionation test. *Biochemistry* 27, 5961–5971.

7. Collier, H. B. (1973). A note on the molar absorptivity of reduced Ellman's reagent, 3- carboxylato-4-nitrothiophenolate. *Analytical biochemistry*, *56*(1), 310-311.

8. Dawson, R.M.C. et al., Data for Biochemical Research, 3rd ed., 116-117 (1993).

9. Duckworth, H. W., Nguyen, N. T., Gao, Y., Donald, L. J., Maurus, R., Ayed, A., Bruneau, B., and Brayer, G. D. (2013) Enzyme-substrate complexes of allosteric citrate synthase: Evidence for a novel intermediate in substrate binding. *Biochim. Biophys. Acta*

10. Eggerer, H. (1965) Zum Mechanismus der biologischen Umwandlung von Citronensäure. VI. Citrat-Synthase ist eine Acetyl-CoA-Enolase. *Biochem. Z*. 343, 111– 138.

11. Francois, J. A., Starks, C. M., Sivanuntakorn, S., Jiang, H., Ransome, A. E., Nam, J.-W., Constantine, C. Z., and Kappock, T. J. (2006) Structure of a NADH-insensitive hexameric citrate synthase that resists acid inactivation. *Biochemistry* 45, 13487–13499.

12. Gauthier, N., Wu, J. W., Wang, S. P., Allard, P., Mamer, O. A., Sweetman, L., Moser, A., Kratz, L., Alvarez, F., Robitaille, Y., Lepine, F., Mitchell, G. (2013). A liver-specific defect of Acyl-CoA degradation produces hyperammonemia, hypoglycemia and a distinct hepatic Acyl-CoA pattern. *PloS one*, *8*(7), e60581.

13. Gerlt, J. A., and Gassman, P. G. (1993) Understanding the rates of certain enzyme-catalyzed reactions: proton abstraction from carbon acids, acyl-transfer reactions, and displacement reactions of phosphodiesters. *Biochemistry* 32, 11943–11952.

14. Gerlt, J. A. (2007) Enzyme catalysis of proton transfer at carbon atoms, in Hydrogen- transfer reactions (Hynes, J. T., Klinman, J. P., Limbach, H. H., and Schowen, R. L., Eds.) pp 1107-1138, *Wiley-VCH*, Weinheim, Germany.

15. Gill, S. C., and von Hippel, P. H. (1989) Calculation of protein extinction coefficients from amino acid sequence data. *Anal. Biochem*. 182, 319–326.

16. Griep, M. A., and McHenry, C. S. (1990) Dissociation of the DNA polymerase III holoenzyme b2 subunits is accompanied by conformational change at distal cysteines 333. *J. Biol. Chem.* 265, 20356–20363.

17. Johnson, K. A. In The enzymes; Sigman, D. S., Ed.; Academic Press, 1992; Vol. 20; pp 1–61.

18. Kurz, L. C., Constantine, C. Z., Jiang, H., and Kappock, T. J. (2009) The partial substrate dethiaacetyl-coenzyme A mimics all critical carbon acid reactions in the condensation half reaction catalyzed by *Thermoplasma acidophilum* citrate synthase. Biochemistry 48, 7878–7891.

19. Kurz, L. C., Drysdale, G., Riley, M., Tomar, M. A., Chen, J., Russell, R. J. M., and Danson, M. J. (2000) Kinetics and mechanism of the citrate synthase from the thermophilic archaeon *Thermoplasma acidophilum*. *Biochemistry* 39, 2283–2296.

20. Kurz, L. C., Fite, B., Jean, J., Park, J., Erpelding, T., and Callis, P. (2005) Photophysics of tryptophan fluorescence: link with the catalytic strategy of the citrate synthase from *Thermoplasma acidophilum*. *Biochemistry* 44, 1394–1413.

21. Kurz, L. C., Nakra, T., Stein, R., Plungkhen, W., Riley, M., Hsu, F., and Drysdale, G. R. (1998) Effects of changes in three catalytic residues on the relative stabilities of some of the intermediates and transition states in the citrate synthase reaction. *Biochemistry* 37, 9724–9737.

22. Kurz, L. C., Roble, J. H., Nakra, T., Drysdale, G. R., Buzan, J. M., Schwartz, B., and Drueckhammer (1997) Ability of single-site mutants of citrate synthase to catalyze proton transfer from the methyl group of dethiaacetyl-coenzyme A, a non-thioester substrate analog. *Biochemistry* 36, 3981–3990.

23. Kurz, L. C., Shah, S., Frieden, C., Nakra, T., Stein, R. E., Drysdale, G. R., Evans, C. T., and Srere, P. A. (1995) Catalytic strategy of citrate synthase: Subunit interactions revealed as a consequence of a single amino acid change in the oxaloacetate binding site. *Biochemistry* 34, 13278–13288.

24. Kuzmič, P. (1996). Program DYNAFIT for the analysis of enzyme kinetic data: application to HIV proteinase. *Analytical biochemistry*, *237*(2), 260-273.

25. Marcus, A., and Vennesland, B. (1958) Studies with acetyl coenzyme A and condensing enzyme in D_2O. *J. Biol. Chem*. 233, 727–730.

26. Martin, D. P., Bibart, R. T., and Drueckhammer, D. G. (1994) Synthesis of novel analogs of acetyl coenzyme A: Mimics of enzyme reaction intermediates. *J. Am. Chem. Soc*. 116, 4660–4668.

27. Myers, J. A., and Boyer, P. D. (1984) Oxygen and deuterium exchanges show reversal of catalytic steps of citrate synthase: catalytic cooperativity is not observed. *Biochemistry* 23, 1264–1269.

28. Nguyen, N. T., Maurus, R., Stokell, D. J., Ayed, A., Duckworth, H. W., and Brayer, G. D. (2001) Comparative analysis of folding and substrate binding sites between regulated hexameric type II citrate synthases and unregulated dimeric type I enzymes. *Biochemistry* 40, 13177–13187.

29. Pratt, R. F. (1977) Rabbit muscle aldolase catalyzed proton exchange of hydroxyacetone phosphate with solvent. *Biochemistry* 16, 3988–3994.

30. Rufus Lumry, Emil L. Smith, Ruby R. Glantz *J. Am. Chem. Soc*., 1951, 73 (9), pp 4330– 4340.

31. Rose, I. A. (1958) The absolute configuration of dihydroxyacetone phosphate tritiated by aldolase reaction. *J. Am. Chem. Soc*. 80, 5835–5836.

32. Russell, R. J. M., Hough, D. W., Danson, M. J., and Taylor, G. L. (1994) The crystal structure of citrate synthase from the thermophilic archaeon, *Thermoplasma acidophilum*. *Structure 2*, 356 1157–1167.

33. Srere, P. A. (1967) A magnetic resonance study of the citrate synthase reaction. *Biochem. Biophys. Res. Commun*. 26, 609–614.

34. Srere, P. A. (1969). [1] Citrate synthase: [EC 4.1. 3.7. Citrate oxaloacetate-lyase (CoA- acetylating)]. *Methods in enzymology*, *13*, 3-11.

35. Sutherland, C. M., Katharine J.and Henneke, Towner, P., Hough, D. W., and Danson, M. J. (1990) Citrate synthase from the thermophilic archaebacterium *Thermoplasma acidophilium*. Cloning and sequencing of the gene. *Eur. J. Biochem.* 194, 839–844.

36. Thibblin, A., and Jencks, W. P. (1979) Unstable carbanions. General acid catalysis of the cleavage of 1-phenylcyclopropanol and 1-phenyl-2-arylcyclopropanol anions. *J. Am. Chem. Soc*. 101, 4963–4973.

37. Usher, K. C., Remington, S. J., Martin, D. P., and Drueckhammer, D. G. (1994) A very short hydrogen bond provides only moderate stabilization of an enzyme-inhibitor complex of citrate synthase. *Biochemistry* 33, 7753–7759.

38. Wiegand, G., Remington, S., Deisenhofer, J., and Huber, R. (1984) Crystal structure analysis and molecular model of a complex of citrate synthase with oxaloacetate and S-acetonyl coenzyme A. *J. Mol. Biol*. 174, 205–219.

39. Wu, P., and Brand, L. (1994) Resonance energy transfer: Methods and applications. *Anal. Biochem*. 218, 1–13.

APPENDIX

APPENDIX

Supplementary Methods

AaCSFl

The procedure used to isolate AaCS^{intein} from BL21(DE3) cells transformed with pJK240 was followed as previously described up to the chitin column step, except that buffer J (50 mM , pH 8.0, 500 mM KCl, and 1 mM EDTA) was used instead of buffer H to equilibrate the chitin column and to perform protein buffer-exchange (Francois et a., 2006). After washing the chitin column (2.5 cm $\times$ 6 cm, 24 mL) with 3 column volumes (CV) of buffer J, the column was flushed with 3 CV of buffer J containing 50 mM sodium 2-mercaptoethanesulfonate (MESNA). After 48 h at 4 °C, the column was developed with 3 CV buffer J. Fractions containing protein were pooled, concentrated by ultracentrifugation (Amicon YM-30 Centriprep centrifugal filter device), and buffer-exchanged to dilute MESNA to < 10 μM. A solution of 3 mM **1** in buffer K (50 mM , pH 8.0, 100 mM KCl) (1 mL) was added to three Eppendorf tubes, each containing AaCS- MESNA (15.6 mg mL^{-1} in 0.22 mL buffer J); a 1:42 ratio of AaCS-MESNA:**1** was present upon mixing. After 48 h at 4 °C, the reaction mixtures were combined and subjected to three cycles of dilution-reconcentration in buffer K. The concentrated AaCSFl solution (0.2 mL) was diluted into buffer K plus 20 mM 2-mercaptoethanol (βME, 2 mL). After 24 h at 4 °C, dilution-reconcentration in buffer K (five cycles) was used to dilute βME to < 10 μM. The

concentrated protein was applied to a Sephadex G25 column (2.5 cm × 33 cm, 130 mL) equilibrated and then developed in buffer K. Fractions containing protein were combined, concentrated, and diluted-reconcentrated in buffer K plus 10 mM βME.

Solutions containing AaCSFl appeared orange under visible illumination and green- yellow under UV illumination (302 nm). Single-use aliquots (13.7 mg mL^{-1}) were frozen and stored at -80 °C. As a control, AaCS-MESNA derivatized with N-2-[(fluorescein-5-carbonyl)amide]ethyl-L-cysteinamide was buffer-exchanged in the absence of βME. The major ESI-MS peak obtained was consistent with AaCS$(Fl)_2$. Excess, unreacted N-2-[(fluorescein-5-carbonyl)amide]ethyl-L-cysteinamide therefore appears to form a heterodisulfide with a single accessible cysteine per AaCS(Fl) subunit.

Tables

***Table A1**. Oligodeoxynucleotides used in this study.*[a]

name	mutant	strand	sequence ($5' \rightarrow 3'$)
898	W404F	coding	GGCTGGGTGAGCCAG TAAGGAAATGATTGA AGAA
899	W404F	non-coding	TTCTTCAATCATTTCCT TACTGGCTCACCCAGC C
959	W400F	coding	CCGCACCACCGGCTG TGAGCCAGT
960	W400F	non-coding	ACTGGCTCACAGCCG GTGGTGCGG

[a] Positions that alter the original sequence are underlined.

Determination of FRET efficiencies for various AaCSFl complexes.

Crystal structures of unliganded (PDB id 1k3p), the binary complex (PDB id 4jag), and the ternary complex (PDB id 2h12) show that the C-terminal residue is 25–30 Å from either

Trp400' or Trp404', regardless of what ligands are present (17, 24, 27). Trp-Fl Förster distances measured with unliganded and various ligand-bound forms of AaCSFl (Table 3) were similar, with an average $r_{\blacklozenge} = 33$ Å. This $r_{\blacklozenge}$ value is in the expected range, given that a fully extended Fl-tag is 10 Å long.

Table A2. Determination of FRET efficiencies for various AaCSFl complexes.

additions[a]	f_{AaCS} (M^{-1})	f_{AaCSFl} (M^{-1})	E	$\dot{r}_{DA}$ (Å)
none	2.23 x 10^8	1.91 x 10^8	0.257	32.2
OAA[b]	1.84 x 10^8	1.47 x 10^8	0.365	29.6
OAA+CMX[b,c]	1.59 x 10^8	1.42 x 10^8	0.190	34.4
OAA+AcMX[b,d]	1.64 x 10^8	1.46 x 10^8	0.199	34.1

[a] Conditions: excitation wavelength, 295 nm; emission wavelength, 346 nm temperature, 25 C; 50 mM potassium phosphate, pH 8.0, 100 mM KCl; final sample volume, 2.5 mL.
[b] OAA was added to a final concentration of 0.1 mM. Emission intensities have been corrected for inner filter effect due to OAA.
[c] CMX was added to a final concentration of 0.11 mM. No inner filter effect correction was necessary for CMX.
[d] AcMX was added to a final concentration of 0.13 mM. No inner filter effect correction was necessary for AcMX. The excitation slit width was 2.5 nm.

Supplementary Figures

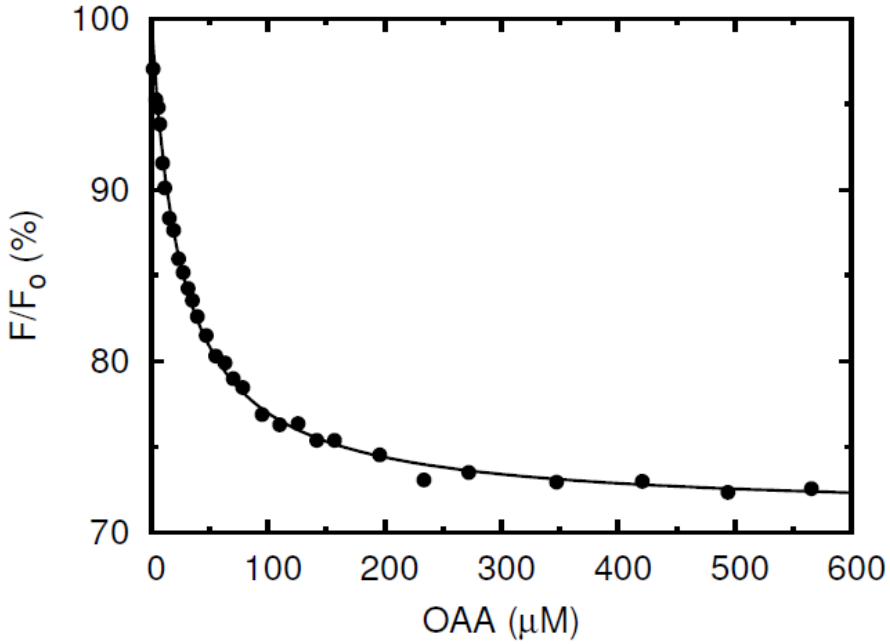

Figure A1. OAA fluorescence titration data recorded in 50 mM potassium phosphate, pH 8, 100 mM KCl containing 0.425 mM AaCSFl at 25 °C (excitation: 296 nm; emission: 340 nm). The solid line is a fit of the data to a single binding site (Table 1).

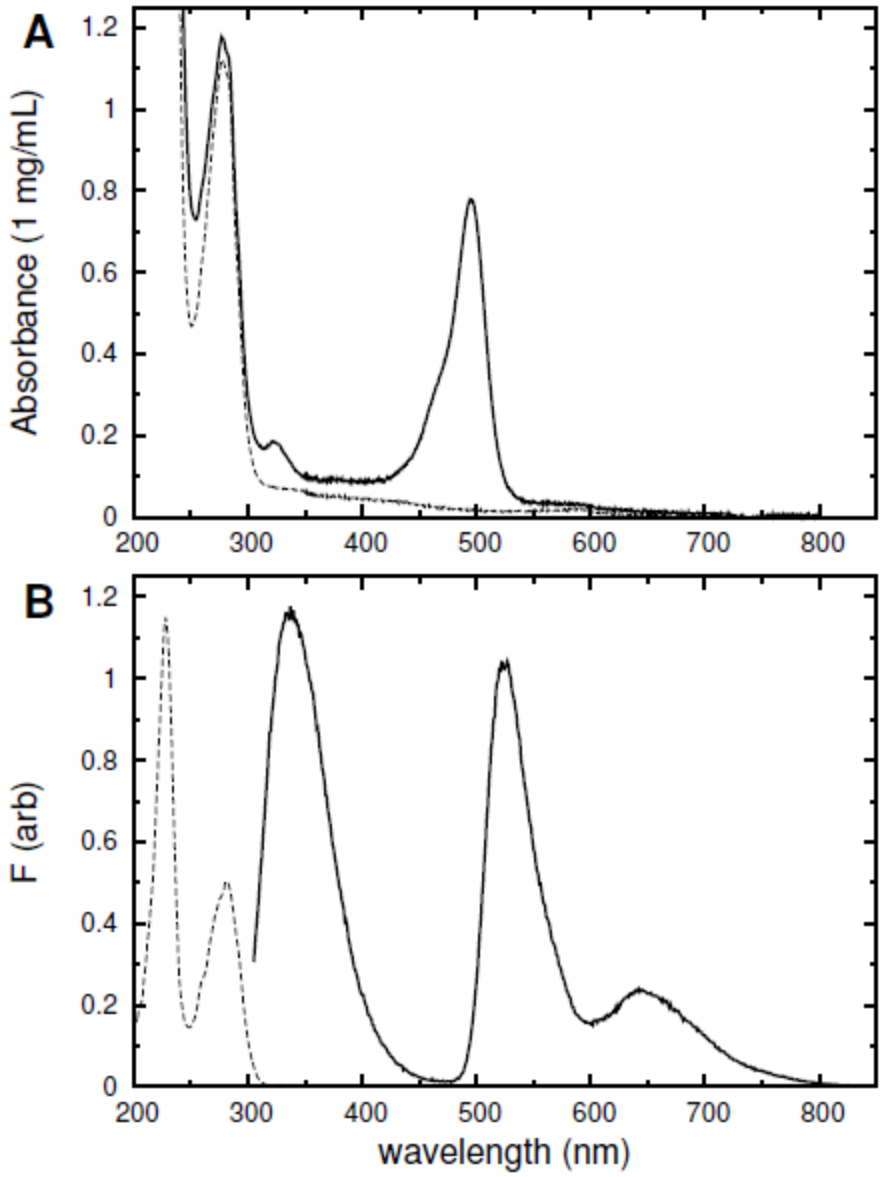

Figure A2. Spectroscopic characterization of AaCSFl in buffer PK8. (A) Absorbance spectra of AaCS (dotted line) and AaCSFl (solid line) with each scaled to 1 mg mL^{-1} (21 mM subunits). (B) AaCSFl fluorescence excitation (dotted line) and emission (solid line) spectra. The excitation and emission spectra were recorded with emission and excitation wavelengths of 339 nm and 295 nm, respectively.

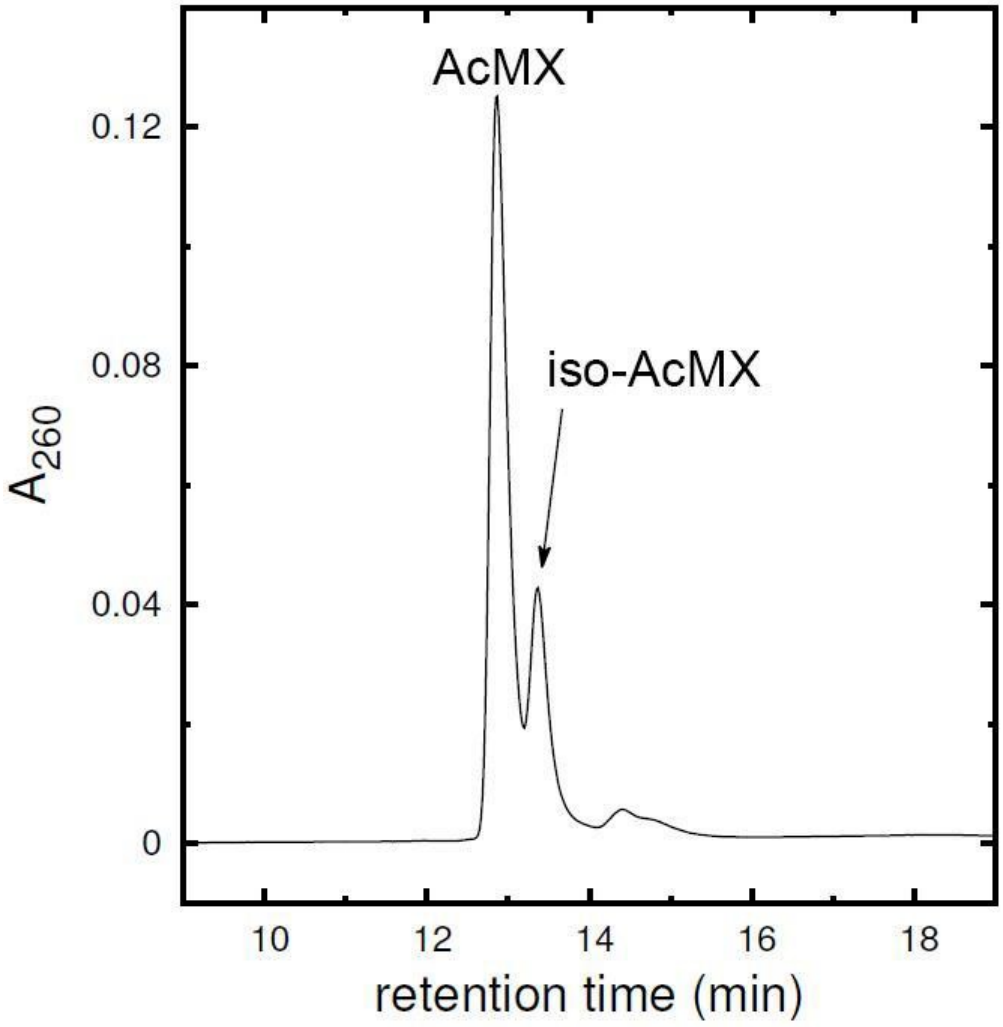

Figure A3. Analysis of AcMX by HPLC. The areas of the indicated peaks correspond to a 5:1 ratio of AcMX:iso-AcMX.

VITA

VITA

Jesse Murphy was born in Champlin, MN. After graduating Champlin Park High School in 2003, Jesse took a year off to work before enrolling at the University of Minnesota Duluth. Jesse received his B.S. in Biochemistry and Molecular Biology in 2008. He remained in the Hinderliter lab and received his M.S. in Biochemistry the following year. Jesse joined the Biochemistry program at Purdue in 2010 and received his Ph.D. in 2016 with Dr. T.J. Kappock.